Karl Rudolf Marguc

High temperature annealing of gold thin- films on thermally oxidised silicon

DIPLOMARBEIT

zur Erlangung des akademischen Grades
Diplom-Ingenieur

Diplomstudium Technische Physik

Technische Universität Graz

Betreuer:

a.o.Univ-Prof. Dr. Roland Resel

Institute of Solid State Physics
Graz University of Technology
Austria

Graz, Juli 2010

Contents

I. Abstract

Using a thermal evaporation method, gold thin films with thicknesses of 20nm, 50nm, and 100nm have been prepared on thermally oxidized silicon. The film characteristics were investigated by X-ray diffraction techniques, optical microscopy, scanning electron microscopy, focused ion beam, and atomic force microscopy as a function of different thermal annealing temperatures up to 900°C ex-situ and up to 1100°C in-situ. 'As-prepared' films were rather smooth (0,92% - 5%) but roughness and morphology were strongly dependent on their film thickness.

Ex-situ characterization led to the following fundamental conclusions: all 'as-prepared' gold films had a strong $\{111\}_{Au}$ and a weak $\{511\}_{Au}$ texture. Compared to the structure at room temperature, at higher annealing temperature the $\{111\}_{Au}$ texture got stronger and the $\{511\}_{Au}$ texture weaker. After thermal annealing at 700°C a weak $\{220\}_{Au}$ was observed. On contrary, after thermal annealing at 900°C strong $\{111\}_{Au}$ and $\{200\}_{Au}$ textures were detected. The mosaicity of all films got smaller with higher temperatures. Up to 200°C the crystallite size increased from 20nm to 25nm, however up to 700°C only a slow increase was observed. After the thermal annealing step at 500°C the macroscopic morphology has changed dramatically and three unidentified X-ray diffraction peaks were observed.

In- situ thermal annealing X-ray diffraction characterization led to following conclusions: at 800°C the vertical crystallite size has increased from 20nm to 32nm and stayed then constant up to 1100°C. Up to 500°C the microstrain has increased from 0.04% to 0.1% and has continuously decreased back to 0.04% at 1100°C. The linear thermal expansion coefficient of gold was calculated with $\alpha=15{,}6\times10^{-6}\ C^{-1}$.

While thermal annealing at 500°C a drastic change of the morphology was observed. Gold islands with significant higher highness profile of 300nm were formed, and small areas with no or low gold coverage in the vicinity of the islands were observed. Morphology changes were centered around a square pyramid morphology, which was identified as a crack in the thermal oxide layer developed by diffusion. Probably Au/Si alloys have been formed, but with the used measurement techniques they could not have been proven. In-situ SEM investigations have shown that the changing of the morphology was accelerated at higher temperatures. the morphological change started at edges, where the amorphous silicon oxide layer was broken. On the top of increased gold hills only gold has been observed and under it a mixture of two phases were found.

II. Acknowledgement

In the beginning I want to say: “Thank you Roland Resel”. He was my supervisor and supported this work all over the time and got involved with my studies very motivated. Even though my own stolidity let loosing my way Roland was patient forever and stayed true to the motto “learning by doing”. Moreover I want to thank my group of Institute of Solid State Physics, Graz University of Technology, supporting my work and solving problems every time. In this context Oliver Werzer was a nice helping person building relations between experimental and theoretical effects. Markus Koini, who was specialized measuring with Philips diffractometer and DHS900 from Anton Paar and measuring pole figures, was also a great help as well as Heinz Georg Flesch. He measured all XRR investigations with Brucker Discover D8 and AFM images of my samples as well as the very complex DHS1100 in-situ x-ray diffraction measurements together with Oliver Werzer. Armin Moser helped me solving theoretical and experimental structure problems with computer programming in Matlab. As I lost my head Tatjana Djuric helped me arranging my ideas. And Birgit Kunert was my contact person finding literature and papers.

When I was in Bratislava preparing some samples, J. Jakopovič (*Department of Microelectronics*) evaporated the gold films, D.Haško (*International Laser Center Bratislava*) measured AFM images and A. Šatka (*International Laser Center Bratislava*) SEM images images of the samples as prepared. Thank you!

Because of macroscopic morphology changes of the gold layers after thermal annealing above 500℃ FIB (focused ion beam) measur ements were made by Harald Plank(*Institute for Electron Microscopy, Graz University of Technology*) and SEM (scanning electron microscopy) measurements ex-situ as well as in-situ were measured by Peter Pölt with great enthusiasm.

Moreover I want to thank the following persons of our institute: Peter Pacher and Markus Postl for helping evaporating more gold films in our own laboratory, Adolf Winkler for leading my evaporation parameters, and Egbert Zojer for leading the preparation of template stripped gold films on glas.

III. Fundamentals

Solid state physics is known as the study describing the large existing properties and phenomens of solid materials resulting from their atomic properties. The fundamental assignment differs between amorphous and crystalline solid materials. In this work primarily X-ray scattering methods were used. So during thermal annealing process changes of parameters like lattice constant, crystallite orientation, and other parameters were described. Moreover these parameter descriptions are based on ex-situ as well as in-situ measurements.

3.1. reciprocal space

The reciprocal space is well describing periodical functions easier than in the real space. A crystal is a periodical arrangement of atoms, molecules, and ions extending in all three real space directions. Because of the periodical arrangement a repeating pattern can be constructed called crystal lattice. The smallest unit of the crystal lattice with the highest symmetry is called primitive unit cell (see Figure 3.1) and can be described and specified in the real space as well as in the reciprocal space.

3.1.1. real lattice

In real space the unit cell is quantified by three basis vectors. They are described by the lattice constants **a,b,c** and the angels **α,β,γ** (alpha, beta, gamma) between them (see Figure 3.1). You can differ in six crystal classes of translational periodicity [11]. They are called cubic, tetragonal, orthorhombic, hexagonal, monoclinic, and triclinic. The triclinic lattice is the least symmetric of the fourteen Bravais lattices and the only one having no mirror plane itself. It has three unequal basis vectors and all three angels are different from 90 degree. In this work the cubic crystal class is the most important. It is described by three equal basis vectors (a=b=c) and three equal angels of 90 degree ($\alpha=\beta=\gamma=90°$).

One of the fundamental question of solid state physics science is how many different lattices do exist. The answer was discovered by Auguste Bravais in Paris (1849). If you vary the length of the lattice constants and the corresponding angels, there will exist endless variations of lattices. But if you only differs the lattice symmetry, you will find exactly fourteen fundamental lattice types, called after the discoverer, Bravais lattices. A Bravais lattice is an infinite set of points generated by a set of discrete translation operations described [11] by:

$$\mathbf{t}=n_1\mathbf{a}+n_2\mathbf{b}+n_3\mathbf{c} \qquad (3.1)$$

Where n_i are any integers and **a**, **b**, **c** are known as primitive vectors, which lie in the different planes and span the lattice. A Bravais lattice consists of only one particle sort. Thus e.g. the NaCl lattice results from translation per a cubic-face-centered lattice from positive Na ions and negative Cl ions.

In the regular cubic lattice system exist three different Bravais lattices. The simple cubic lattice is a cube with the edge length **a**. In the body centered cubic Bravais lattice is one lattice point added in the center of the cube. And the third lattice has in every face of the cube an additional lattice point, so called face centered cubic Bravais lattice.

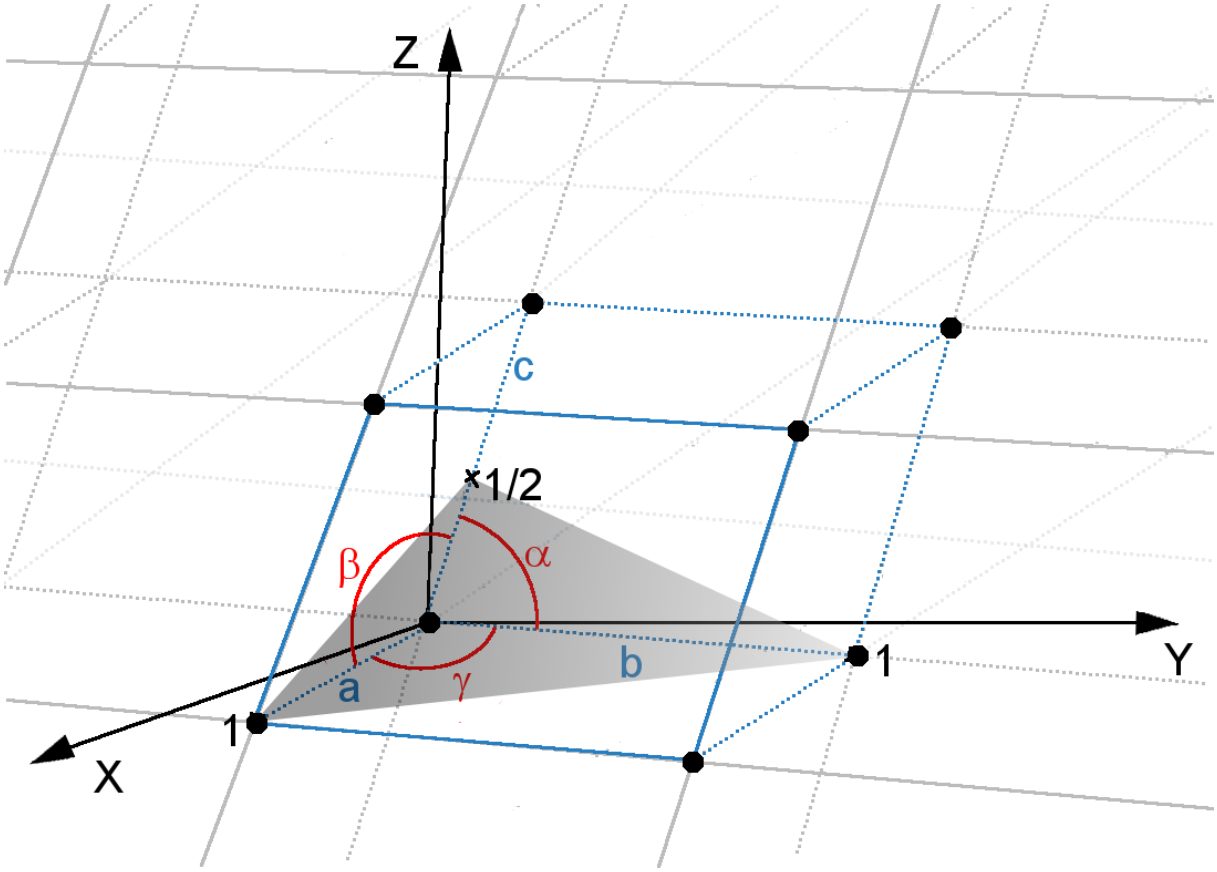

Figure 3.1: Crystallographic unit cell (lattice constants a,b,c alpha, beta, gamma) of a general periodic lattice together with the construction of a (112) plane.

In combination with X-ray scattering existing a set of equivalent lattice planes in a crystal is a fundamental condition. The so called Miller indices are a notation system used to specify the orientations of lattice planes and directions. The indices define where the plane cuts the unit cell edges a,b,c of the unit cell and are denoted by the integers h,k,l. A single net plane is denoted with (hkl). A set of parallel planes have the same indices and are called equivalent net planes, denoted by {hkl}. In figure 3.1 a unit cell with the construction of a (112) plane is shown. The formation of a set of equivalent net planes because of the periodical arrangement of the atoms in all three real space directions are visualized by the grey lines in figure 3.1. Because of the {112} set of parallel planes a 112 X-ray diffraction peak is possible to be observed (see chapter3.2.).

3.1.2. reciprocal lattice

Scattering techniques are based on the superposition of single scatter centers. X-ray scattering uses electrons as scatter centers. The periodical arrangement of atoms in a crystal leads to scattering maxima under special conditions. Finding an unique solution of the mathematical equation describing, the superposition of scattered waves, the reciprocal lattice is defined. The transformation from the real lattice with the three primitive vectors **a**,**b**,**c** to three reciprocal lattice primitive vectors **a***,**b***,**c*** is defined by the equals 3.2a, 3.2b, and 3.2c.

$$\vec{a}^* = 2\pi \frac{\vec{b} \times \vec{c}}{\vec{a} \cdot (\vec{b} \times \vec{c})} \qquad (3.2a)$$

$$\vec{b}^* = 2\pi \frac{\vec{c} \times \vec{a}}{\vec{b} \cdot (\vec{c} \times \vec{a})} \qquad (3.2b)$$

$$\vec{c}^* = 2\pi \frac{\vec{a} \times \vec{b}}{\vec{c} \cdot (\vec{a} \times \vec{b})} \qquad (3.2c)$$

A general lattice vector **G** in the reciprocal space is denoted by :

$$\vec{G} = h \cdot \vec{a}^* + k \cdot \vec{b}^* + l \cdot \vec{c}^* \qquad (3.2)$$

The orientation of the reciprocal lattice vector is generally orthogonal to the corresponding lattice plane in real space (see figure3.2). Another significant characteristic includes the fact that the norm of the reciprocal lattice vector is reciprocal proportional to the lattice plane distance in real lattice (see figure 3.2).

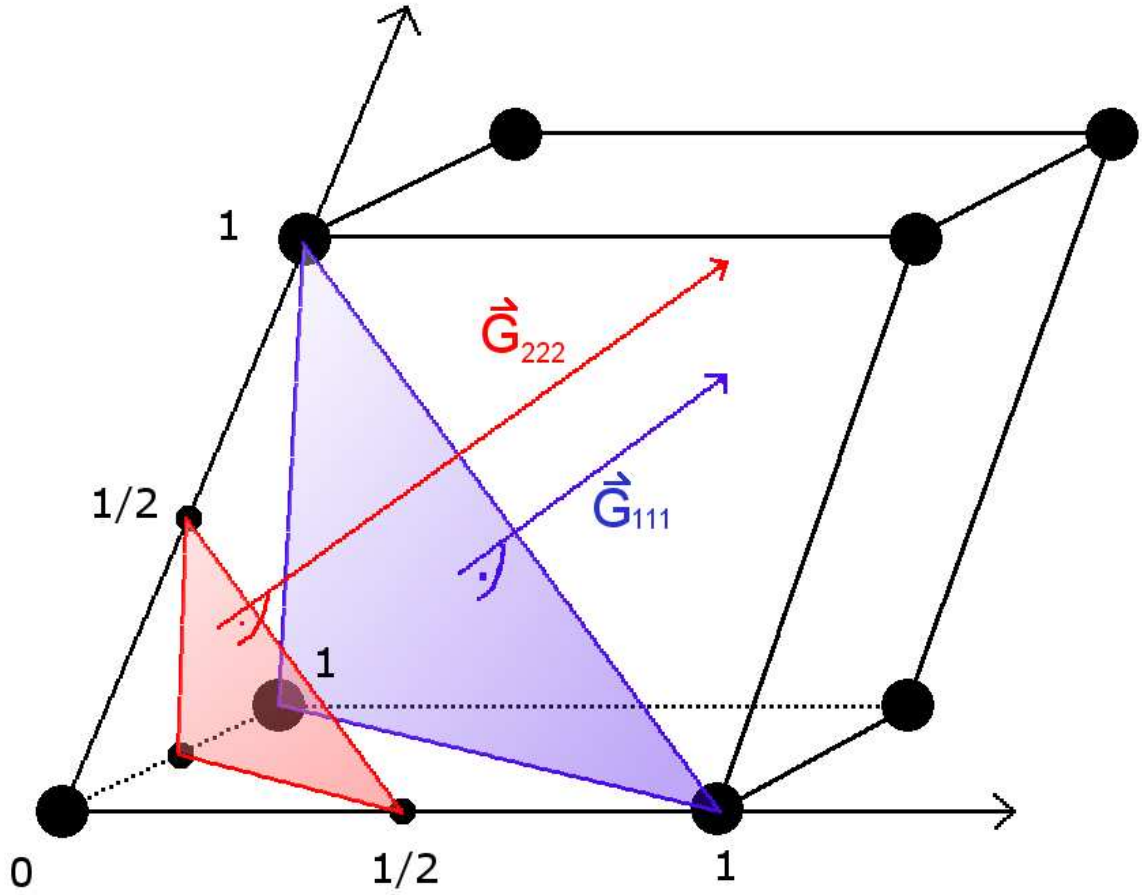

Figure 3.2: example for a reciprocal space vector: the orientation of the reciprocal space vector is orthogonal to the corresponding lattice plane in real space and the norm is reciprocally proportional to the lattice plane distance in real space

Comparing reciprocal space with real space of a single crystal with cubic unit cell in figure3.3 shows the fact that each (hkl) point in the reciprocal space corresponds to a set of lattice planes in the real space lattice. Tilting the crystal in real space will tilt the reciprocal space just as well. Moreover the reciprocal characters are shown by calculating the half and third real space lattice distances of (hhh) planes and the corresponding reciprocal lattice points. The corresponding observed X-ray diffraction peaks of the second and higher calculated reciprocal space points are called higher order peaks. At second in the right side of figure 3.3 geometry possibilities of the X-ray goniometer in Eulerian geometry are displayed in front of the primary beam (see also figure 3.9d).

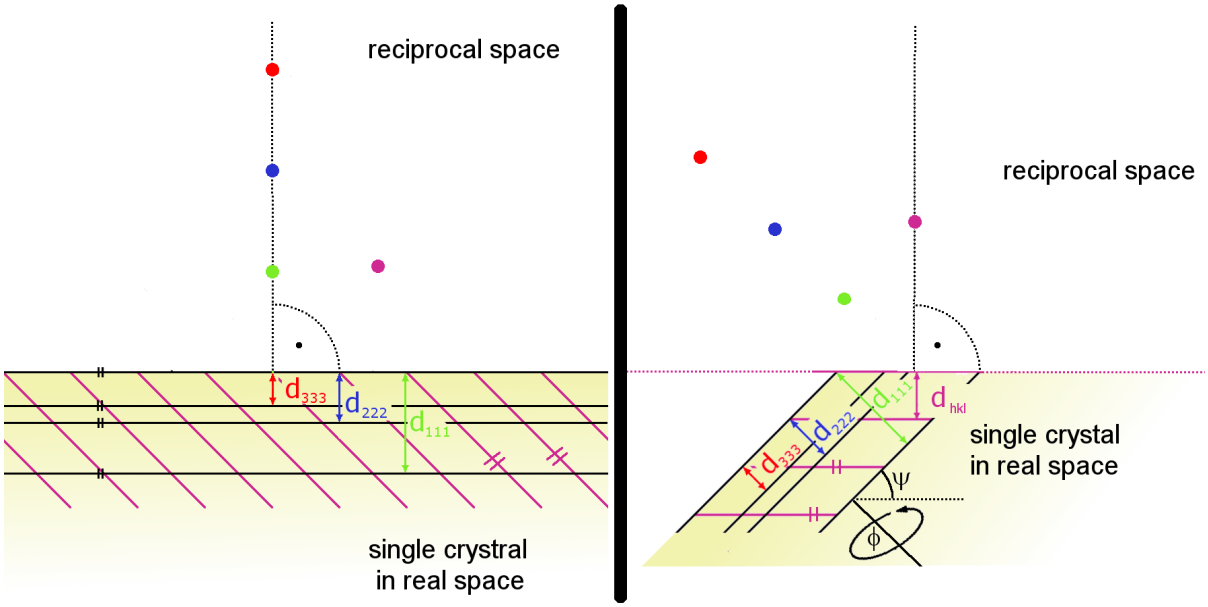

Figure 3.3: left: reciprocal lattice points of the (hhh) planes and of a general (hkl) plane; right part: tilting of the same sample by the angle ψ causes also a tilt of the reciprocal lattice.

In a powdered sample every possible crystalline orientation is represented equally. Therefore the real space lattice planes of the crystallites with same lattice constants and so on with the same real space lattice distances but not the same orientations correspond with a set of reciprocal lattice points. They have the same norm but no special orientation all over the whole reciprocal space. Therefore a powder is represented by spheres in three dimensional reciprocal space (see figure 3.4).

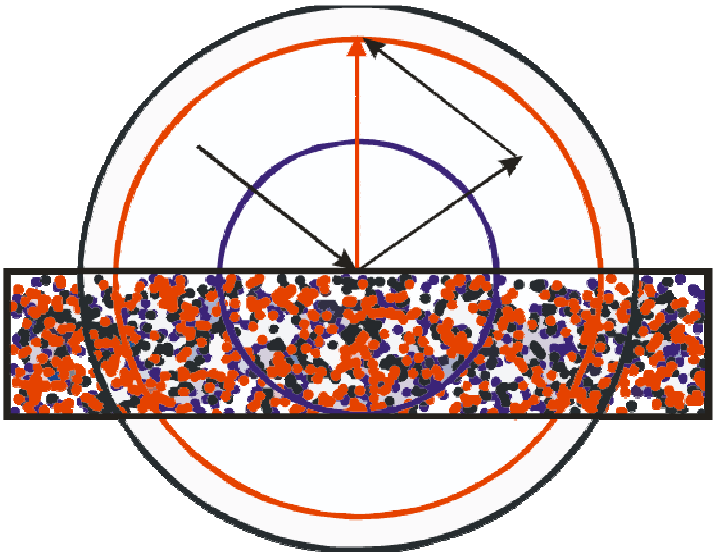

Figure 3.4: reciprocal space of a powder (set of non orientated crystals) [2] –

3.1.3. two dimensional powder

In a perfect powder every possible crystalline orientation is represented, so called three dimensional powder (3D-powder). If in a powder one special preferred (hkl)-plane and the corresponding higher orders of all crystallites have the same orientation, the orientation specification in reciprocal space of all other existing (hkl) planes will be possible reduced to only two reciprocal space vectors. In this case therefore the powder is called two dimensional powder (2D-powder). In a perfect 2D-powder the preferred and parallel (hkl) plane of all crystallites is represented by the z-axis of the reciprocal space. And further the other orientations are represented in the two dimensional q_x, q_y-plane of the reciprocal space (see Figure 3.5).

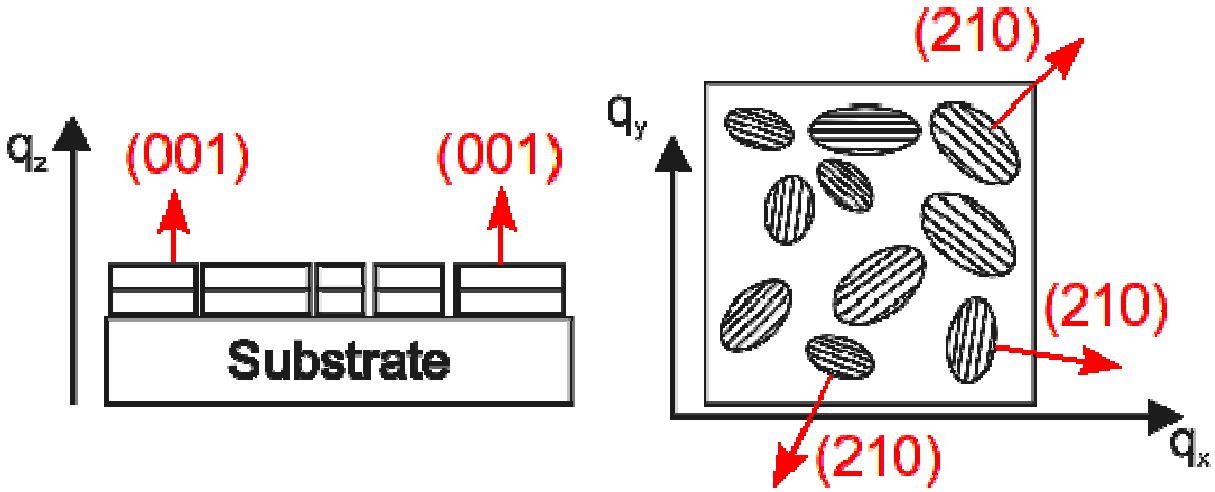

Figure 3.5: two-dimensional powder with a 001 texture: (00l) planes are parallel to surface of the substrate. The in-plane reciprocal space vectors of all (210) planes are not oriented. They have contributions in the whole reciprocal space only in q_x and q_y.

In a 2D-powder a set of crystallites have a special collective orientation parallel to the substrate surface so that one real space (hkl) lattice plane is parallel to the substrate surface – so called {hkl} texture. The other planes of these crystallites have different orientation. Therefore a 2D powder is represented by circles in the reciprocal space. Representing a 2D powder the significant coordinates of the reciprocal space can be reduced to one parallel to the real space substrate surface q_p , defined by equation 3.3, and a orthogonal one q_z (see Figure 3.5 and 3.6)

$$q_p = \sqrt{q_x^{\,2} + q_y^{\,2}} \qquad (3.3)$$

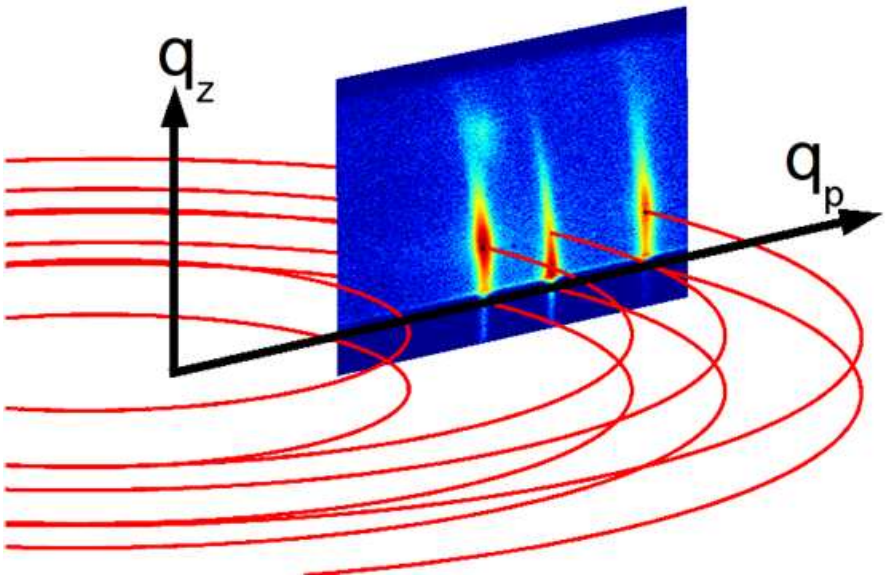

Figure 3.6: The reciprocal space of a two-dimensional powder [2] are reduced to circles

An idealized {hkl} textured powder on a substrate exists if all crystallites have a collective (hkl) plane parallel to the substrate surface. In reality of a {hkl} textured powder a lot of crystallite (hkl) plane positions are tilted by a small angle to the substrate surface (see Figure 3.7). The smaller the averaged angle the better is the powder textured.

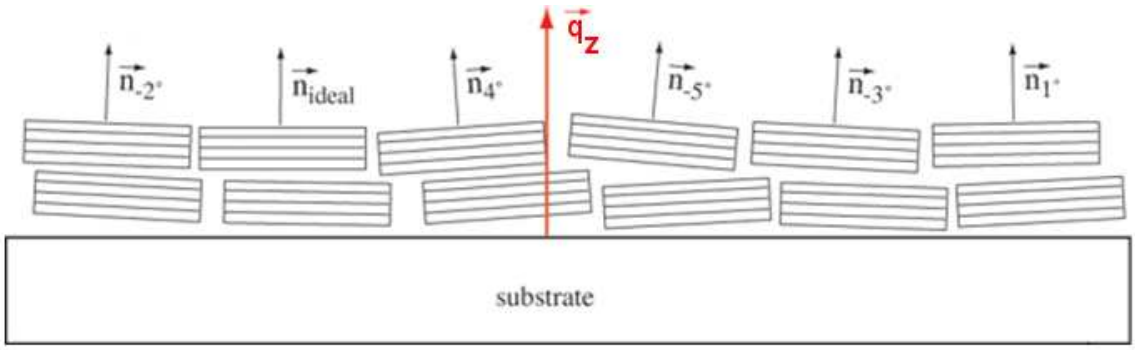

Figure 3.7: Two-dimensional powder alignment [4]: in the example the real space planes of the crystallites are shown parallel to substrate surface. The better the alignment the more parallel the normal vectors of the crystallites to the corresponding scatter vectors will be.

3.2. X-ray scattering

X-ray scattering techniques are a family of non-destructive analytical techniques which reveal information about the crystallographic structure, chemical composition, and physical properties of materials and thin films. These techniques are based on observing the scattering intensity of an X-ray beam hitting a sample as a function of incident and scattered angle, polarization, and wavelength or energy.
The fact that the inter-atomic distances in crystals and molecules correspond in the electromagnetic spectrum with the wavelength of X-ray (see figure3.9a) is one fundamental condition getting diffraction (elastic scattering). The second fundamental condition is a long range order in the analyzed sample.

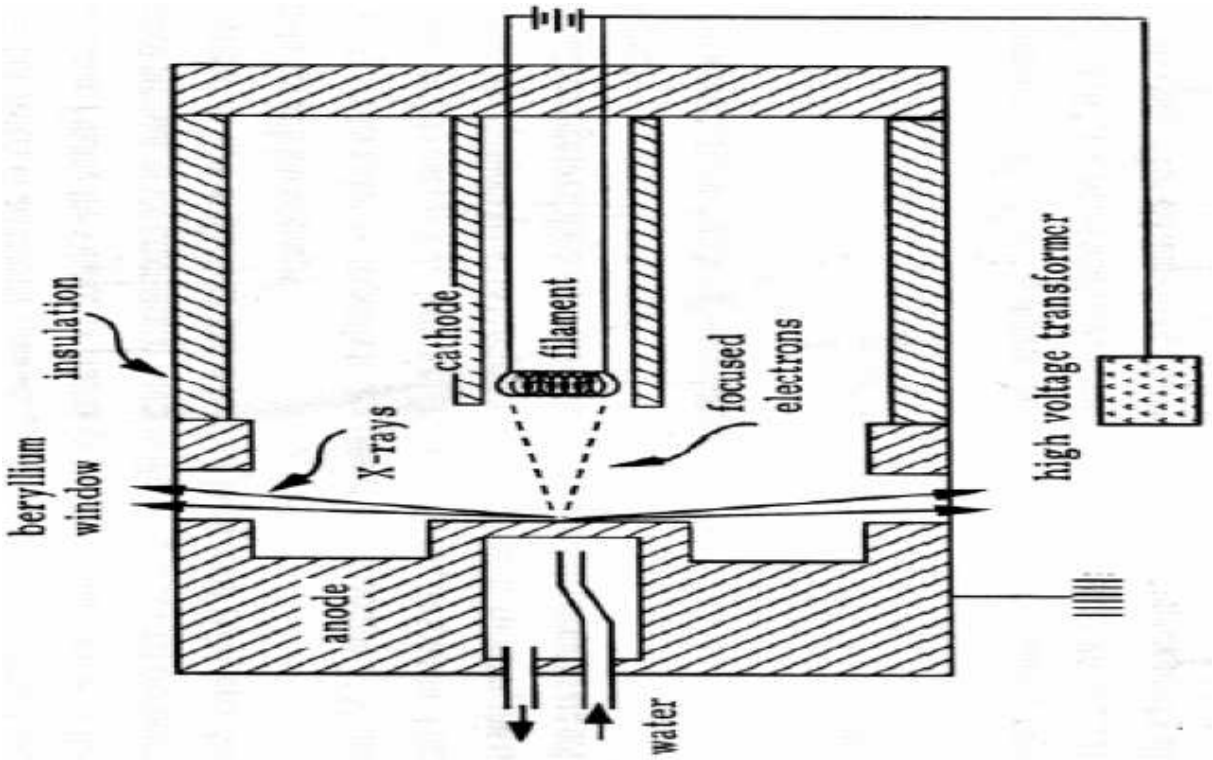

Figure 3.8: principle assembling of a X-ray tube [11]

In labor X-ray tubes (see Figure 3.8) are used to produce the primary X-ray beam. X-ray tubes are vacuum tubes with a cathode emitting electrons into the vacuum and an anode collecting them. A high voltage power source, in this work 40kV, accelerates the emitted electrons. The produced X-ray spectrum depends on accelerated voltage and used anode material. The most used materials are copper, chrome, molybdenum, and wolfram. They generate X-ray photon spectrum, known as Bremsstrahlung (see Figure3.9a). In this work only copper and chrome were used. Every Bremsstrahlung have significantly wavelength with high intensity (see figure 3.9a) noted by K_α (7) and K_β (9) in example of figure 3.9a. The first letter is always the refilled atomic shell. The second Greek letter symbolizes the shell distance. For example the electronic transition between the atomic shells L to K emits K_α and the transitions from the shells M to K emit K_β radiation. In the atomic L shell there are three different levels. Two of them allow L to K transition [4] leading to the different radiation wavelength $K_{\alpha 1}$ and $K_{\alpha 2}$ (see Figure 3.9b).

In this work two different X-ray goniometers were used. In figure 3.9c (Brucker Discover D8) and in figure 3.9d (Phillips powder diffractometer) the principle assembling of both different goniometers is displayed. The X-ray beam coming from the X-ray tube is called primary beam focused to the sample. The Phillips goniometer has a point focusing beam. And the tube of the Brucker is rotated by 90 degree around his length axis getting a line focusing beam. After scattering the primary beam under special conditions (see following capture) the intensity of the scattered beam is measured by the detector varying its position by 2θ circle way (see Figure3.9c+d). The sample is tilted by characterizing parameter θ in detector direction, orthogonal to detector by characterizing parameters ψ (Phillips) or χ (Brucker), and is able to rotate around the sample normal characterized by parameters φ(Phillips) and ϕ(Brucker). The so called Eulerian geometry is in principle used at both devices. The line focusing at the device of Brucker leads to the fact that a greater area of the analyzed sample is registered by primary beam instead of using point focusing (Phillips), which gets to a sharper scattering registration. Therefore X-ray reflectivity (XRR) measurements were practiced with Brucker device.

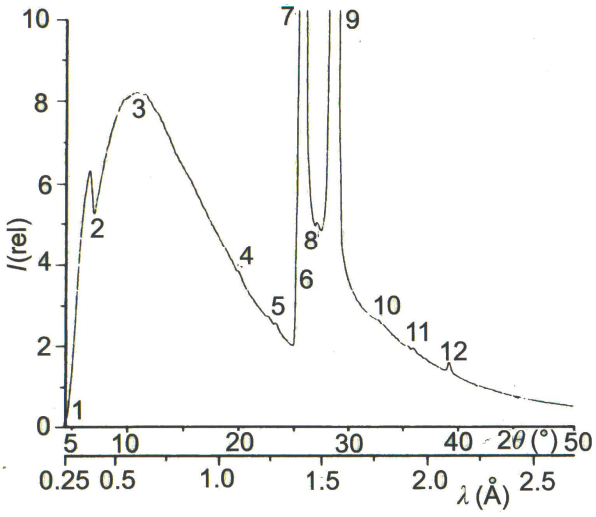

a.) copper Bremsstrahlung [8,10]

	Cu [Å]	Cr [Å]
Kα1	1.54059292	2.289746
Kα2	1.544414	2.2936517
Kβ1	1.392246	2.084912

b.) wavelength table [8]

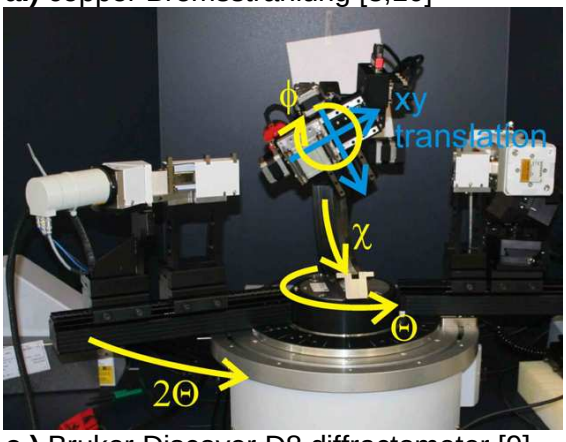

c.) Bruker Discover D8 diffractometer [9]

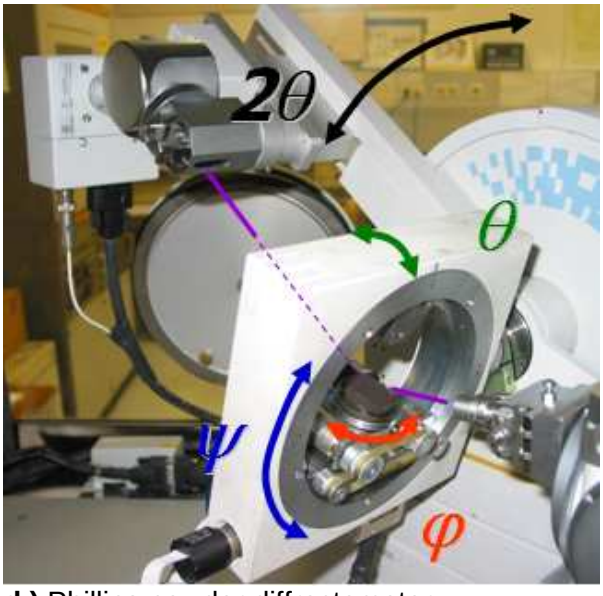

d.) Phillips powder diffractometer

Figure 3.9: a.)spectrum of a characteristic Cu X-ray radiation with the high intensity wavelengths CuKβ(7) and CuKα1+CuKα2(8) [8] **b.)** most important wavelength of used X-ray tubes **c+d.)**principal assembling of a X-ray goniometer in Eulerian geometry in Bragg-Bretano line focusing (c) and point focusing geometry.(d)

3.2.1. diffraction conditions

As noted X-ray diffraction is an elastic scattering process. For this reason the norm of the primary beam k_0 is equal to the norm of the scattered beam k (see equation 3.4).

$$\left|\vec{k}_0\right| = \left|\vec{k}\right| = \frac{2\pi}{\lambda} \qquad (3.4)$$

At second the primary beam has to be coherent getting a constructive diffraction. Describing the measured diffraction a scattering vector q is defined as the difference from the primary beam vector k_0 to reflected beam vector k (see equation 3.5 and figure 3.10).

$$\vec{q} = \vec{k} - \vec{k}_0 \qquad (3.5)$$

Varying the detector position the norm of scattering vector changes. Rotating the sample the orientation of the scattering vector can be changed. Only if the scattering vector and the reciprocal space vector are equal the reflected beam will be registered by the detector.
Figure 3.10 displays a single crystal with (hhh) planes parallel to the crystal surface. A believing (hkl) plane is also displayed. The theoretical construction getting a detector signal of reciprocal space point corresponding to the real higher ordered (333) plane is also displayed. Consequently to this construction is the condition, that the scattering vector q and the reciprocal space vector G_{hkl} have to be parallel and must have the same norm to register any diffraction peak by detector. This condition is called Laue condition and is displayed in equation 3.6:

$$\vec{q} = \vec{G}_{hkl} \qquad (3.6)$$

The distance d_{hkl} between two crystal layers characterized with the three Miller indices **h,k,l** of a cubic crystal with unit cell parameter **a** is given by

$$d_{hkl} = \frac{a}{\sqrt{h^2 + k^2 + l^2}} \qquad (3.7)$$

The scattered intensity is described theoretically by the primary intensity and the following proportional factors:

- slit interference function in all three lattice constant directions
- square norm of the structure factor

The intensity maximum of a diffraction pattern is observed, if equation (3.8) is satisfied.

$$\lambda = 2\frac{a}{\sqrt{h^2 + k^2 + l^2}}\sin\theta \qquad (3.8)$$

From equation (3.4), (3.7), and (3.8) the very popular Bragg equation (3.9) is derived:

$$n \cdot \lambda = 2 \cdot d_{hkl} \cdot \sin(\theta) \qquad (3.9)$$

The equation describes the position of X-ray diffraction peaks in angular space and is equivalent to the Laue condition (3.6).

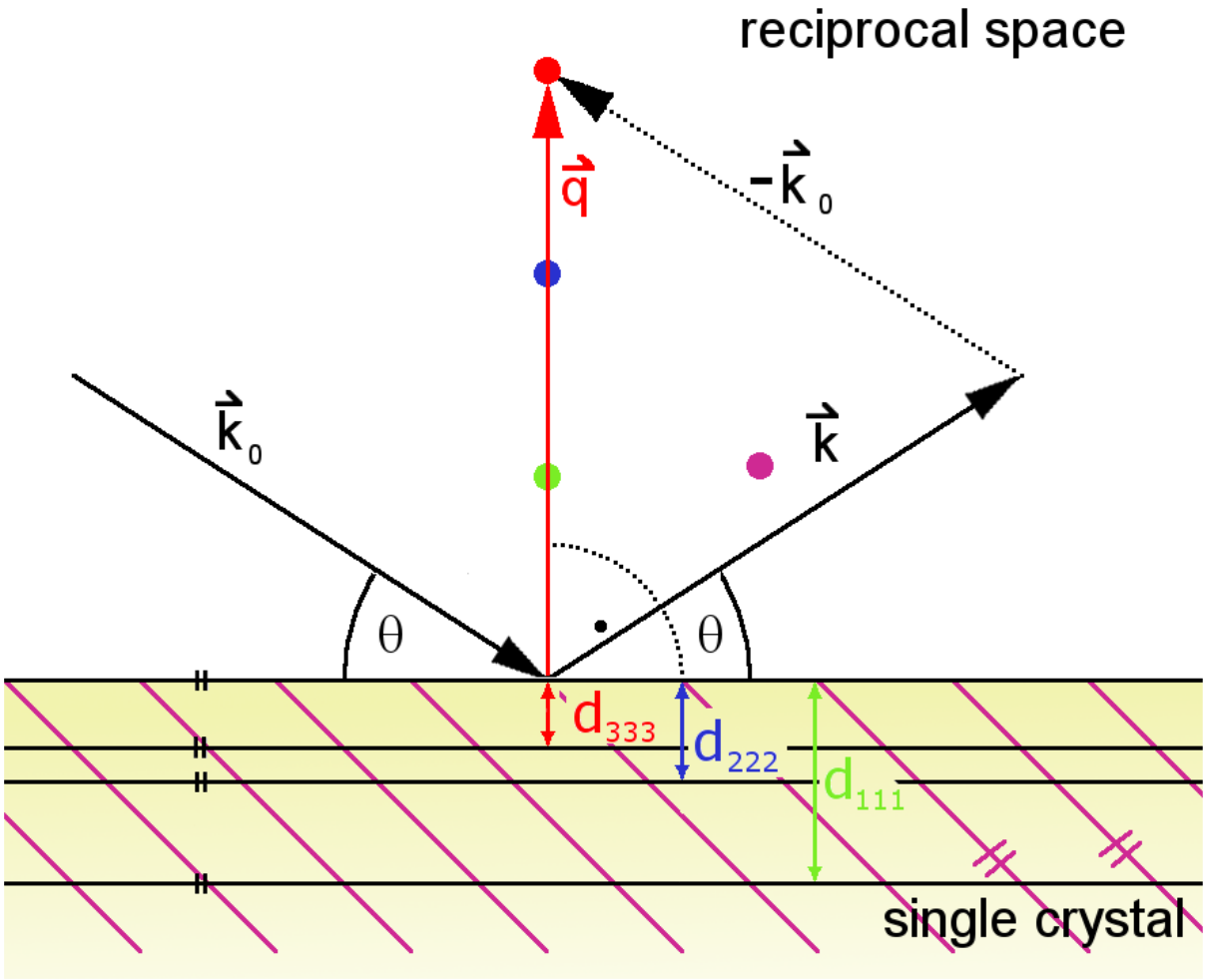

Figure 3.10: specular geometry provides the scattering vector **q** perpendicular to the sample surface

3.2.2. Scherrer equation

The Scherrer equation (3.10) is one way analyzing the average size dimension of single crystallites in hkl direction, so written D_{hkl}. X-ray measuring peaks with wave length λ leads to a relation between the average crystallite size $\langle D_{hkl} \rangle$ and the integral breath $\beta_{2\theta,hkl}$ of the analyzed peak . The integral breath is defined as ratio of the full fill peak area and the average highest intensity, which is positioned in the peak centre and found by measured data fitting.

$$\left\langle D_{hkl} \right\rangle = \frac{K_{Scherrer} \cdot \lambda}{\beta_{2\theta,hkl} \cdot \cos(\theta_{hkl})} \qquad (3.10)$$

Where θ_{hkl} is the peak centered Bragg angle and $K_{Scherrer}$ is the shape factor, also known as Scherrer constant. The dimensionless shape factor has a typical value of about 0,9, but varies with actual shape of the crystallites. Finding the integral breath needs a large number of measured data getting well fitted. Moreover the integral breath dimension has to be transformed in radiant dimension to calculate the true integral breath account.

3.2.3. Williamson Hall plot

The crystallites in a polycrystalline thin film in general exhibit defects and lattice distortions [7]. Consequential effects of distortions are expansions and contractions. Assuming both effects occur with equal probability a strain field describes them quantitatively. Strain causes varying inter planar distance Δd and therefore it is quantitatively noted by ε= Δd/d where d describes the absolute inter planar distance. The relation between strain and line broading can be found by differentiating the Bragg equation [7]:

$$\frac{\Delta d}{\Delta(2\theta)} = \frac{\lambda \cos\theta}{4\sin^2\theta} = \frac{d_0}{2}\cot\theta \qquad (3.11)$$

This equation is interpreted such that the variation in $\Delta(2\theta)$ is identified with the integral breadth β, which is broadened due to the variation in interplanar spacing Δd. The ratio of $\Delta d/d_0$ is considered as the product of the root mean square microstrain ε_{rms} and a scaling factor K_D that depends on the nature of the lattice distortions and the underlying model of microstrain. It then follows for the relation between reflex broadening and strain [7] :

$$\beta_D = 2K_D \cdot \varepsilon_{rms} \cdot \tan\theta \qquad (3.12)$$

The total integral breadth broadening line is an addition of size broadening line, integral breath, and the distortion broadening line. Addition of the Scherrer equation

and equation (3.12) as well as further converting leads to the equation (3.13), which was called after Williamson and Hall.

$$\beta_{2\theta} \cdot \frac{\cos(\theta)}{\lambda} = \frac{K_{Scherrer}}{\langle D_v \rangle} + K_D \cdot \varepsilon_{rms} \cdot \frac{2\sin(\theta)}{\lambda} \quad (3.13)$$

Considering both broadening line effects the equation (3.13) gets a linear characteristic in the space used in figure 3.11:

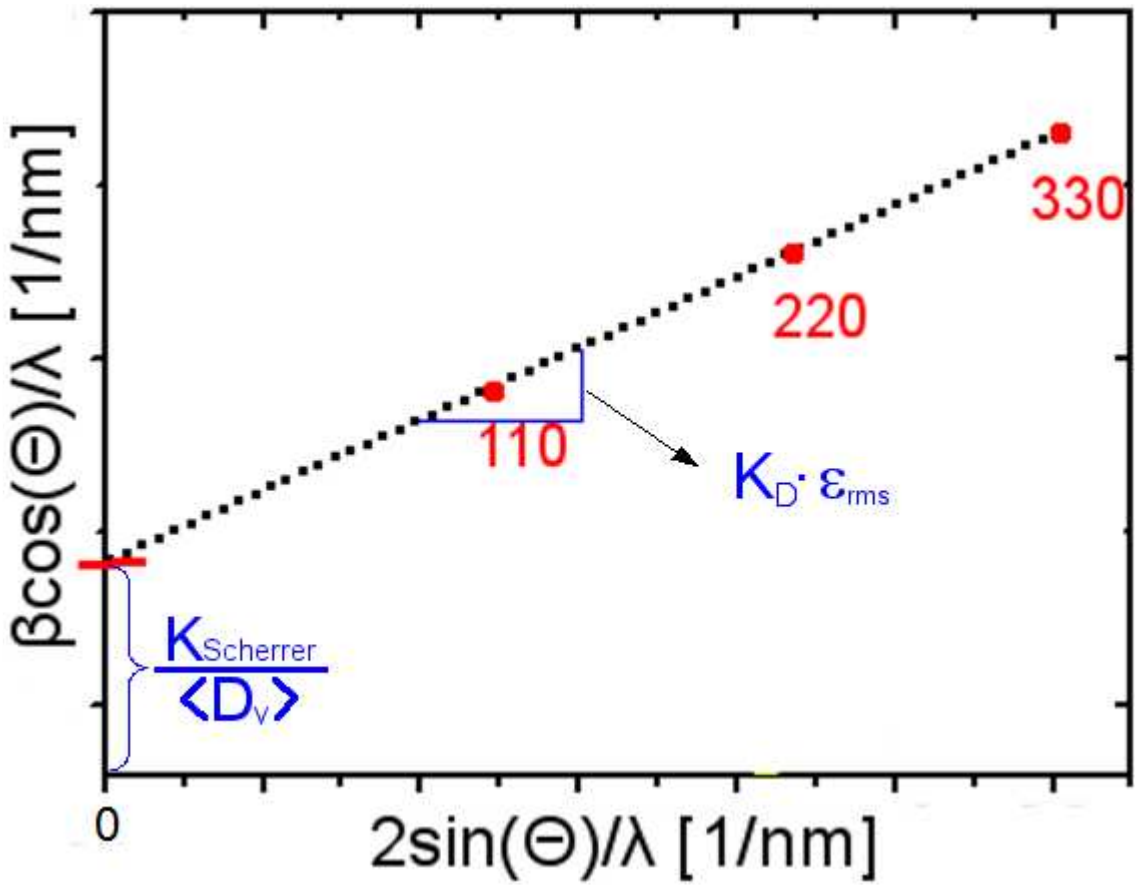

Figure 3.11: theoretical example of a Williamson Hall plot

So with Williamson Hall equation (3.13) the average crystallite size $\langle D_v \rangle$ and the root mean square strain $K_D \cdot \varepsilon_{rms}$ can be calculated, see figure 3.11. Therefore in praxis all measured reflecting peaks and the corresponding calculated integral breadth are plotted in space room shown in figure 3.11. The average crystallite size $\langle D_v \rangle$ and the root mean square strain $K_D \cdot \varepsilon_{rms}$ can be extracted by fitting the as for calculated points with linear fitting model (see figure 3.11).

IV. Experimental techniques

4.1. X-ray scattering

The principal assembling of the two different used X-ray goniometers were the same Eulerian geometry, Brucker Discover D8 in Bragg-Bretano line focusing and the Phillips goniometer point focusing geometry. In figure 4.1 the used geometry with all sample varying parameters is shown. The primary beam k_0 is coming with constant wavelength of the X-ray tube. Between the sample and the used X-ray source is an angle Θ. Therefore the parameter varying the position of the used X-ray source along a circle way around the sample is called Θ. The reflected beam k is registered by a detector also varying its position in a circle way around the sample. In this case the angle between the source and the reflected beam is 2Θ. So the varying parameter of the detector is called 2Θ. By varying these two parameters the norm and direction of the scattering vector q (see equation 3.5) are changed.

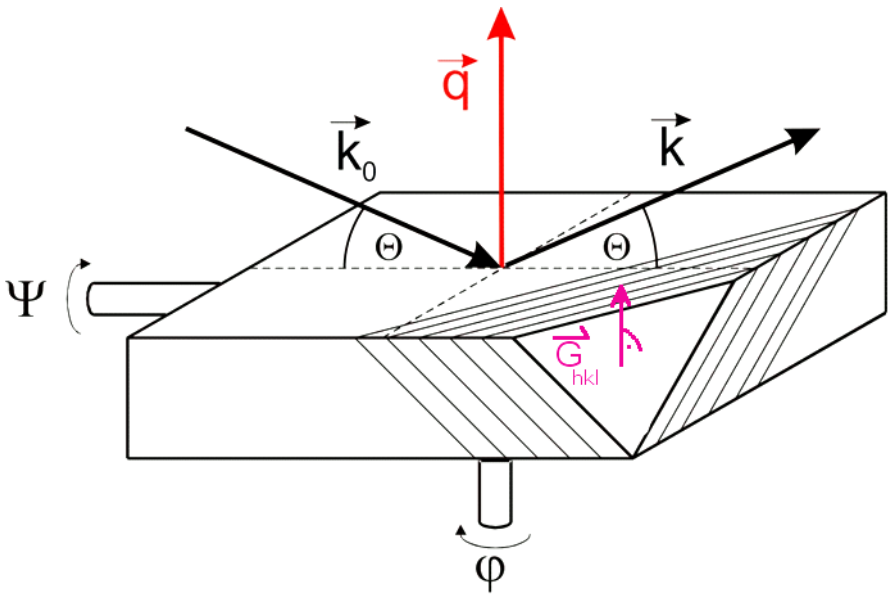

Figure 4.1: diffraction geometry in a system with an Eulerian cradle.
The length of the scattering vector q can be varied by changing Theta(Θ). By varying of Psi(ψ) and Phi(φ) the orientation of the scattering vector can be changed.

Moreover it is possible tilting the sample by parameter ψ and rotating around the z-axis by parameter φ (see figure 4.1). So it is possible varying the direction of special (hkl)-layers and the corresponding reciprocal space vector $\mathbf{G_{hkl}}$ (see figure 3.2) getting parallel to the scattering vector. If the norm of reciprocal space vector is equal and the direction parallel to scattering vector (see figure 3.10) the Laue condition (see equ. 3.6) is satisfied and the detector will register higher intensity.

4.1.1. Θ/2Θ-scan and specular scan

This is the most fundamental applied technique in this work. It is suitable to powder samples which are composed of small crystallites [2]. In a sample with (more ore less) random oriented crystallites it is statistically determined, that some of the net planes always lie parallel to the sample surface[2]. Therefore the sample has not to be tilted while whole scanning time. Getting a diffraction peak it is necessary that the scattering vector and the reciprocal space vector are parallel as well as having the same norm. If the detector angle 2θ at every position accounts the double value of the source angle θ, see chapter 4.1, the scattering vector always will be parallel to the normal of the non tilted sample. Under that conditions the normal vector is identified with z-axis of real space and the scattering vector norm is changed by varying the θ/2θ values. If the scattering vector norm is equal to the reciprocal space vector norm corresponding to a special interplanar layer distance, higher intensity, measuring more counts by detector, will be registered (see Fig.4.2) because of fulfilled diffraction conditions.

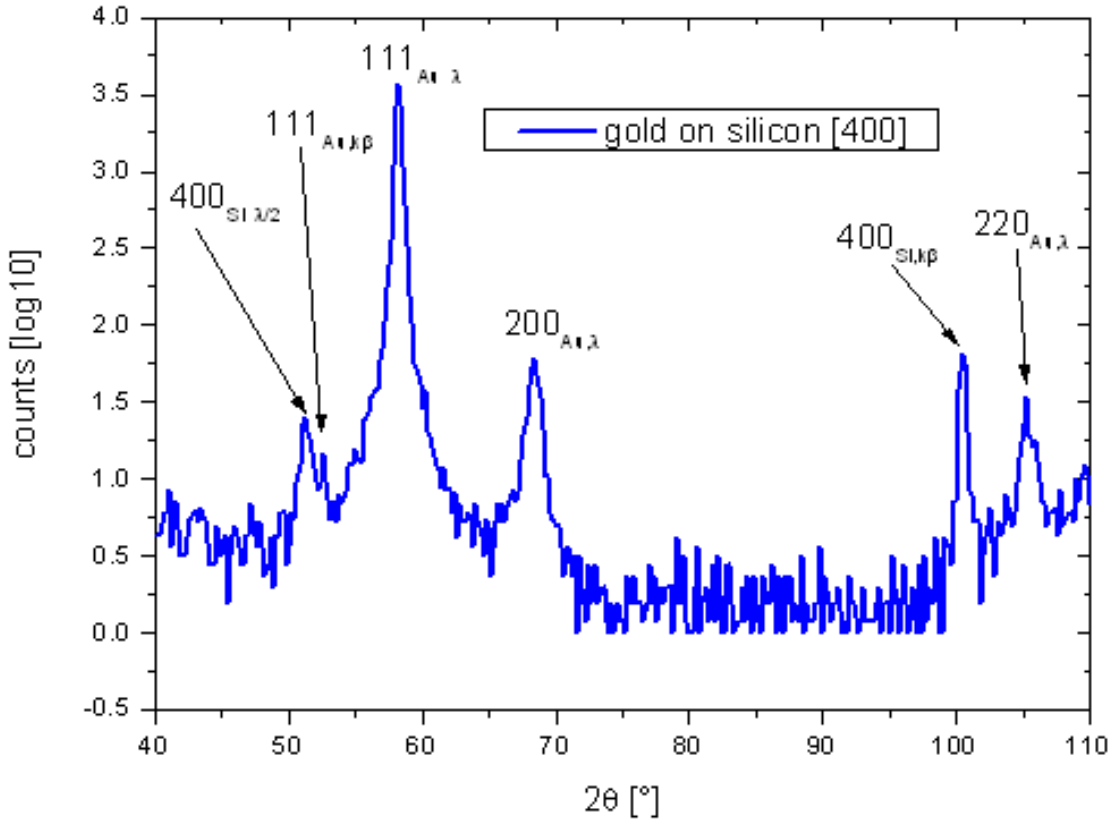

Figure 4.2: specular scan (Θ/2Θ-scan) of a evaporated Au thin film (100nm) on thermally oxidised silicon using Chrome-K_α- radiation.

Moreover the integration time of each step as well as the step width of the 2θ angular take influence to the significance of the measurement. Selecting the regular scanning range all crystallographic orientations parallel to the sample surface are measured. In case of a powder sample all allowed diffraction peaks of the crystallites are measured. And so the sample surface material can be identified by comparing peak

positions. They depend on wavelength of the used source. The peak positions as well as the intensity relationships of them are theoretically calculated with a computer program Therefore the unit cell data, the used wavelength, and other parameters have to be input. In this work the application PowderCell2.4 was used calculating the theoretical comparing data.

4.1.2. pole figures

Measuring pole figures is an experimental technique getting information of the main crystallites orientations on the measured sample. Based on stereographic projection all theoretically existing (hkl) planes of the observed unit cell can be constructed. So in figure 4.3a (100),(010), and (001) plane constructions are shown. Figure 4.3b displays the equatorial plane of the theoretical pole-construction in figure 4.3a concluding the three intersection points of the corresponding planes and is called stereogram. In this work the application WULFF [34] was used for calculating stereogram of the observed materials.

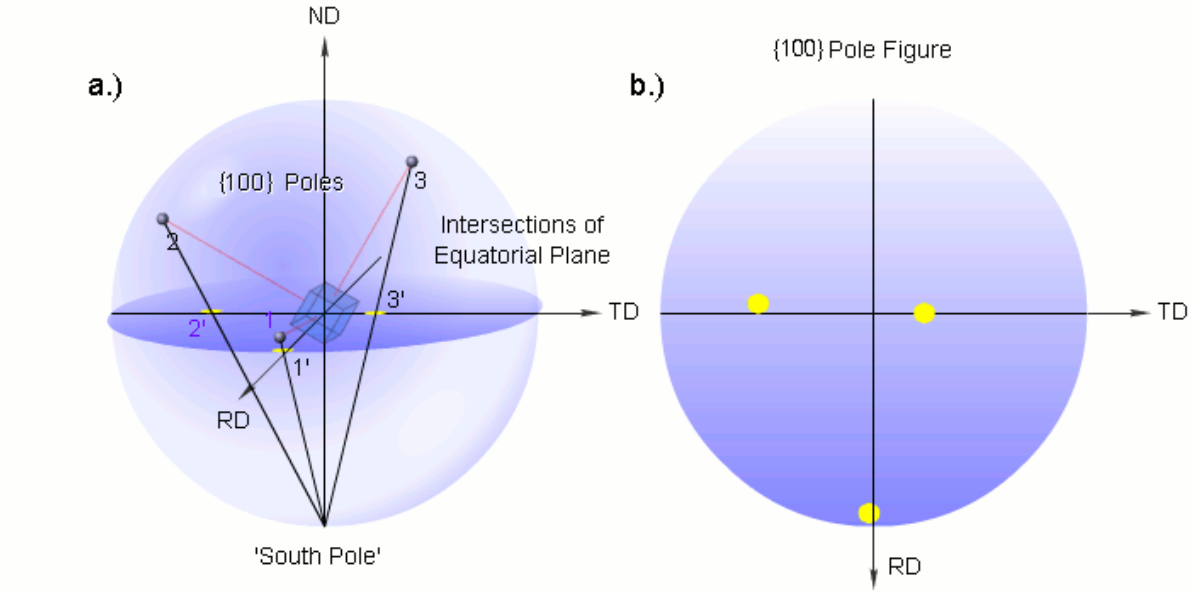

Figure 4.3:**a.) construction** of a stereogram from a cubic crystal **b.) stereogram** of the three planes projected in 4.3.a)

Contrary to the theoretical stereogram in a measured polefigure only one selected interplanar hkl distance can be observed. Knowing this distance the Bragg equation has to be fulfilled registering diffraction intensity. Therefore the 2θ and θ parameters are fixed on a position satisfying the Bragg equation. With this alignment the sample is rotated, represented by the parameter ϕ, around the z-axis in small steps about a range of 360 degree. Moreover the sample is tilted by ψ in small steps about a range of 90 degree(see fig. 4.4b). With other words the scattering vector with a constant norm, corresponding to the observed interplanar distance, is varied its orientation.

In this work only materials with cubic unit cells were investigated. Therefore in figure 4.4a the stereogram of a cubic single gold crystal with (111) layer parallel to surface and the corresponding intersection points is shown. If there exists a gold powder

sample with mostly (111) oriented crystallites parallel to the sample surface, and the other layers of each crystallite are no specifically orientated, a pole figure shown in figure 4.4b will be measured and is called {111} textured.

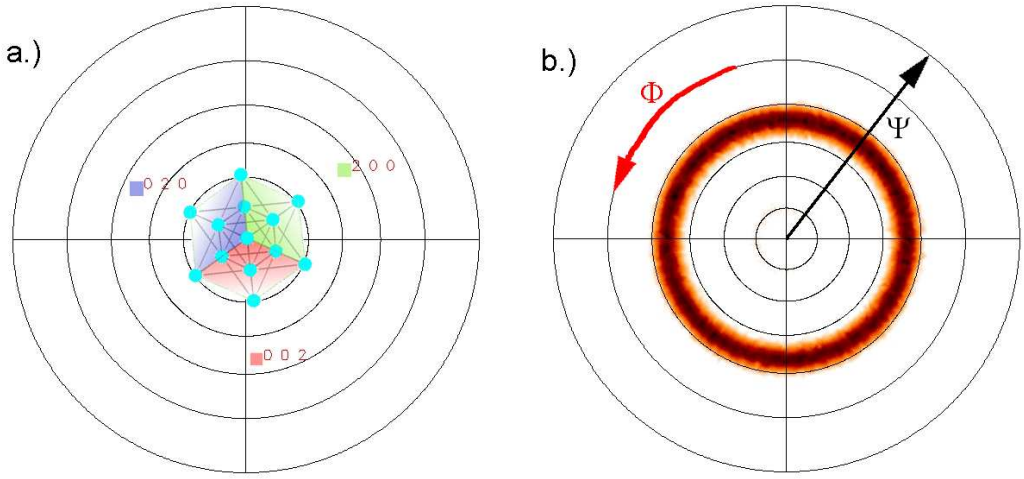

Figure 4.4:a.) stereogram of a cubic single gold crystal with (111) layer parallel to surface **b.)** pole figure of a 2dimensional of gold powde {111} textured with the experimental ψ (range: 0 to 90 degree)and phi (range: 2 to 360 degree)

A peak in a pole figure is called enhanced pole densities and corresponds to a certain pole (see construction in figure 4.3a) and therewith to a certain net plain of the measured crystallite[35].The measured pole figure data set was plotted (see figure 4.4.b) and elaborated with the computer program “Stereopole” [16].

4.1.3. reciprocal space mapping of a 2D-powder

As noted the reciprocal space of a 2D powder is reduced to circles (see figure 3.6). Getting a projection of them like in figure 3.6 is shown, the Psi mapping technique is applied. In this way for a constant φ and varied ψ parameter (see figure 3.9d) by small steps of five degree in a range from -10 degree to 90 degree θ/2θ scans with different 2θ-stepwide were measured at each ψ-position (see figure 4.5a).

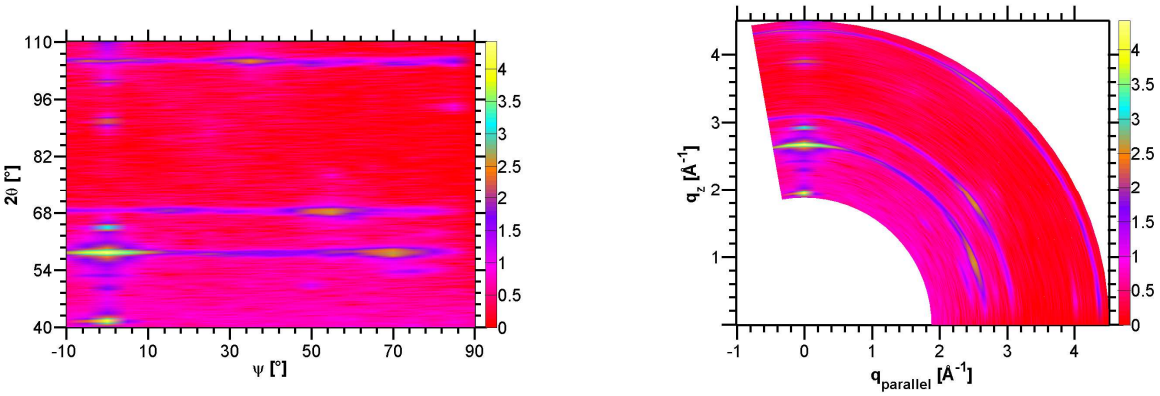

a.)angle space room representation **b.)**reciprocal space represention

Figure 4.5: Psi map of a {111} textured 2D gold powder represented in **a.)** angle space and **b.)** reciprocal space with logarithmic scale of intensity

The measured data set was converted into an ASCI-file containing the measurement conditions as well as the measured intensities saved in a special format. For using the data set of one single θ/2θ scan in Matlab7 and other programs the Matlab7 function “convert” (see Appendix1) was used. This program was programmed by Thomas Haber, TU Graz, and upgraded by Oliver Werzer, TU-Graz. Moreover this function was used in the Matlab script “image_9” (see Appendix1), which was programmed by the author of this thesis himself. This script reads the intensities of each measured 2θ-position for each used Psi position and generates a ψ-2θ Matrix. The generated matrix is saved automatically as a DAT-file with a filename containing sample name, used annealing temperature, and the date doing the experiment. Moreover the Psi map data set is plotted in the angle space room (see figure 4.5.a) as well as in the reciprocal space room(see figure 4.5b) with linear, sqare root and logarithmic scale of intensity. The maps are saved automatically as .jpg files. Comparing all measured Psi maps the program “vergleich_relativ2” (see appendix1) was developed by the author of this thesis. The Matlab script loads the saved data files and normalizes the data set in a way that the highest measured gold peak value is equal with the upper colorbar limit, because sometimes a silicon peak of the used single crystal substrate was higher. And in this case the colorbar was not comparable with a plotted data set without a silicon peak. Moreover the peaks got higher and higher intensities after temperature annealing with higher temperature and hence the colorbar was not comparable again without normalizing the data set. Calculating the theoretical reciprocal space coordinates of a well known unit cell the Matlab7 function “hkl_generation” using formula of Thomas Haber [4]. This function is used in the program “indices4” (see appendix1), programmed from the author of this thesis, to plot the theoretical reciprocal space points of a 2D powder, the crystallite name together with the (hkl) indices as well as the corresponding {hkl} texture.

4.1.4. rocking curves

Rocking curves are an experimental technique quantifying the mosaicity of a 2D powder. When performing a rocking curve the detector (2θ parameter) is fixed, and thus the diffraction angle 2θ is constant. Regarding Bragg´s law one certain net plain distance is chosen by fixing the diffraction angle. A rocking curve is usually performed at a found peak of θ/2θ-scan to check the spatial distribution of the crystallites. This is realized by tilting the sample parallel to the primary beam, qualified by the parameter θ (see figure 3.9d and 4.6), in other words the incident angle. Therefore a rocking curve probes the parallelism condition n||q. As shown in figure 4.6. a rocking curve probes the quality of the crystallites alignment [35]. The rocking curve of a powder (randomly distributed crystallites) will not lead to a peak in a rocking curve instead to a constant intensity. The better the alignment of a 2D powder the smaller is the full width half maximum (FWHM) of the distributed rocking curve peak, so in figure 4.6.

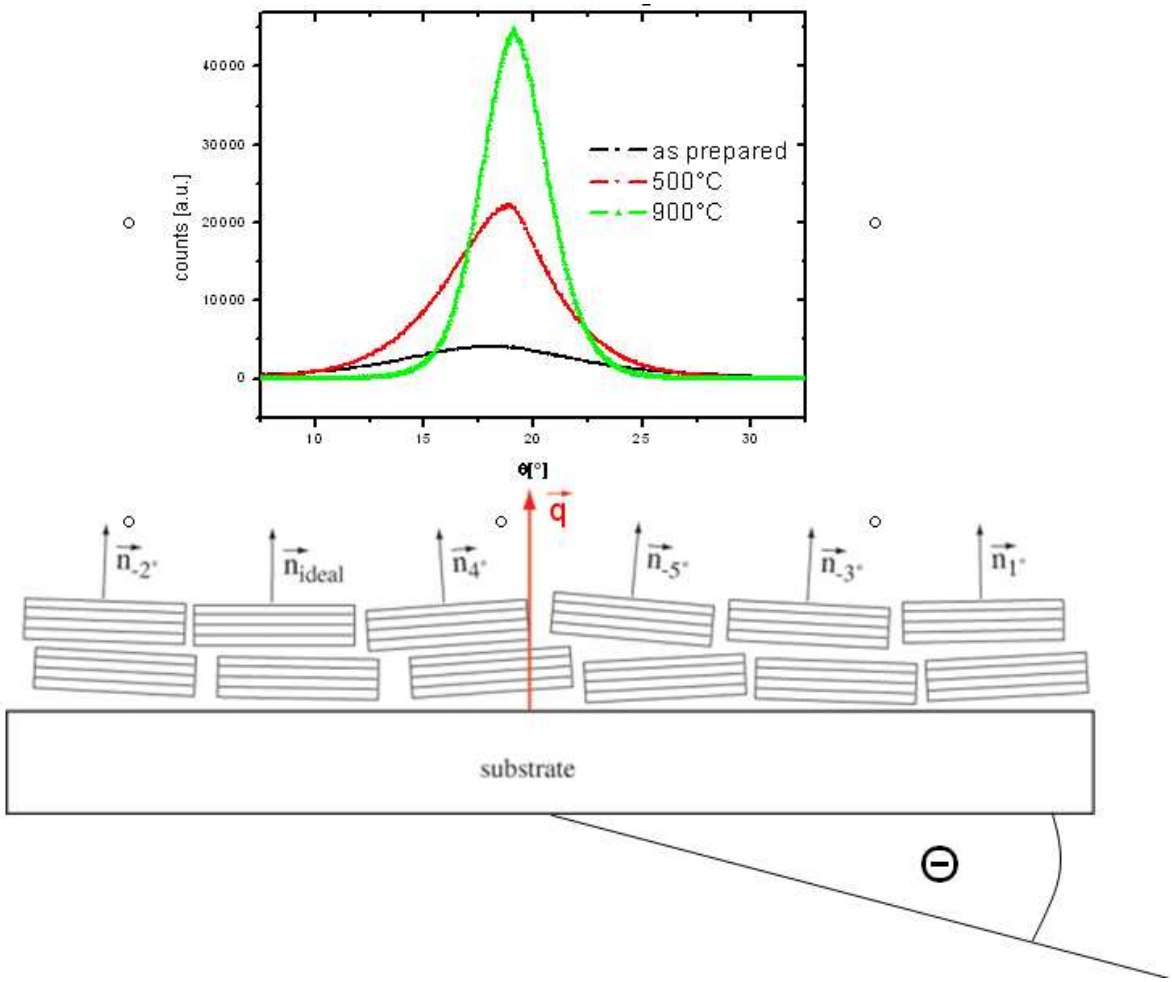

Figure 4.6: Rocking curves by sample tilting, represented by Θ, at a constant detector position (2Θ) of a 2D gold powder. The smaller full width half maximum (FWHM) of the scattering intensity means better common orientation of the crystals.[4]. The displayed measurements in the upper area are rocking curves of gold 111 peak measured ex-situ with three different thermal annealing temperatures.

In example it is simple to see decreasing the FWHM with higher temperature. So the poles will be better ordered. Rocking curves were measured with the Phillips goniometer.

4.2. scanning electron microscopy

The scanning electron microscope (SEM) is a type of electronic microscopic technique scanning the sample surface with a high-energy beam of electrons in a raster scan pattern.
The electrons interact with the atoms. That make up the sample producing signals, which contain information about the sample's surface topography, composition and other properties such as electrical conductivity. Figure 4.7. displays the principle assembling of a SEM together with all included components.

The SEM technique was used in Bratislava measured by A. Šatka (*International Laser Center Bratislava*) scanning the prepared samples (see figure 5.7.) in Bratislava. At second in Graz ex-situ temperature annealed gold samples was scanned by P. Pölt (*Institute for Electron Microscopy, Graz University of Technology*) as well as in-situ temperature annealing SEM technique. The signal producing type of the SEM was made with back scattered electrons (BSE) as well as secondary electrons (SE).

4.2.1.Back scattered electrons (BSE)

Back-scattered electrons (BSE) are beam electrons that are reflected from the sample by elastic scattering. BSE are often used in analytical SEM along with the spectra made from the characteristic X-rays. Because the intensity of the BSE signal is strongly related to the atomic number (Z) of the specimen, BSE images can provide information about the distribution of different elements in the sample. For the same reason, BSE imaging can image colloidal gold labels of 5 or 10 nm diameter which would otherwise be difficult or impossible to detect in secondary electron images in biological specimens.

4.2.2. Secondary electrons (SE)

Secondary electron detectors are common in all SEMs. The signals result from interactions of the electron beam with atoms at or near the surface of the sample. In the most common or standard detection mode, secondary electron imaging or SEI, the SEM can produce very high-resolution images of a sample surface, revealing details about less than 1 to 5 nm in size. Due to the very narrow electron beam, SEM micrographs have a large depth of field yielding a characteristic three-dimensional appearance useful for understanding the surface structure of a sample.

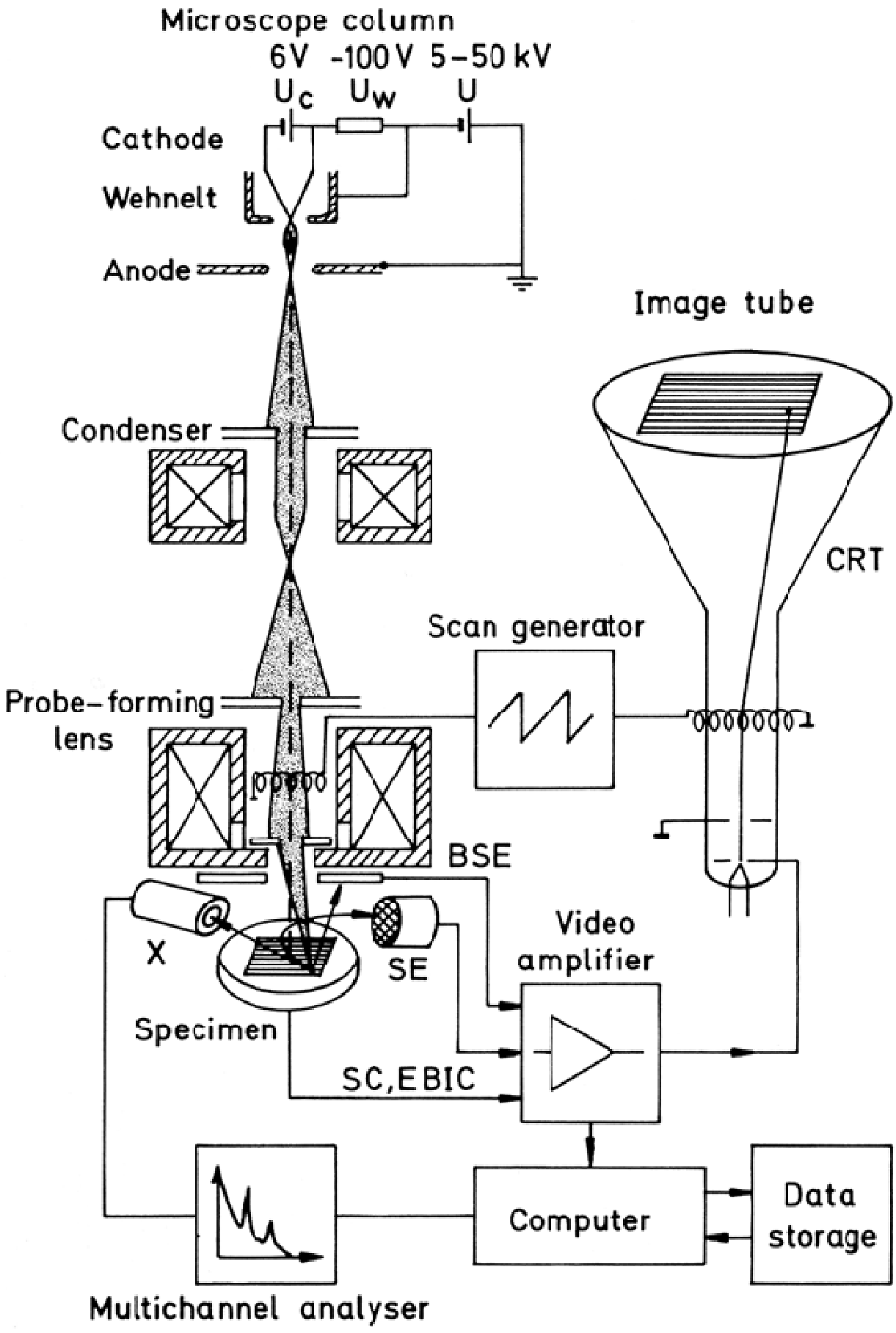

Figure 4.7: principle of SEM (scanning electron microscopy) [37]

4.2.3. SEM in-situ thermal annealing

Getting SEM-images during sample thermal annealing a heating chamber (see figure 4.8a.) was assembled at the specimen place (see figure 4.8a). The heating rate was possible to change. Before starting the heating process vacuum was produced with a protective noble gas preventing any chemical reaction of gold with atmospheric atoms. The sample was put into the left shown specimen holder of figure 4.8b.

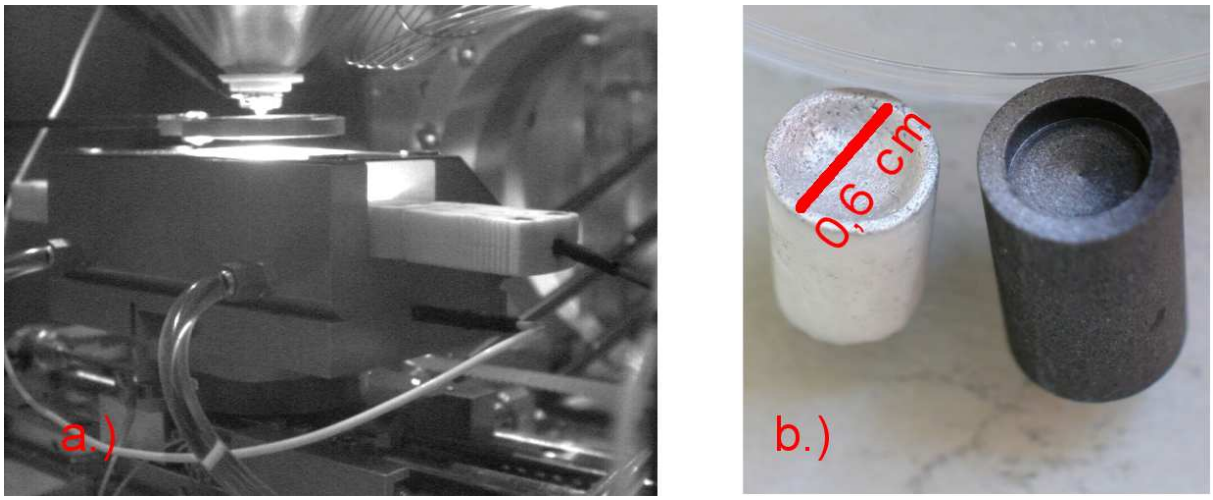

Figure 4.8.: a.) heating chamber of scanning electron microscopy **b.)** specimen holder used for in-situ measuring. Only samples with a diameter of maximal 0.6cm can be heated.

4.2.4. energy dispersive X-ray spectroscopy

Energy dispersive X-ray spectroscopy (EDX) is an analytical technique used for the elemental analysis or chemical characterization of a sample. As a type of spectroscopy, it relies on the investigation of a sample through interactions between electromagnetic radiation and matter, analyzing x-rays emitted by the matter in response being hit with charged particles. Its characterization capabilities are due to the fundamental principle that each element has a unique atomic structure allowing X-rays. They are characteristic of an element's atomic structure to be identified uniquely from one another.

To stimulate the emission of characteristic X-rays from a specimen, a high energy beam of charged particles, such as electrons in SEM, is focused into the sample being studied. At rest, an atom within the sample contains ground state (or unexcited) electrons in discrete energy levels or electron shells bound to the nucleus. The incident beam may excite an electron in an inner shell, ejecting it from the shell while creating an electron hole where the electron was. An electron from an outer, higher-energy shell then fills the hole, and the difference in energy between the higher-energy shell and the lower energy shell may be released in the form of an X-ray. The number and energy of the X-rays emitted from a specimen can be measured by an energy dispersive spectrometer. As the energy of the X-rays are characteristic of the difference in energy between the two shells, and of the atomic structure of the element from which they were emitted, this allows the elemental composition of the specimen to be measured.

Scanning electron microscopes (SEM) are equipped with a cathode and magnetic lenses to create and focus a beam of electrons. A detector, in figure 4.7:called X, is used to convert X-ray energy into voltage signals. This information is sent to a pulse processor, which measures the signals and passes them onto an multi channel analyzer (see figure 4.7) for data displaying and analysing the EDX spectrum with computer (see figure 4.9). Data analysing of all measured probes was made by P. Pölt (*Institute for Electron Microscopy, Graz University of Technology*).

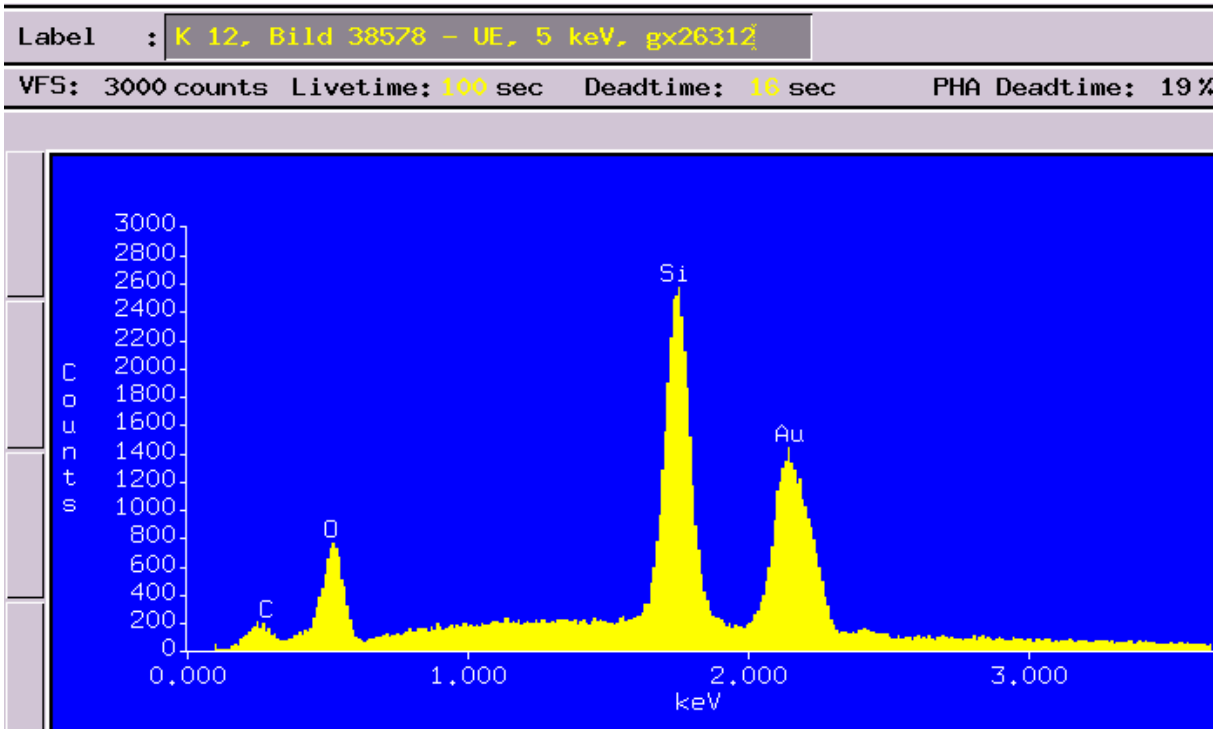

Figure 4.9: EDX spectrum example of a thermal annealed gold sample

4.3.Focused ion beam

Focused ion beam (FIB) is a fundamental technique removing material of a sample surface by highly energy ions combined with a SEM. The used measuring instrument FEI NOVA 200 in figure 4.10 is a combination of an focused ion beam (FIB) etching the sample and a focused electron beam (FEB). Controlling the etching process a digital camera is focused in direction to the sample. Highly energetic Ga ions remove material at the spot of incidence (sputtering).

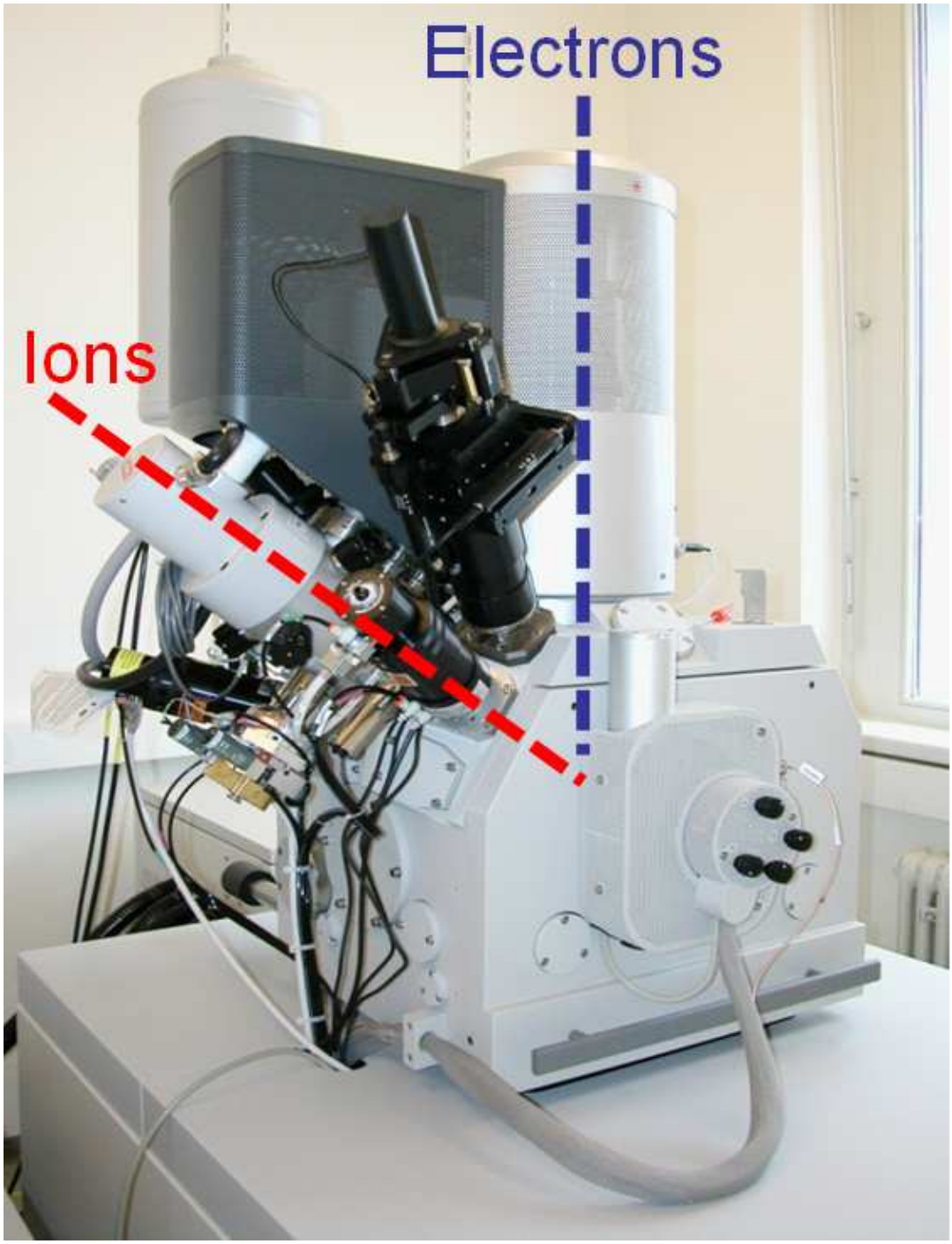

Figure 4.10.: FEI NOVA 200 - Focused ion beam (FIB) and focused electron beam (FEB) combination at the institute for electron microscopy and fine structure research –

Moreover controlled movement and exposure time of the ion beam allows for a three dimensional structuring down to the nanometer scale and simultaneous operation of FIB and FEB allows for an online monitoring of the structuring. Temperature annealed gold samples were measured and analysed by Harald Plank(*Institute for Electron Microscopy, Graz University of Technology*) comparing X-ray technique resulting resolutions.

4.4. thermal annealing

In this chapter all used themal annealing techniques combined with X-ray measurements are described. Ex-situ thermal annealing technique was distributed by Markus Koini and the author of this thesis. Ex-situ X-ray techniques were measured by Heinz Georg Flesch Brucker D8 and the author of this thesis with Phillips powder diffractometer. In-situ techniques were dperformed by Heinz Georg Flesch and Oliver Werzer with the Brucker Discovery D8 diffractometer. All measured data were analyzed by the author of this thesis himself.

4.4.1. ex-situ with DHS 900

Thermal annealing ex-situ investigations are proceeded in the following sequence: a sample is heated by a heating chamber at a special constant temperature for a special time span. After cooling procedure different sample investigations will be done.
The Domed Hot Stage (DHS) 900 was developed by Anton Paar and has analogical construction like DHS 1100 shown in figure 4.11 leftwards. Normally it is designed for using on X-ray diffractometers. So the sample is covered by a dome, which is made of carbon and is permeable for X-rays.
In this work the DHS 900 only was used as heating chamber up to 900 degree Celsius outwards of X-ray diffractometer. Argon was used as inert gas. After thermal annealing sample measurement techniques like Psi-mapping, Rocking curves, Specular Scan and atomic force microscopy (AFM) were applied. Further with some special samples measurement techniques like scattering electron microscopy (SEM), focused ion beam (FIB), and X-ray reflectivity were investigated after thermal annealing with DHS 900..

4.4.2. in-situ with DHS 1100

The difference of thermal annealing in-situ versus ex-situ investigations is the time point of investigating sample measurements. Thermal annealing in-situ investigations are measured during heating procedure. All In-situ investigations were made with Brucker Discovery D8 diffractometer together with DHS1100. The Domed Hot Stage (DHS) 1100, in figure 4.11 leftwards, was developed by the Institute of Solid State Physics, Graz University of Technology, together with Anton Paar GmbH and is a further development of the predessor model DHS900. It is designed for the use on four circle diffractometers and it allows temperature dependant X-ray structure analysis up to 1100℃ [2].
Thermal annealing In-situ investigations were made in 100℃ steps up to 900℃. Applied measuring techniques were specular scans and rocking curves.

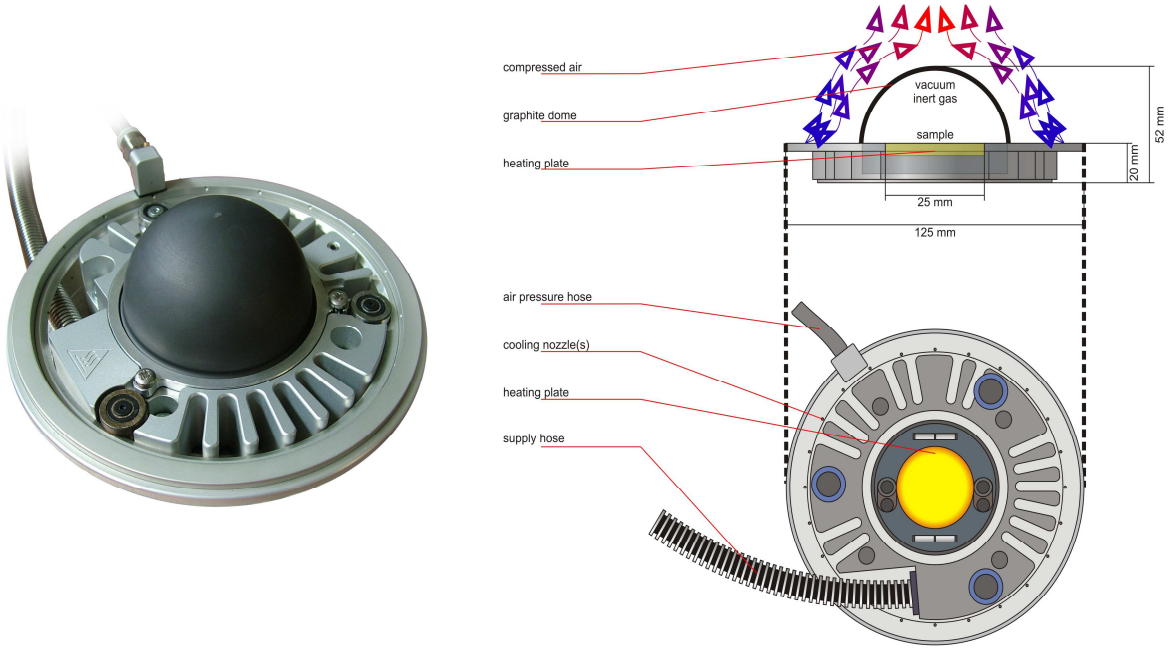

Figure 4.11.: heating chamber DHS 1100 [2] from the company Anton Paar Graz (left) and a sketch of the construction in topview and side view (right)

V.Materials and properties

5.1. Motivation

The aim of this work was analyzing structure-, size-, strain-, and morphology changes of {111} textured 2D gold powder while (in-situ) and after (ex-situ) thermal annealing procedure. Therefore in this chapter the fundamental sample materials, gold as well as the used substrate, thermal oxidized silicon, and their fundamental properties are described. Moreover all prepared samples and their preparation conditions are displayed.

5.2. Gold

The chemical element gold (Au) is a noble metal with order number 79 within the periodic table. The chemical element notation Au of gold is leaded off of the Latin name Aurum. There exists only one isotope of gold. The unit cell of gold crystals has a face centered cubic

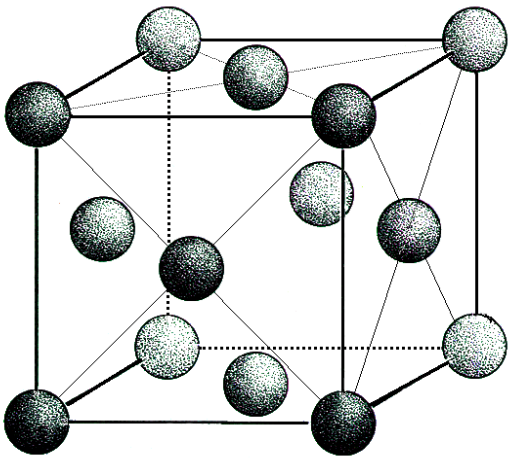

Figure 5.1: A1-type, face centred cubic lattice structure of gold [5]

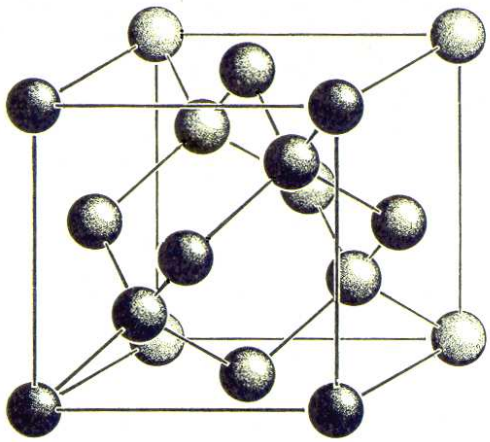

Figure 5.2: A4-type, two displaced face centred cubic structures - lattice structure of silicon [5]

lattice, also known as A1-type (see figure 5.1).The lattice parameter of gold is often determined with different experimental investigations in literature. In this work the lattice constant a=4,07894Å, published by E.Straumanis [1] 1971, was used in all calculations. At first this was one of the newer lattice parameter calculations of gold in literature. The second reason using this parameter was the good correlation of the first X-ray measurement and the corresponding calculated theoretical pattern with this parameter. Moreover Straumanis also calculated the thermal expansion coefficient of gold, which was also calculated in this work

5.3. substrate

The used substrates for all prepared samples were thermal oxidized silicon (100) single crystals. So the silicon crystallite layers orientated parallel to substrate surface are the (h00) layers. The Silicon lattice structure, shown in figure 5.2, is a face centred cubic cell, called A4-type. The lattice constant of silicon in literature is equal 5,430825 Å [8]. Specifying the thickness of the grown oxide layer on silicon single crystal a XRR (X-ray reflectivity) investigation was made. In figure 5.3 the measurement data as well as the fit are displayed together with resulting calculated oxide layer thickness of 39,5nm.

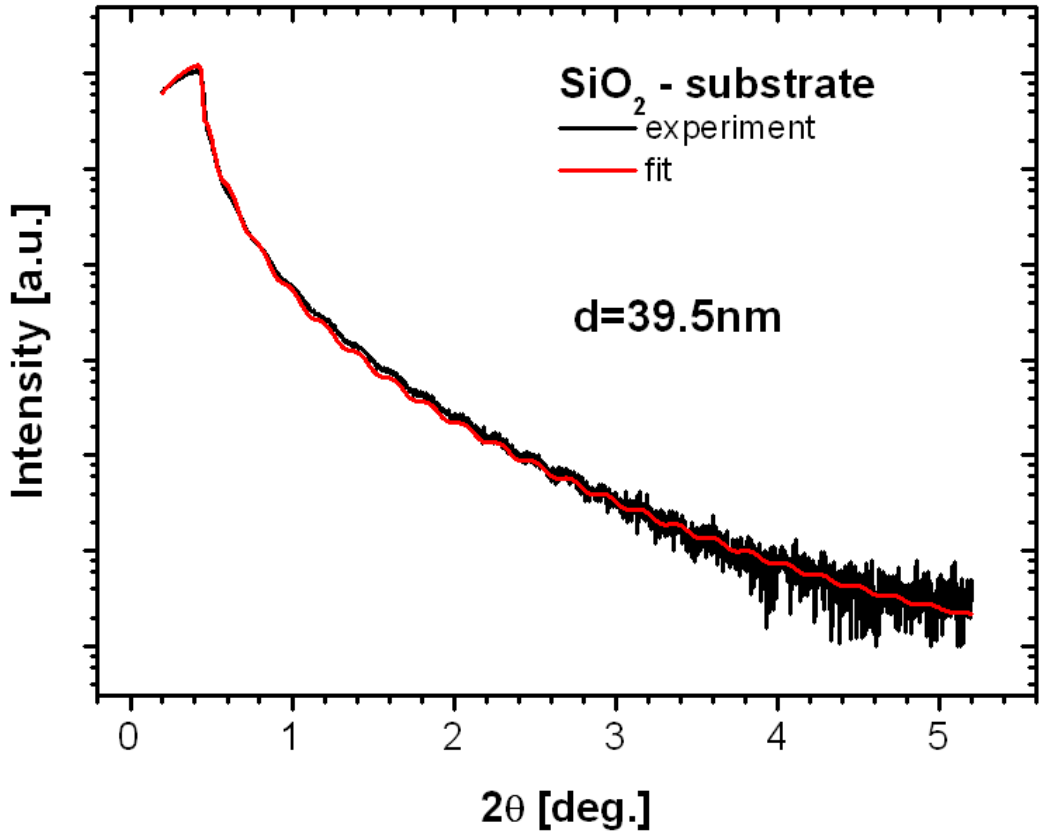

Figure 5.3: XRR (X-ray reflectivity) measurement of the used substrate in this work

5.4. sample preparation

All prepared gold samples were made by a evaporation technique whereas always the same thermal oxidized silicon substrate and the same gold resource were used. The substrate was cut by hand with a size of 2x2cm First samples named K10, K11, K12, K13, K14, K15 K16, and k17, were prepared in Bratislava on Department of Microelectronics. In addition gold samples, named with K and higher counter than 17, were prepared in Graz by myself.

5.4.1.sample preparation in Bratislava

sample	K 10	K 11	K 12	K 13	K 14	K15	K 16	K 17
plasma etched	no	no	no	**yes**	**yes**	**yes**	yes	yes
p [10^{-6} Torr]	5.5	5.4	5.5	5.5	5.4	5.5	5.5	5.5
$T_{substrate}$ [°C]	24 °C	24 °C	24 °C	24 °C	24 °C	24 °C	**56 °C**	**56 °C**
d_{mb} [nm]	**20nm**	**50nm**	**100nm**	**20nm**	**50nm**	**100nm**	**100nm**	**100nm**
dep. rate [nm/s]	0.041	0.109	0.104 (0,051)	0.041	0.109	0.104 (0,051)	0.104 (0,051)	0.104 (0,051)

Tab.5.4: sample preparation conditions of all samples.(p…pressure, T…temperature, d_{mb}…gold thickness measured by micro balance while evaporating, dep. Rate…average deposition rate of the gold layer)

All samples shown in table 5.4 were made of J. Jakopovič (*Department of Microelectronics*) in Bratislava. So by thermal gold evaporation three different thickness of gold layer samples were produced. The thickness of the gold layer in table 5.4 was measured with micro balance technique during evaporation. Of every thickness two samples were prepared with different substrate cleaning technique but under same evaporating conditions, so one sample series was cleaned by plasma etching (see table 5.4). Well known is the fact the lower the deposition rate the better evaporated layer textured will be. Therefore the deposition rate was minimized as possible. In figure 5.5 development of gold layer thickness is plotted about the deposition time. It is clearly to see that all 100nm gold samples of Bratislava were evaporated in two serial evaporating sections. Therefore in table5.4 exists two different deposition rates of these samples. Bracketed deposition rate symbolizes the second evaporating section. As known the higher the substrate temperature while evaporating process the greater grain size will exist on the finished sample after evaporating process.

Therefore two samples ,K16 and K17 in table 5.4, were assembled with higher substrate temperature of 56℃ while the evaporating process.

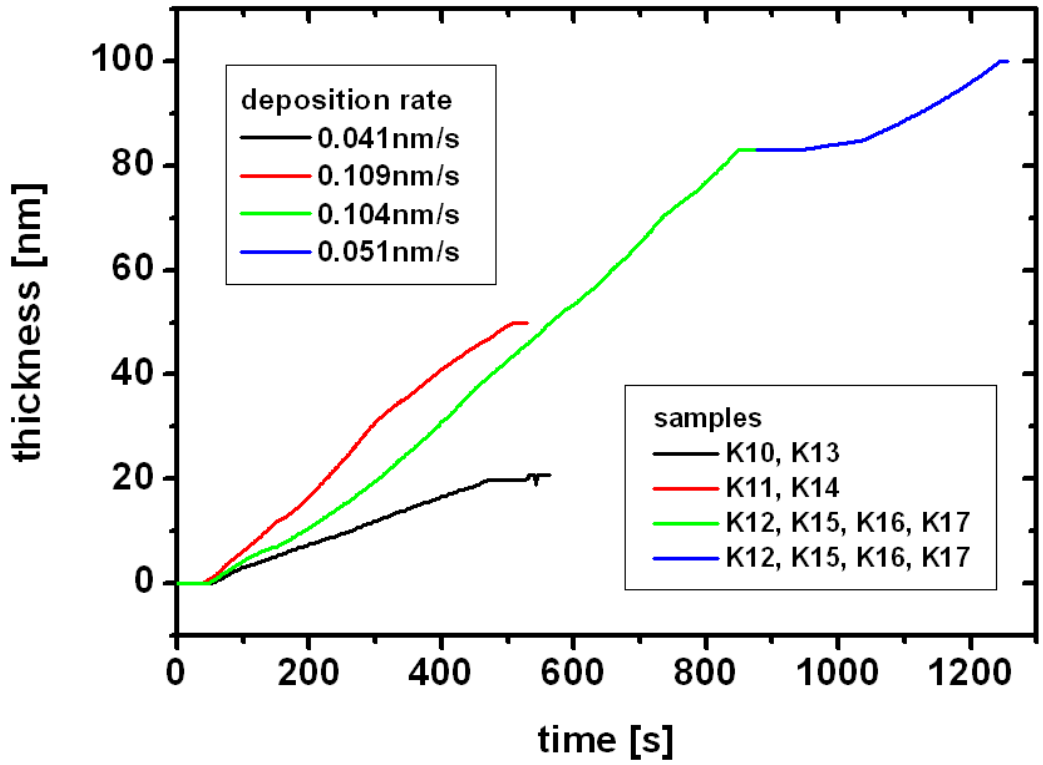

Figure 5.5: deposition rate as a function of deposition time of all samples prepared in Bratislava. The 100nm samples were evaporated with a small break. Therefore the deposition rate is presented by two different colours

After the sample preparation AFM (atomic force microscopy) and SEM (scanning electron microscopy) investigations were made in Bratislava. In figure 5.6 AFM images, made by D.Haško (*International Laser Center Bratislava*), are depicted. The SEM images were made by A. Šatka (*International Laser Center Bratislava*) and are displayed in figure 5.7. At first it is clearly observable that the samples with plasma etched substrate (right side of figure 5.6 and5.7) don't have large morphology differences. By contrast the different gold thickness show very well morphology differences. So only on the 20nm samples grooves into the gold layer were found. The thicker the gold layer the greater are the gold grains and therefore the layer roughness.

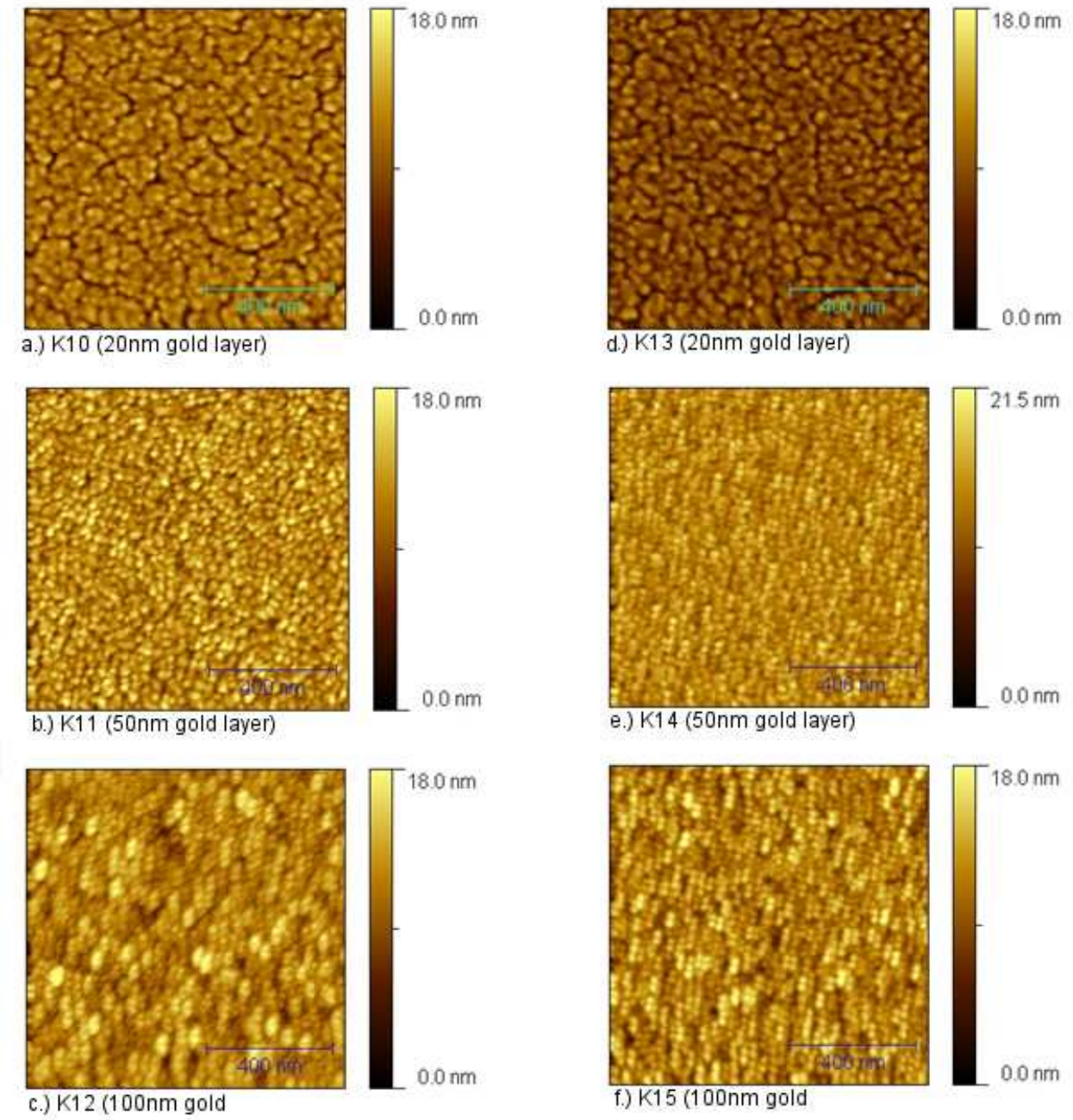

Figure5.6: Atomic force microscopy images of the evaporated gold samples. On the left side the samples without **(a-c)** and on the right side with plasma etched substrate **(d-f)** are shown.

All said conclusions can also made by the following SEM images, so the grooves of the 20nm gold layer samples as well as the other grain morphology of the 50nm and 100nm gold layer samples. The more homogeneous surface of the thicker gold layer samples is also observable. Contrary to other materials gold layers are generated while evaporating by hill growth. So in the beginning small gold hills in certain distances grow on the substrate surface until they are as great that they are docking together. At this moment firstly the substrate surface is covered by a contiguous gold layer.

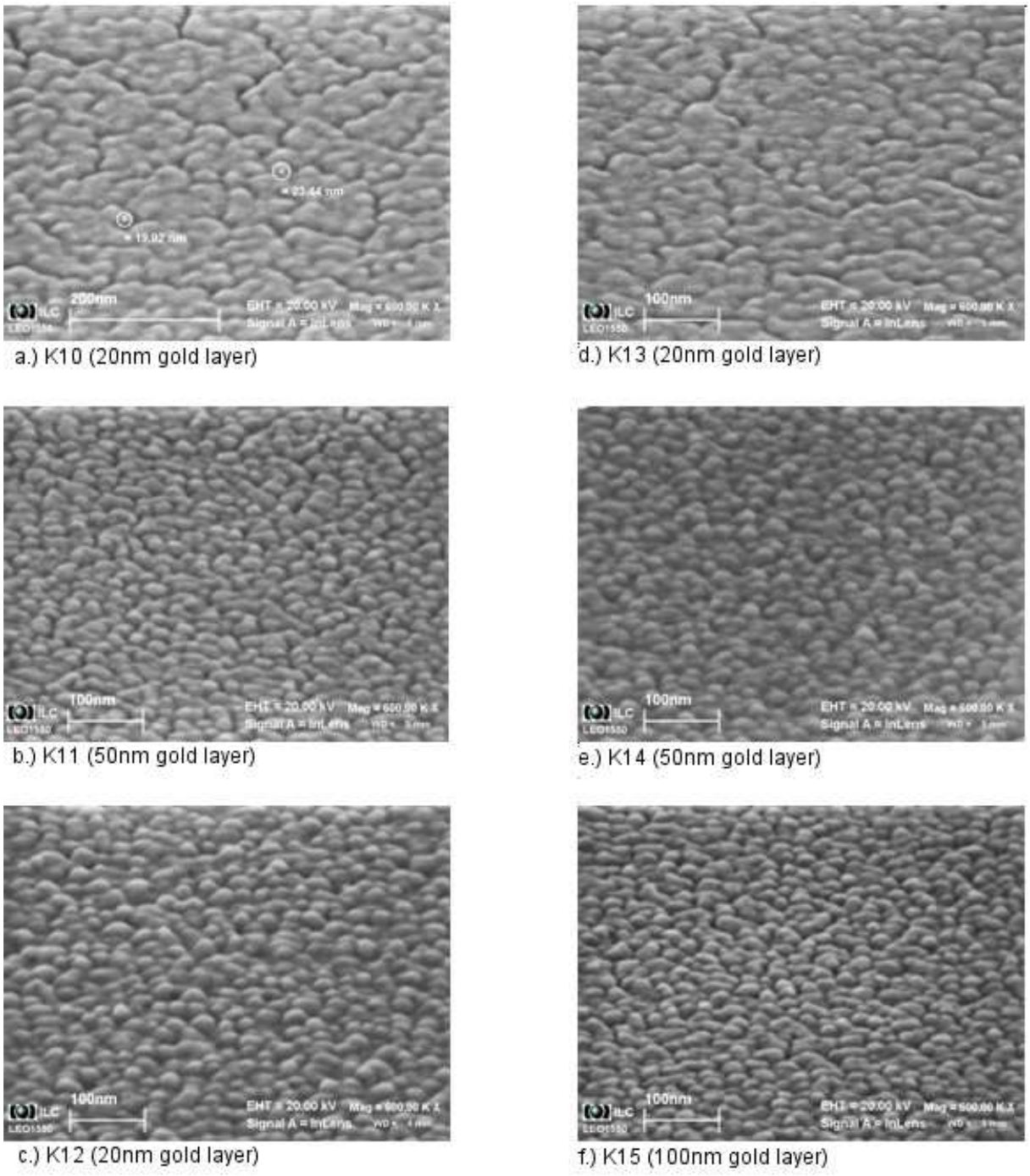

a.) K10 (20nm gold layer)

d.) K13 (20nm gold layer)

b.) K11 (50nm gold layer)

e.) K14 (50nm gold layer)

c.) K12 (20nm gold layer)

f.) K15 (100nm gold layer)

Figure 5.7: Scanning Electron Microscopy images of the evaporated gold layers. On the left side the samples without **(a - c)** and on the right side with plasma etched substrate **(d - f)** are shown.

The hill growth of gold can be reproduced by the SEM images in figure 5.8 and 5.9. They were investigated at sample positions which were covered partially while thermal gold evaporating.

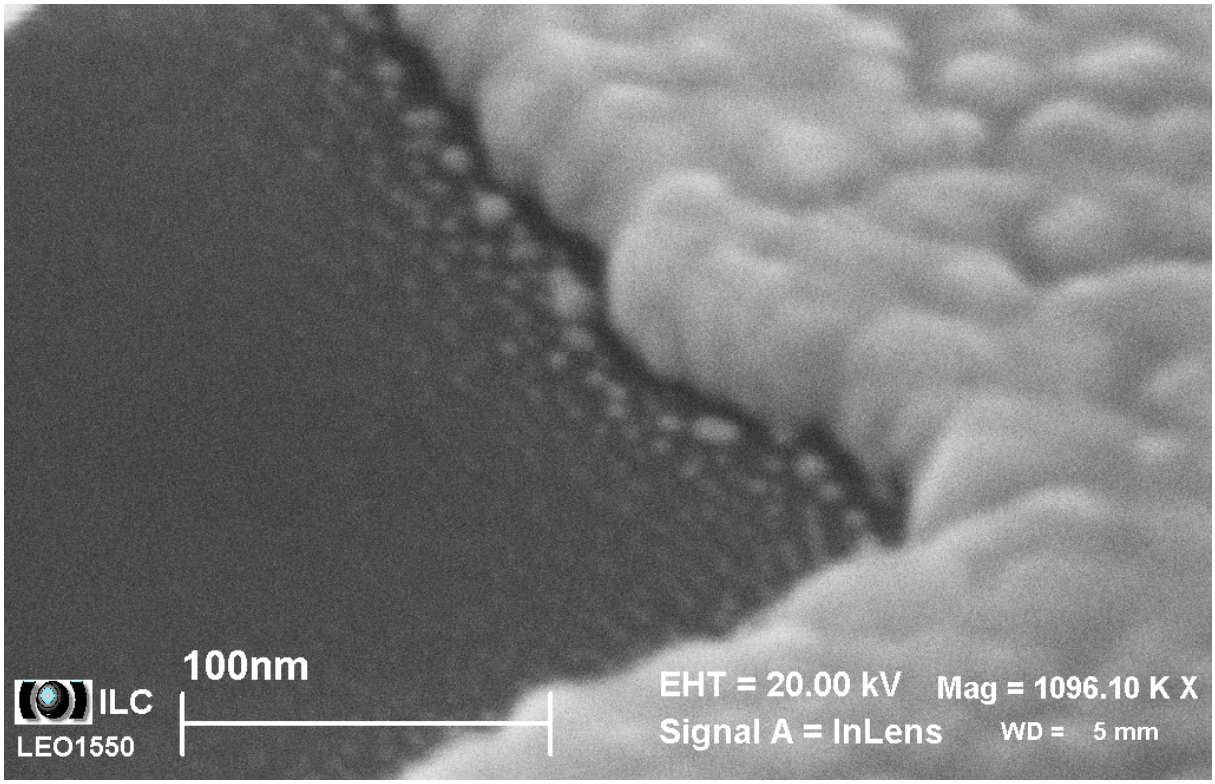

Figure 5.8: SEM image of sample K13 (20nm) as prepared at only partially covered area.

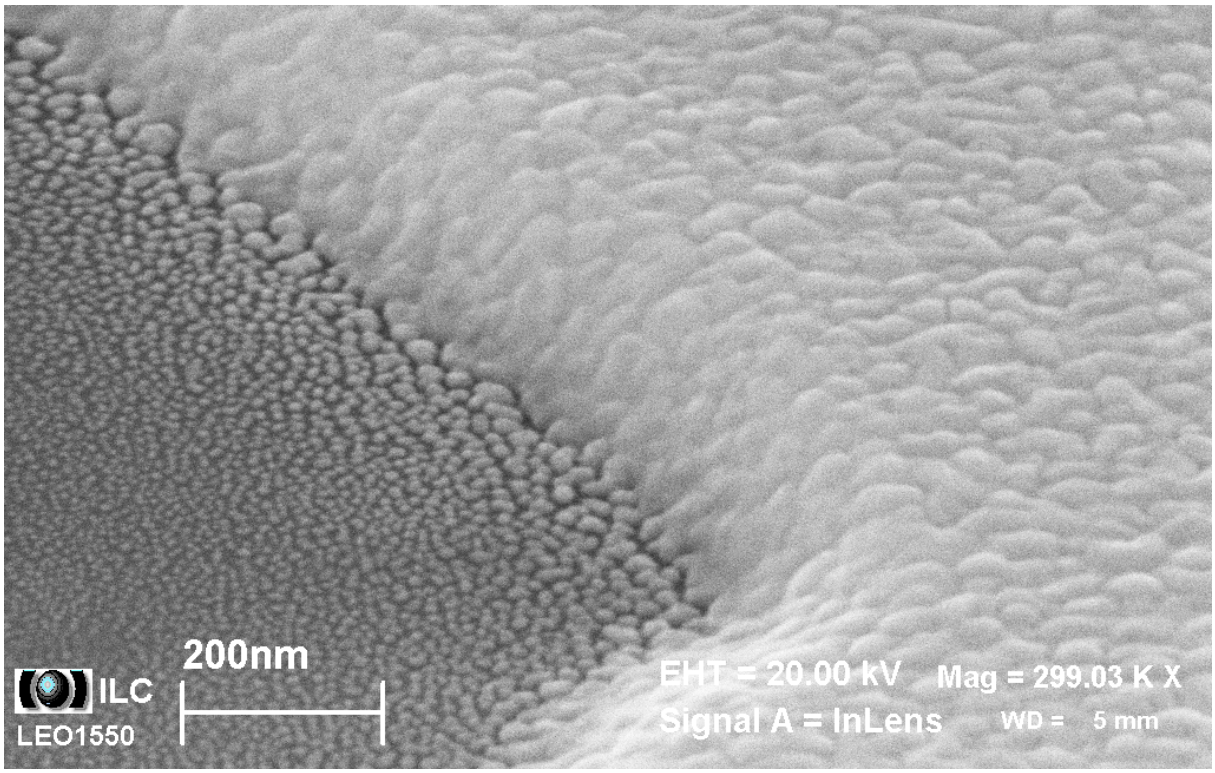

Figure 5.9: SEM image of sample K16 (100nm) as prepared at an area covered during the deposition process.

In Graz XRR (X-ray reflectivity) investigations of two samples as prepared were made by Heinz Georg Flesch specifying special characteristics like gold layer thickness and surface roughness. The experimental data of these measurements as well as the corresponding calculated fitting function are displayed in figure 5.10a and 5.10b. Because of the higher roughness of the thicker gold layer sample K12 no exact fitting function was possible to determine. Therefore the calculated roughness of sample K12 have a very great error interval. But then the error interval of the calculated thickness do not transcend however the value of 2nm. So a very interesting result of these investigations is the conclusion that the real gold layer thickness is around one and a half thicker than with micro balance technique while evaporating process measured value(see table 5.4).

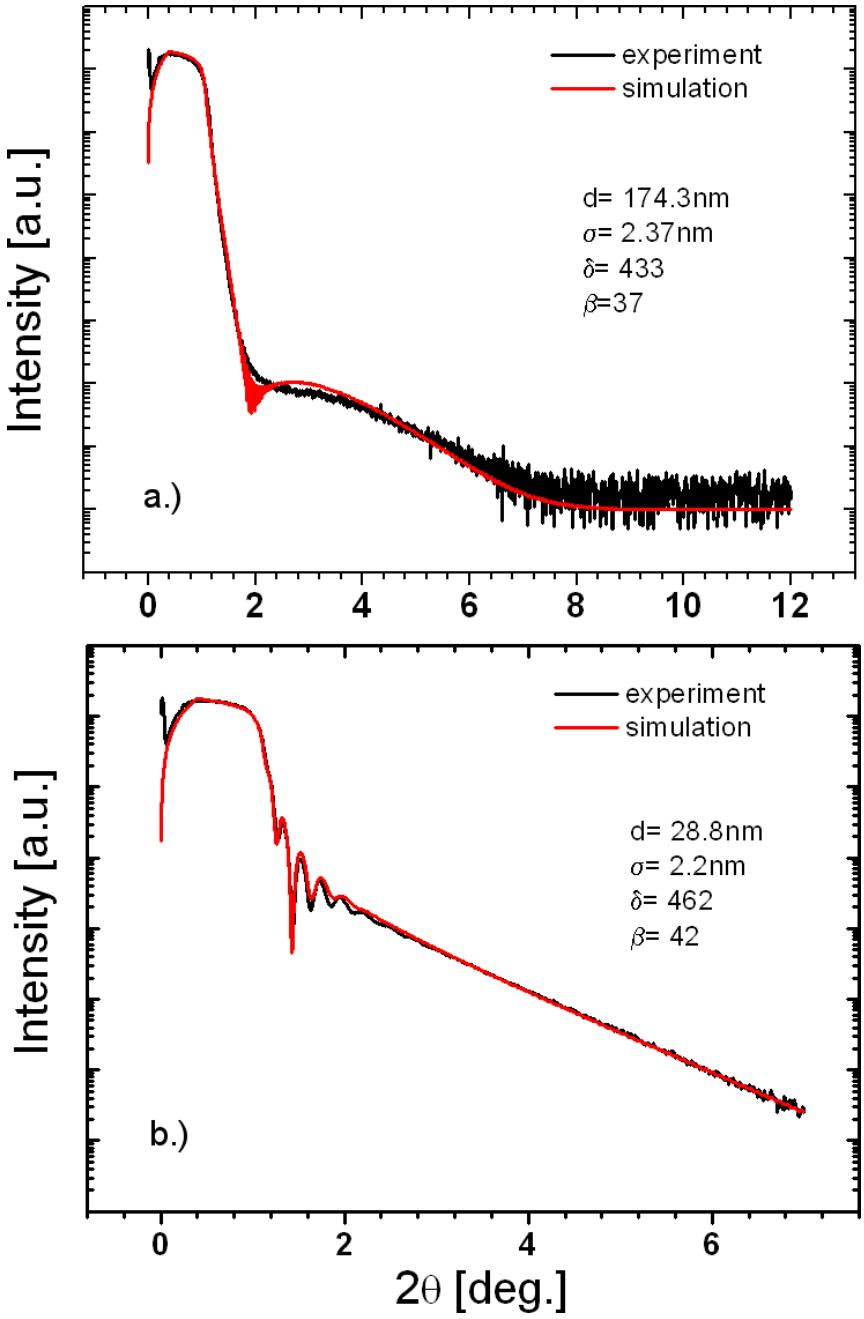

Figure 5.10: XRR (X-ray reflectivity) measurement of the samples **a.)**K12 and **b.)**K13 reveal the real layer thickness of the gold layer (d..layer thickness, σ..roughness, δ..average electron density, β..X-ray absorption)

Moreover material composition and 2D characteristics of all samples were studied. So specular scan technique was investigated with Phillips X-ray diffractometer with Cr-radiation identifying all sample materials. In figure 5.11 all measured data of these investigations are displayed, while the yellow lines in figure 5.11 symbolize the theoretically calculated 2θ values with the program Powdercell for an experiment with Cr radiation. Powdercell uses international known database of materials and their unit cell parameters calculating the theoretical 2θ values. It is also possible to change the parameters of a selected unit cell. So done with gold unit cell using the measured parameters from Straumanis [1]. 2θ interval from 40 degree to 110 degree was selected for the specular scan because all gold identifying peaks exist in this interval

under condition of using Cr-radiation. Moreover the program Powdercell also calculates the theoretical intensity relations between all diffraction peaks, which are reasonable because of two important facts. At first the diffraction area in unit cell is different for each hkl-peak. At second, diffraction peaks are enabled by the right layer distance. For example the diffraction condition don't differences between (200) and (020) layer because of the same distance in case of cubic unit cell. Therefore some layers have a greater multiplier than others and so on a greater intensity in case of a powder. The measured intensity of 111 gold diffraction peak is determined with higher intensity in relation to the other gold diffraction peaks as theoretically calculated. Finally the conclusion of an {111} textured 2D powder at all samples was made. Checking this conclusion by investigations with pole figure technique was done for all samples. In figure 5.12 the polefigures of two samples are displayed. At first all samples were determined with {111} and {511} texture. Higher temperature of substrate during evaporating (K16) leads to a stronger {111} texture and more scattering volume. Because of the same scale ranges the right figures in figure 5.12 are a little sated at some areas.

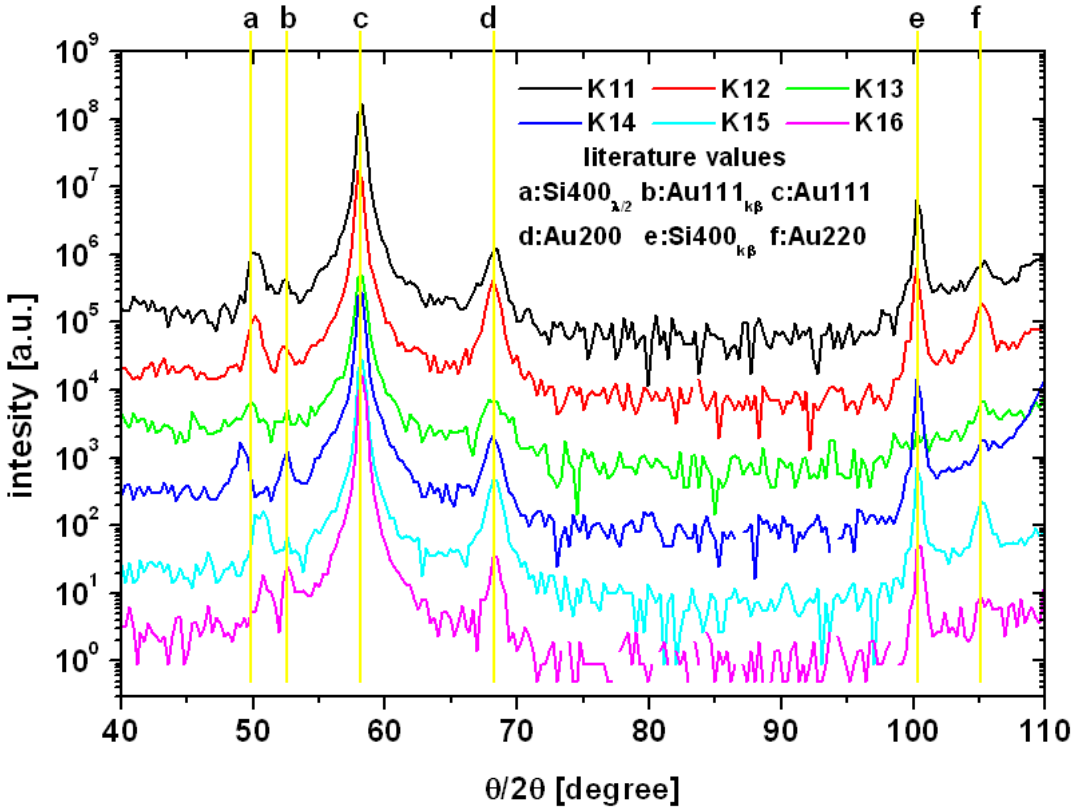

Figure 5.11: specular scans with Cr-K_α radiation. The expected peak (gold + higher harmonics + K_β of 100 silicon) positions are symbolized by the yellow lines.

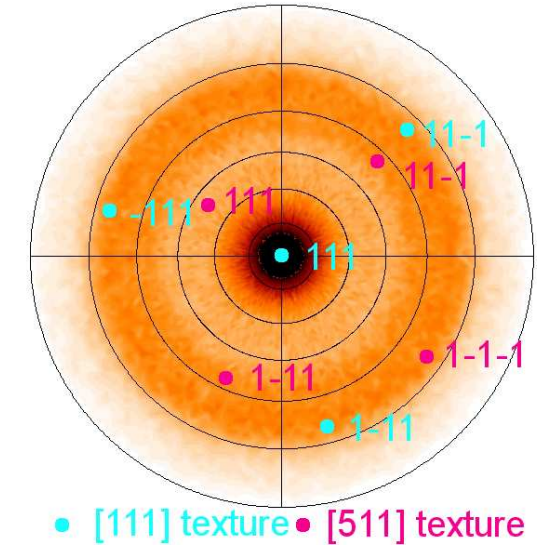

a.) K12 $(111)_{Au}$ - 2Θ=58,3°

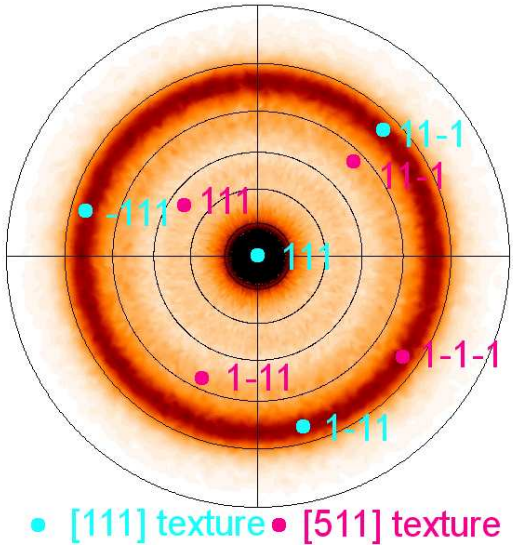

d.) K16 $(111)_{Au}$ - 2Θ=58,31°

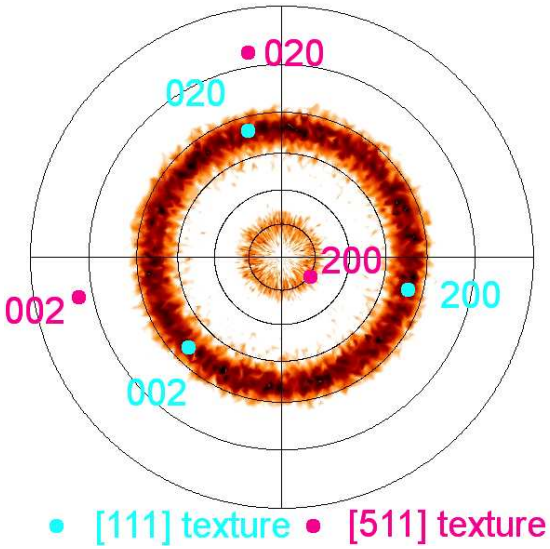

b.) K12 $(200)_{Au}$ - 2Θ=68,4°

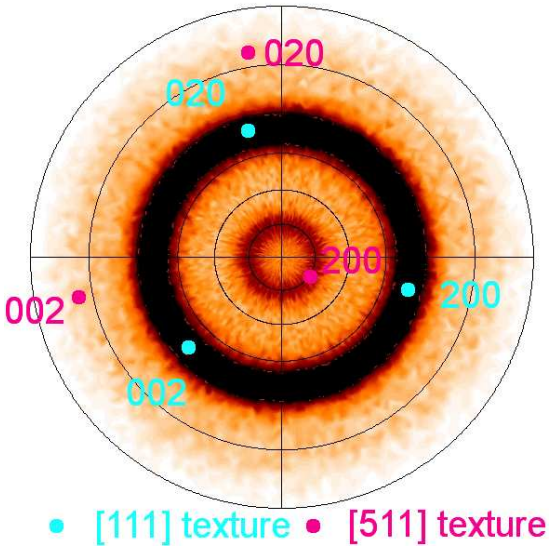

e.) K16 $(200)_{Au}$ - 2Θ=68,46°

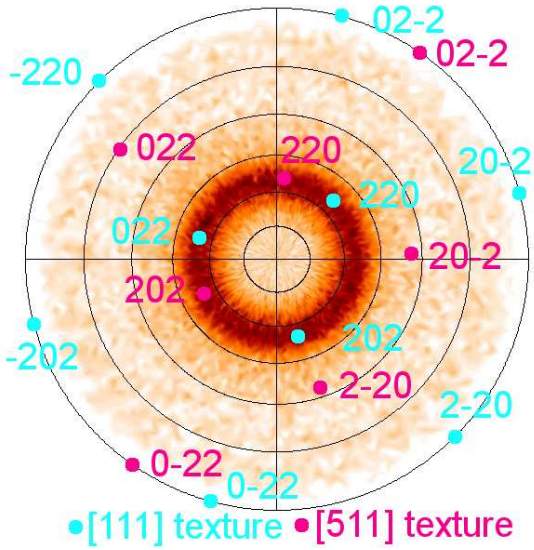

c.) K12 $(220)_{Au}$ - 2Θ=105,4°

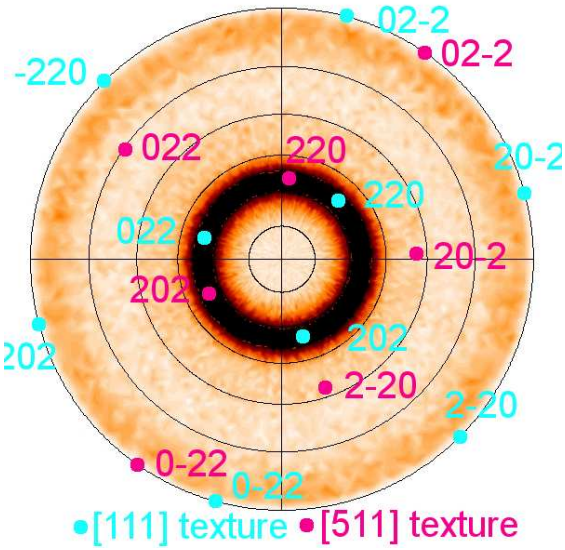

f.) K12 $(220)_{Au}$ - 2Θ=105,41°

Figure 5.12: {111}, {200}, and {220}.polefigures of the 100nm gold samples K12 (left) and K16 (right) as prepared, measured with Cr-radiation

5.4.2.Sample preparation in Graz

All samples named by K and higher counter number than 17 are made in Graz University of Technology on Institute of Solid State Physics by K.R.Marguc and M. Postl. Moreover all these samples have the same gold layer thickness of 100nm, measured with micro balance technique while thermal evaporating process. As more the same silicon substrate and the same gold resource like in Bratislava made samples were used. One special sample was made getting higher adhesion force between gold layer and substrate studying if the macroscopic morphology changes after heating at five hundred degree Celsius will also exist like on samples with only evaporated gold layer, no chrome layer, and smaller adhesion force. Therefore between silicon substrate and gold layer a 5nm chrome layer was evaporated by the same technique like gold layers. The name of this sample is K20 (see table 5.13). Of all gold samples as prepared investigations like specular scans, pole figures and ψ-maps were made with Phillips diffractometer by author of this thesis. All samples were after preparing {111} and {511} textured, so more the sample K20 with a 5nm chrome layer between substrate and the 100nm gold layer. But in figure 5.14 it is visible that this sample K20 is clearly smaller textured than the other gold layer samples. Moreover in figure 5.14 pole figures of only one 100nm gold layer sample are displayed because this sample was used for SEM (scanning electron microscopy) in-situ measurements. The samples prepared in Graz were used for SEM (scanning electron microscopy) in-situ investigations studying the morphology changing process while sample heating above five hundred degree Celsius (see next chapter).

sample	K18+K19	K20	K21	K22+K23	K24+K26
plasma etched	no	no	no	no	no
substrate	SiO_2	SiO_2	SiO_2	SiO_2	SiO_2
p [10^{-6}mBar]	5,7	5,7	5,7	3,0	5,5
$T_{substrate}$ [°C]	room temperature				
$d_{mb,Cr}$ [nm]	0	5	0	0	0
$d_{mb,Au}$ [nm]	100	100	104	15+85	100
dep. rate [nm/s]	0,52	0,27	0,46	0,03	0,022
dep. rate [nm/s]				0,11	

Table 5.13 : sample preparation conditions of samples made in Graz. (p…pressure, T…temperature, d_{mb}…gold thickness measured by micro balance while evaporating, dep. Rate…average deposition rate of the gold layer)

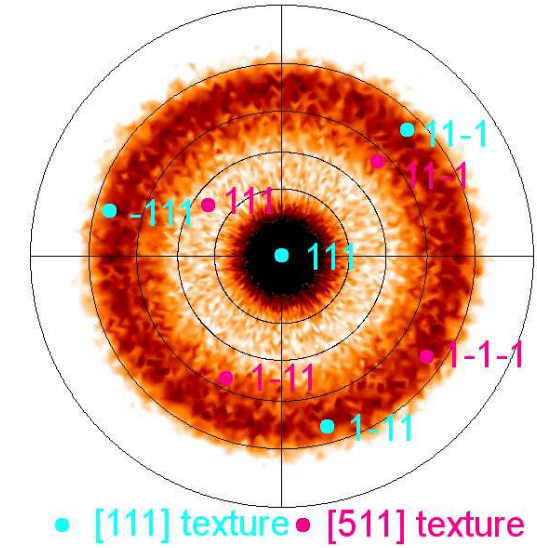

a.) K19(111)$_{Au}$- 2Θ=58,3

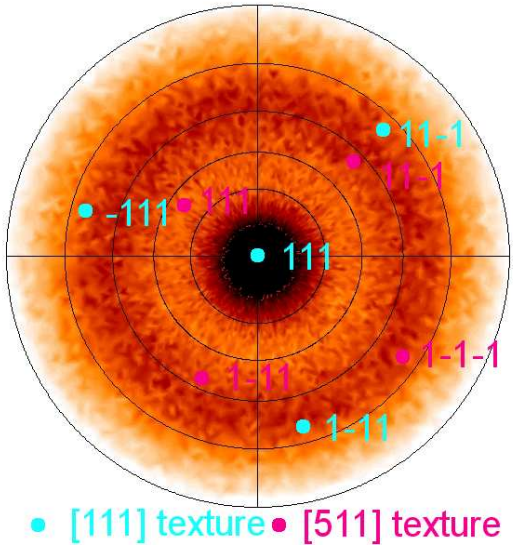

d.) K20(111)$_{Au}$ - 2Θ=58,3

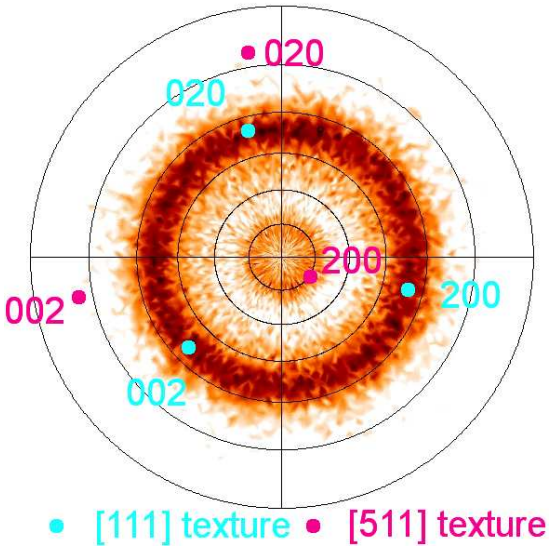

b.) K19(200)$_{Au}$ - 2Θ=68,4

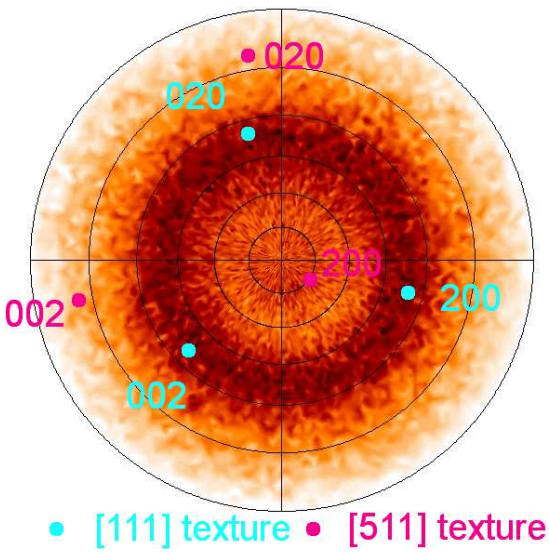

e.) K20(200)$_{Au}$ - 2Θ=68,4

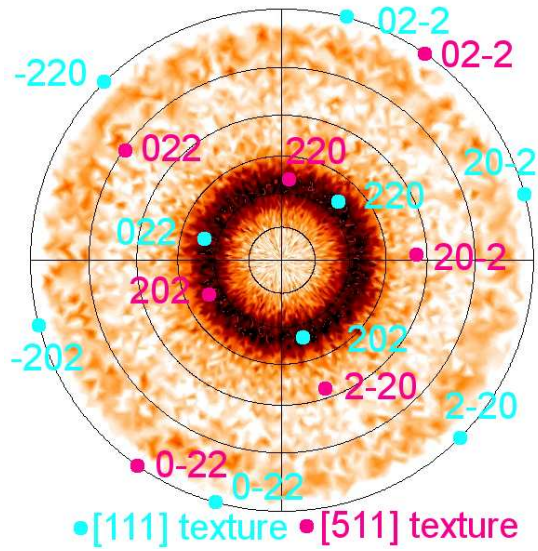

c.) K19(220)$_{Au}$ - 2Θ=105,4

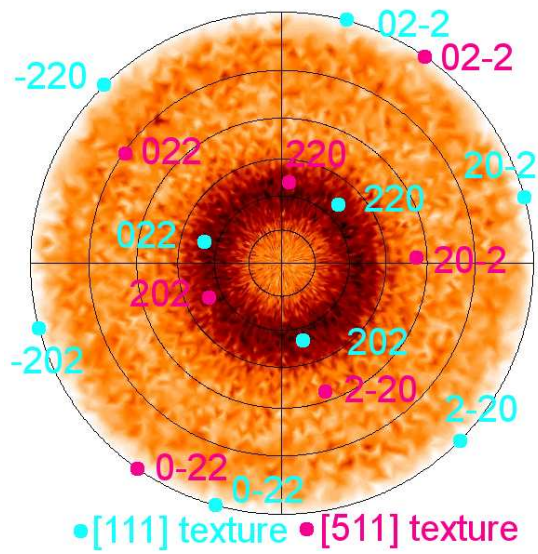

f.) K20(220)$_{Au}$ - 2Θ=105,4

Figure 5.14: **a.+d.)** 111-, **b.+e.)** 200-, **c.+f.)** 220-.polefigures of only gold layer sample K19 (left) and 100nm gold sample K20 (right) with Cr layer as prepared measured with Cr-radiation

VI. Results

In this chapter the most significant investigation results are displayed. Other investigations of this diploma thesis are discussed and compared. In principle this chapter is subdivided in the following sections:

- Ex-situ thermal annealing investigations based on X-ray diffractometer techniques
- In-situ thermal annealing investigations based on X-ray diffractometer techniques
- SEM (scanning electron microscopy) investigations
- Conclusions

Other used techniques like AFM (atomic force microscopy), focused ion beam, and optical microscopy are noted in particular sections of this chapters if their results are significant.

6.1. ex-situ investigations with DHS900

All samples were thermal annealed with DHS 900 with constant temperature along a special time sequence.Before the thermal annealing process was started all samples were analysed as prepared. So θ/2θ-, ψ-map, anf pole figure investigations were made analysing composition and crystallite orientation. A 2D powder characteristic with strong {111}- and small {511} texture were found about all samples as prepared. In figure 6.1a.)-c.) polefigures of 100nm gold sample K15 are representing the so called texture. These polefigures are also representative for all other samples. The only found differences are the strongness of the texture. So for example the less thicker 20nm gold sample K10 was stronger textured as prepared. At first sample 100nm gold sample K15 was annealed in 100℃ steps up to 900℃ with twelve hours thermal annealing time per step. After thermal annealing process with 500℃ a macroscopic morphology change was found on sample K15. Therefore other 100nm gold samples as well as a sample with 5nm Cr layer under 100nm gold layer (sample K20) were thermal annealed with 500℃ with different thermal annealing time. So significant results of these ex-situ investigations are represented and compared on the following pages.

6.1.1. sample K15

As in the beginning noted the 100nm gold sample was thermal annealed in 100℃ steps up to 900℃ with annealing time of twelve hours. After every thermal annealing step the following ex-situ investigations were made: θ-maps were measured with Phillips X-ray diffractometer. Specular scans and rocking curves were measured with Brucker Discover D8 X-ray diffractometer by H.G.Flesch as well as AFM (atomic force microscopy) images. Moreover after 500℃ thermal annealing step optical microscopy images were measured because of the found macroscopic morphology changes. In figure 6.1a.)-c.) it is clearly to see the strong {111} and small {511} texture. In the end a strong {111} and {200} texture was found (see figure 6.1 d.)-f.).

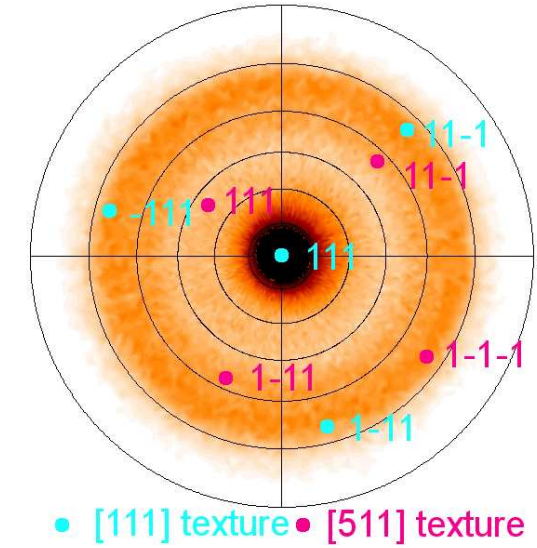

a.) K15(111)$_{Au}$ as prepared 2Θ=58,3

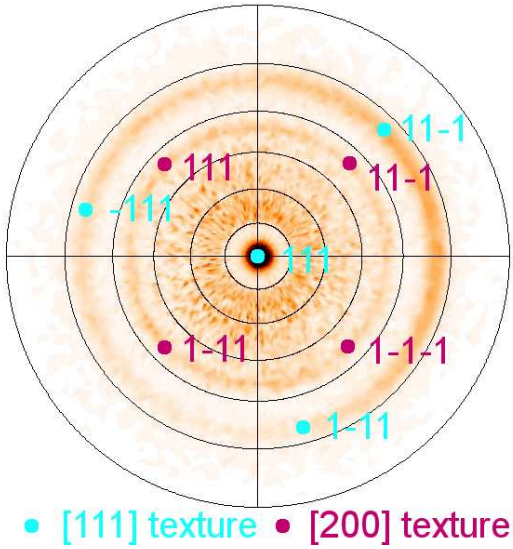

d.) K15(111)$_{Au}$ after annealing series

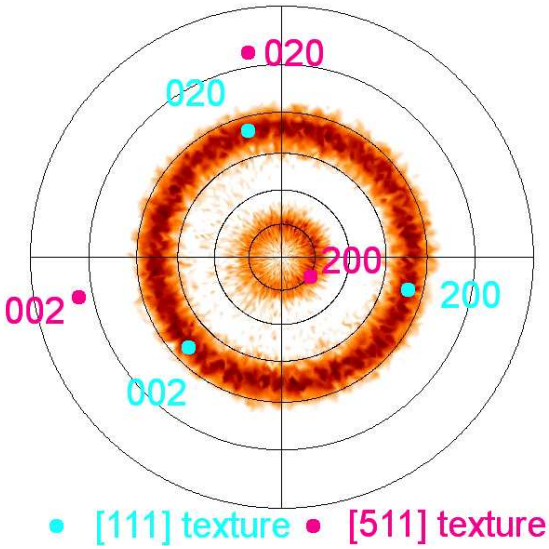

b.) K15(200)$_{Au}$ as prepared 2Θ=68,4

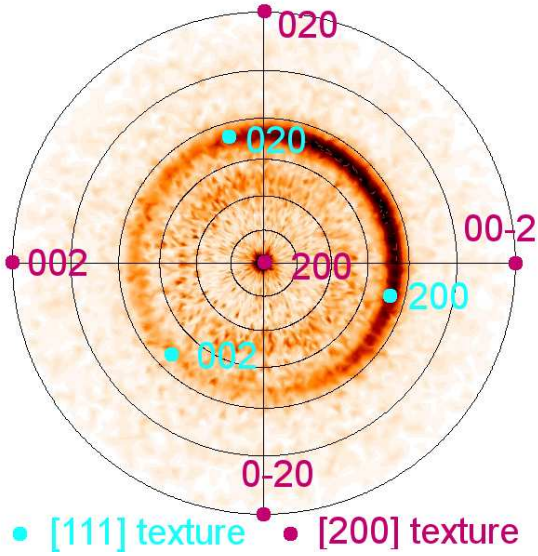

e.) K15(200)$_{Au}$ after annealing series

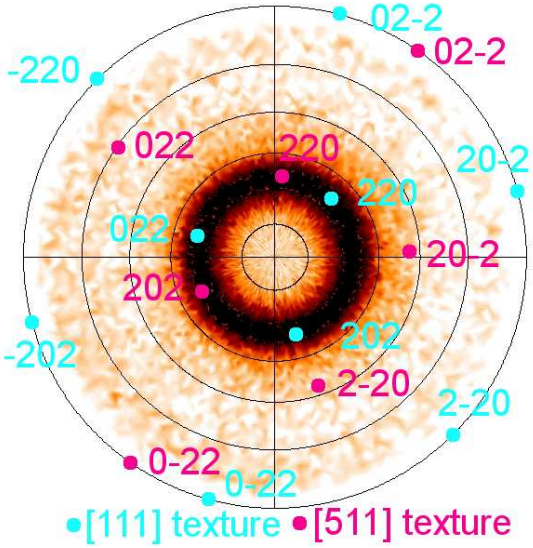

c.) K15(220)$_{Au}$ as prepared 2Θ=105,4

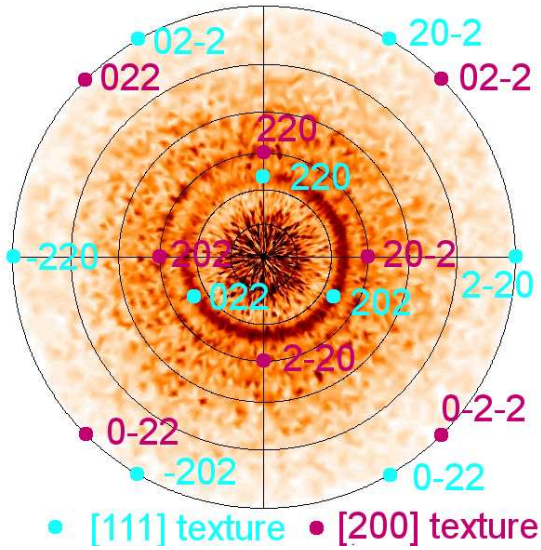

f.)K15(220)$_{Au}$ after annealing series

Figure 6.1: **a.) + d.)**111], **b.) + e.)**[200], and **c.) + f.)**[220]. polefigures of the 100nm gold samples K15 as prepared (left) and after the annealing series with DHS900 annealed at 900℃(right). Measured with Cr-K_alpha radiation.

Until 500℃ thermal annealing the {511} texture got smaller and {111} texture stronger. After 700℃ thermal annealing step additi onally a small {220} texture was found. After thermal annealing step with 900℃. {11 1}-gold texture was stronger again, {511}- and {220}- gold texture did not really exist anymore, further more a strong {200}- gold texture was found. This texture development can be followed by the measured ψ-maps shown in figure 6.7 until 6.11.
In figure 6.2 all found different macroscopic morphologies measured with optical microscopy are displayed. So in figure 6.2a.) gold hills with an size until 50µm are observable. They got smaller after thermal annealing step with higher temperature, viewable in figure 6.2g.). It was a very interesting observation that gold layer crack with resulted gold hill morphology was clearly delimited by another gold layer crack morphology (see figure 6.2f.)). The observed starting point of the gold hill morphology was the pyramidical morphology in figure6.2c.), which is the most interesting found macroscopic morphology, because the unidentified hkl peaks of the specular scans in figure 6.3 are in connection with this morphology (see next chapter). In international crystal data base no crystallites with this hkl-peaks were able to find in connection with gold, silicon, or both together!

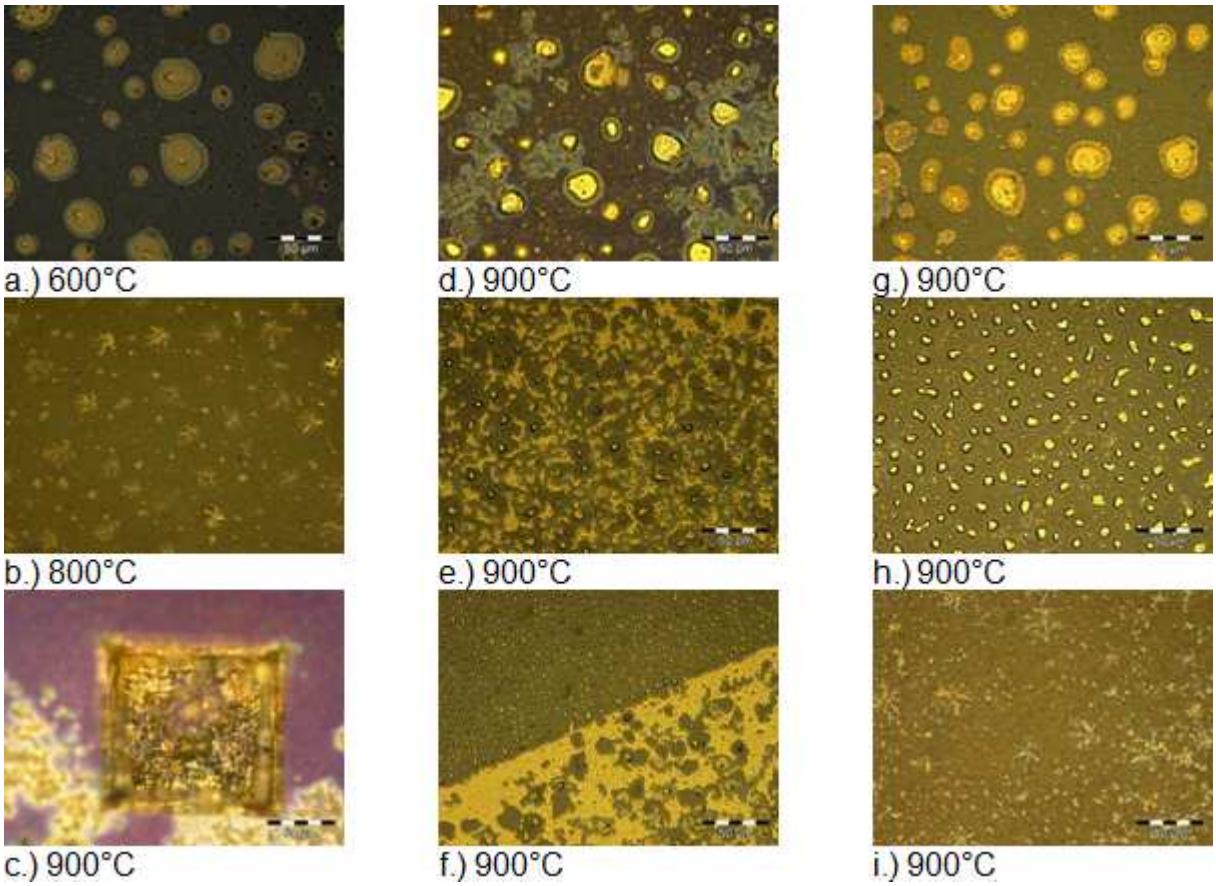

Figure6.2: optical microscopy images of 100nm gold sample K15 after thermal annealing with **a.)**600℃, **b.)**800℃, and **c.) - i.)**900℃

Moreover in figure 6.3 it is clearly observable that these unidentified hkl peaks got smaller after every further thermal annealing step with higher temperature, viewable in figure 6.5c.). So the specular scan difference between the as prepared and the 400℃ thermal annealed measurement is the relative intensity ratio of the three significant gold peaks 111, 200, and 220. Because of stronger {111} texture the ratios

of 111 gold peak intensity to the others is observed higher and higher after thermal annealing with higher temperature until 500℃ step. After macroscopic morphology changing process this relative intensity relationship trend were not observable anymore as well as any other trend in relationship of this intensity ratios. This conclusion was suggested because of the varying textures after 500℃ and higher temperature annealing steps.

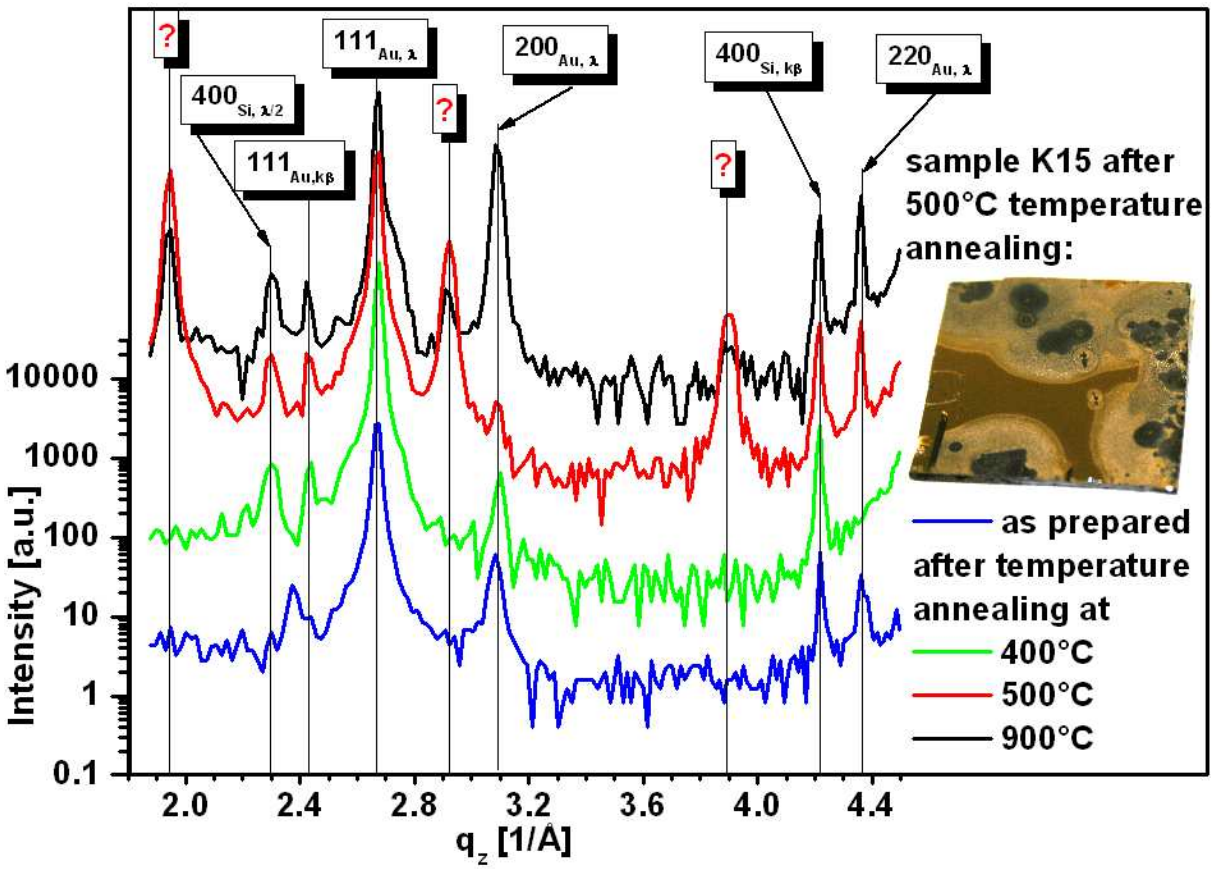

Figure 6.3: representing specular scans of sample K15 (100nm) after temperature annealing at 400℃, 500℃, 900℃, as prepared. The inset show s the changed thin film morphology after the temperature treatment at 500℃.

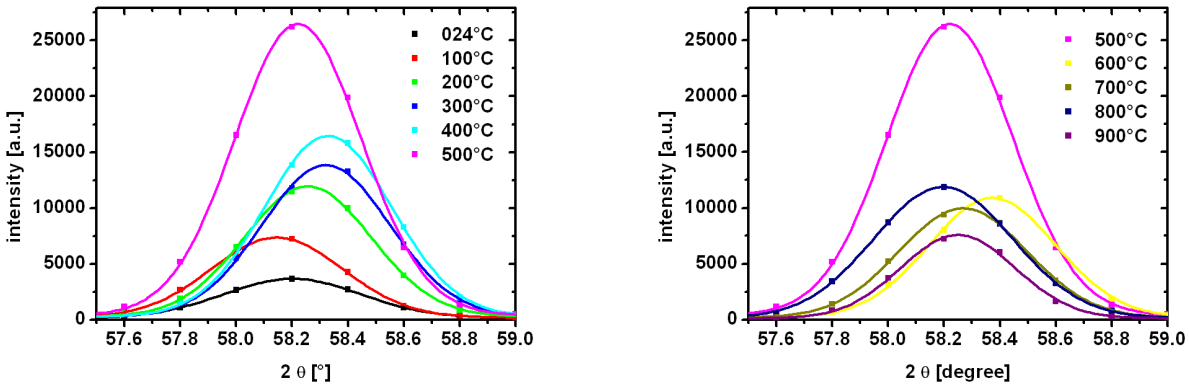

Figure 6.4: experimental data (full points) and the correspondending fitting of the specular 111 peak of sample K15 after temperature annealing up to 900℃ in 100℃ steps.

So in figure 6.4 and 6.5a.) the trend of higher intensity of 111 gold peak is viewable as well as in contrast with all measured ψ-maps the following conclusions about 111 gold peak intensity.
After 600℃ and 700℃ thermal annealing process int ensity go smaller because of added {220} texture. After next annealing step no, except for {111}, texture was found. Following the 111 intensity got higher. And in the end additional the strong {200} texture was found. Therefore the small 111 gold peak intensity is suggested. Additionally the displacement trend of 111 gold peak to higher degree values until 500℃ thermal annealing step is viewable in figure 6.4. In connection with Bragg equation (3.8) smaller lattice constant were calculated (see figure 6.5d.)). The lattice constant value after 500 degree Celsius thermal annealing, which was calculated of the measurement made with X-ray diffractometer from Phillips, do not go with the trend because of an alignment error. So by calculated lattice constant values, displayed in figure 6.5d.), a trend to higher macro stress until gold layer crack was able to be concluded. This trend was reversed after getting inhomogeneous gold layer.

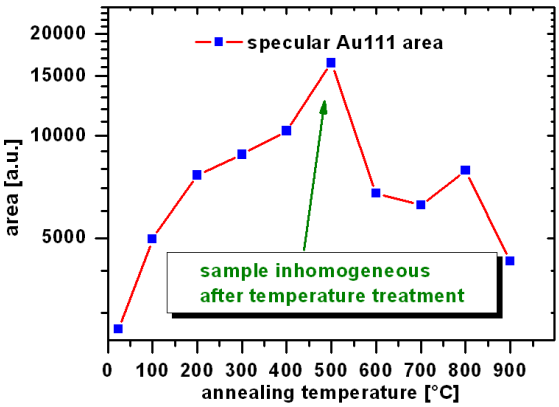

a.) area under 111 gold peak

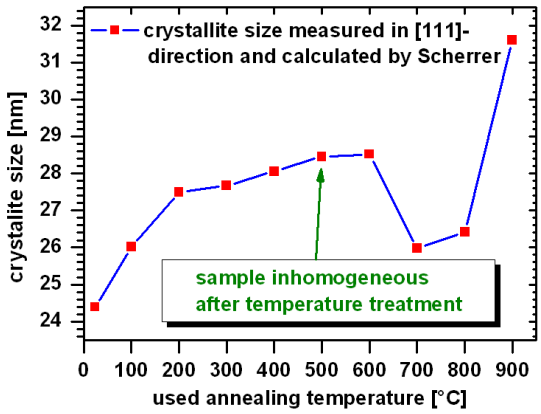

b.) crystallite size

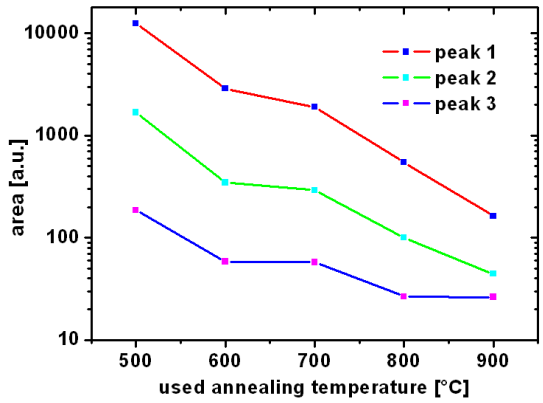

c.) area under unidentified peaks

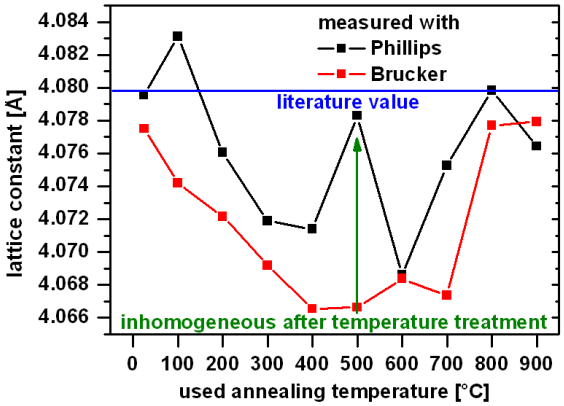

d.) lattice constant

Figure 6.5: calculated temperature-development of different parameters after ex-situ temperature annealing in 100℃ steps up to 900℃ me asured at room temperature

In figure 6.5b.) the crystallite size in (111) direction is calculated with Scherrer equation based on the measurements made with Phillips X-ray diffractometer. The viewable trend to higher crystallite size after thermal annealing with higher temperature got a break after 700℃ thermal anneali ng when a small {220} texture was found. Additional rocking curves of the 111 gold peak were measured with Brucker Discover D8 and Cu radiation by G.H.Flesch. All measured intensities are

displayed in figure 6.6a.), the corresponding full width half maximum FWHM of them in figure 6.6b.). Clearly to see is the trend to better alignment with higher thermal annealing temperature because of smaller full width half maximum of the measured rocking curve peaks in figure 6.6a.).

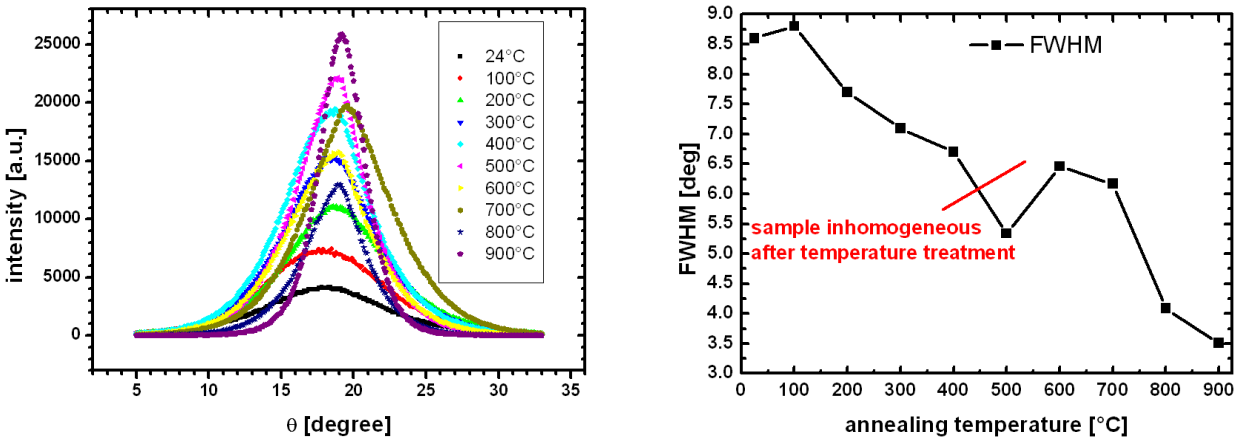

a.) measured rocking curves

b.)calculated full width half maximum development

Figure 6.6:development of rocking curves measured with Brucker discover D8 (Cu-radiation) after temperature annealing in 100℃ steps up to 900℃: **a.)** measured data points **b.)** calculated FWHM (full width half maximum) of rocking curves

On the next pages ψ-maps of sample k15 are displayed. The maps after 100℃, 200℃, and 300℃ thermal annealing temperature are not displayed because there were no significant differences found compared to four hundred degree map. The texture development are represented by the displayed maps.

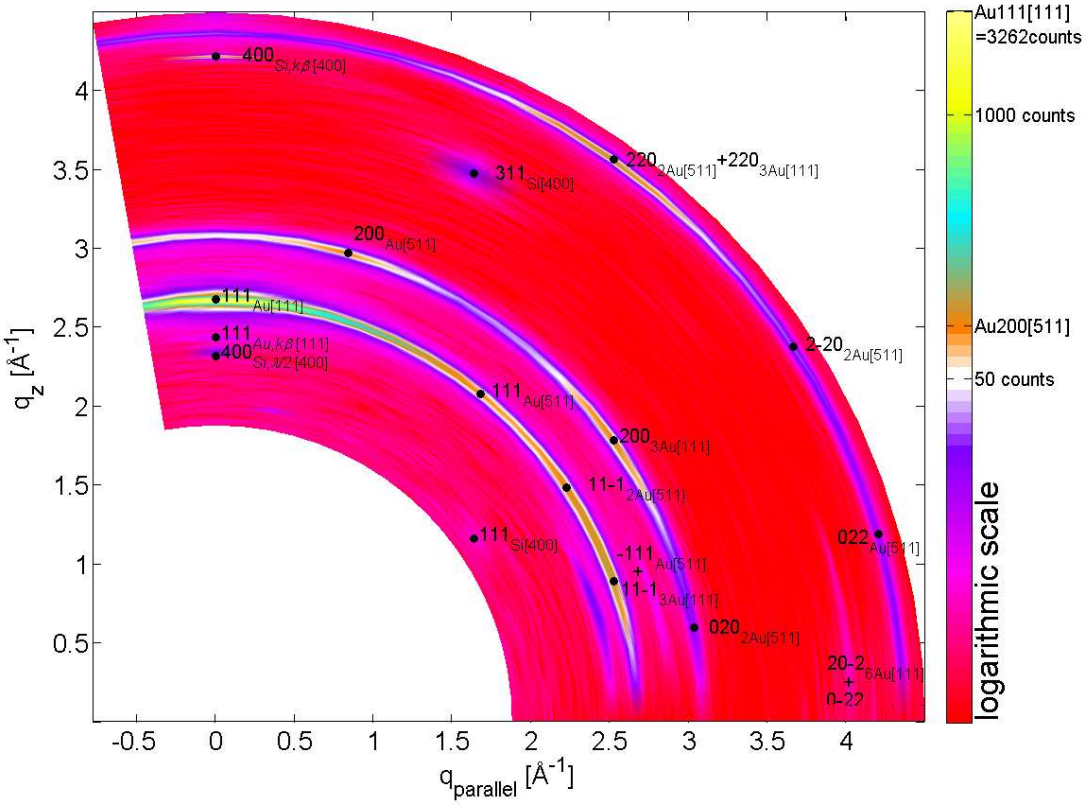

Figure 6.7: reciprocal space map of sample K15 as prepared. {111} - and {5111} - gold texture was detected

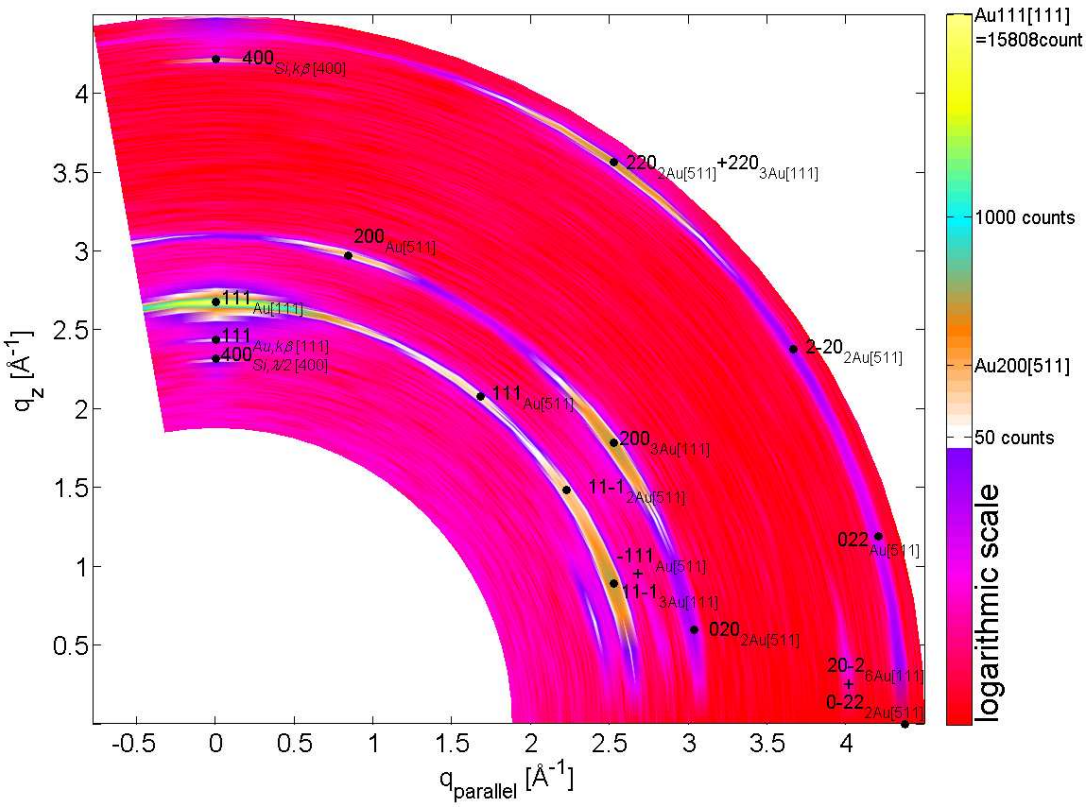

Figure 6.8: reciprocal space map of sample K15 after temperature annealing step with 400℃. {111} - gold texture was stronger and {511} - gold texture was smaller

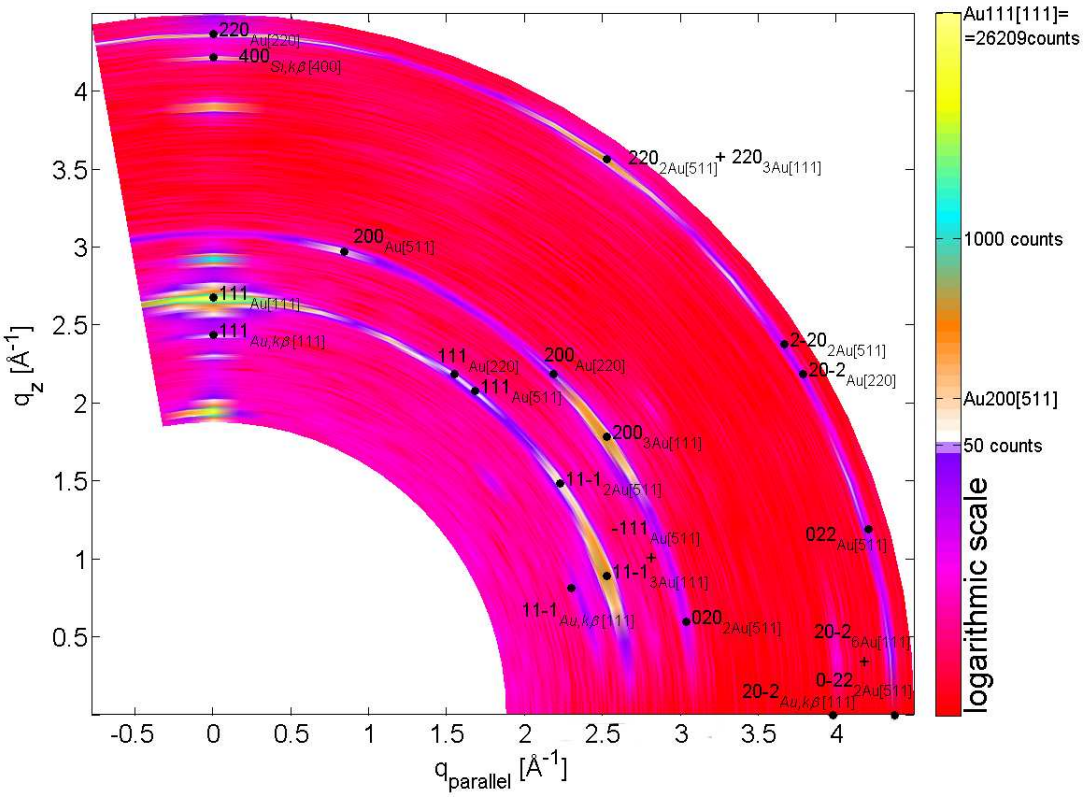

Figure 6.9: reciprocal space map of sample K15 after temperature annealing step with 500℃. {111} - gold texture was stronger, {511} - g old texture was smaller. Further more three unidentified peaks was found.

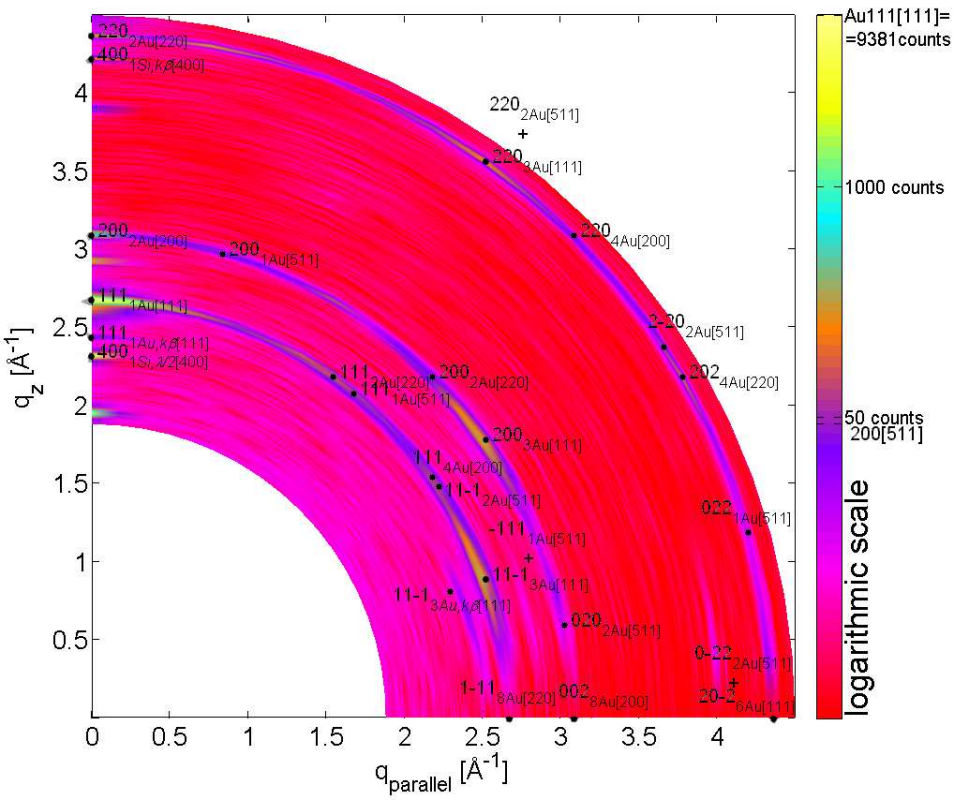

Figure 6.10: reciprocal space map of sample K15 after temperature annealing step with 700℃. {111} - gold texture got smaller and a small {220} - gold texture was found. Further more the three unidentified peaks got smaller.

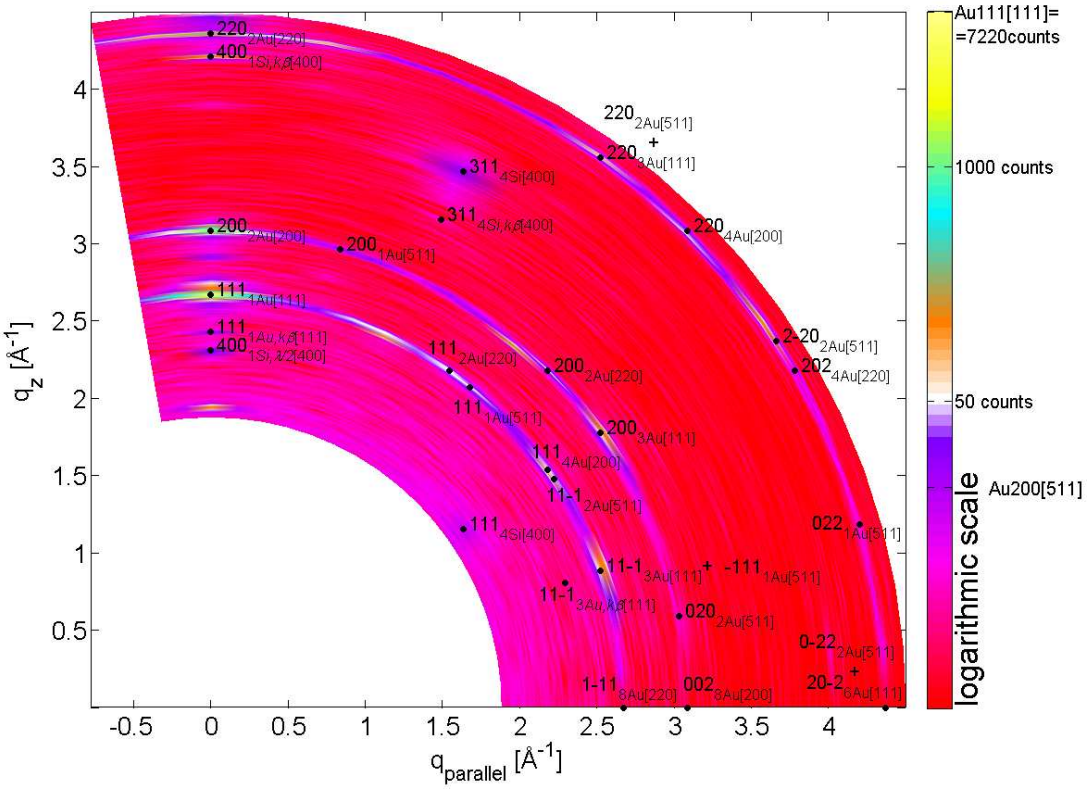

Figure 6.11: reciprocal space map of sample K15 after temperature annealing step with 900℃. {111} -gold texture was stronger, {511} - an d {220} - gold texture did not really exist anymore. Further more a strong {200} - gold texture was found.

As noted after every thermal annealing step of gold sample K15 AFM (atomic force microscopy) images were measured by H.G.Flesch comparing morphology, structure, and grain size. All measured AFM data were processed with “Gwyddion”, which is a modular program for SPM (scanning probe microscopy) data visualization and analysis. In the upper front side of figure 6.12a.) the surface at homogeneous area of 100nm gold sample K15 is visualised after five hundred degree Celsius thermal annealing step. Under it corresponding highness profile was chosen in a way that the largest highness differences of the whole image are visualized, just as well in figure 6.12b.), which is a spot in inhomogeneous area of sample K15. While gold hill highness in inhomogeneous area can be multiplied less with a factor of ten, the average gold hill distance at most can be multiplied with factor two. A very important conclusion was made by the fact that in inhomogeneous area the gold hill highness is higher than 300nm. Later in the SEM (scanning microscopy) investigation chapter EDX (energy dispersive X-ray) spectrums will be discussed. So in this chapter discussed conclusions are depended on the electron depth of impression into the bulk as well as on the highness of the investigated gold hills (see chapter 6.3.2).
Afterwards AFM images, measured after every thermal annealing step, and therefore development of grain size and highness profile in homogeneous area of gold sample K15 is displayed in figure 6.13a.)-h.). In the beginning small homogeneous grains with an average thickness of 50nm were detected. Until 500℃ step the average surface got smoother but of some increasing single grains. After 500℃ thermal annealing step the grain size difference between every step were detected increasing more and more. In the end grain size in range of one micrometer was detected (see figure 6.13h.)).

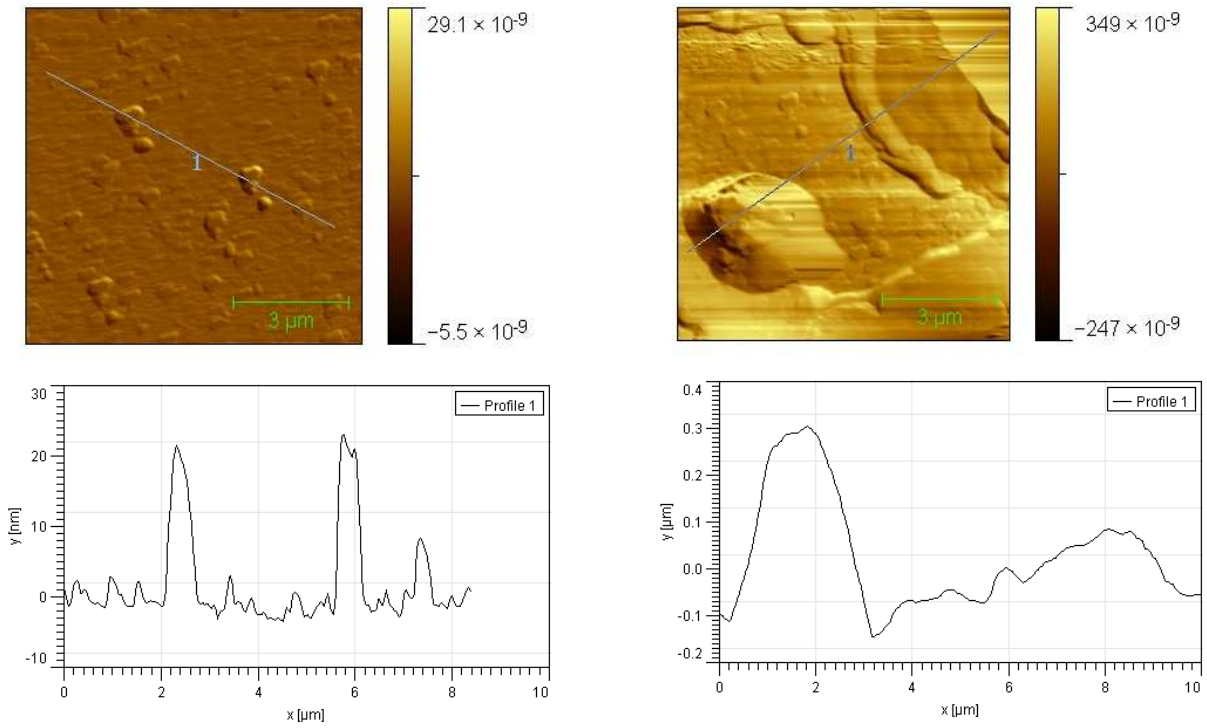

a.) homogeneous area b.) inhomogeneous area

Figure 6.12: AFM (atomic force microscopy) spot of 100nm gold sample K15 after 500℃ temperature annealing on **a.)** homogenous (left) **b.)** inhomogeneous (right) places and the corresponding highness profiles

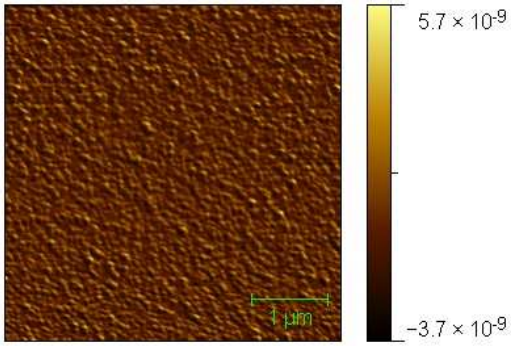

a.) 100℃

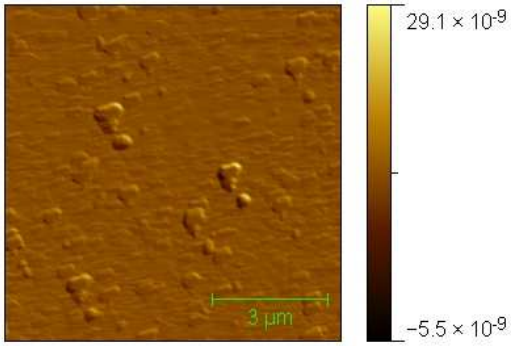

e.) 500℃

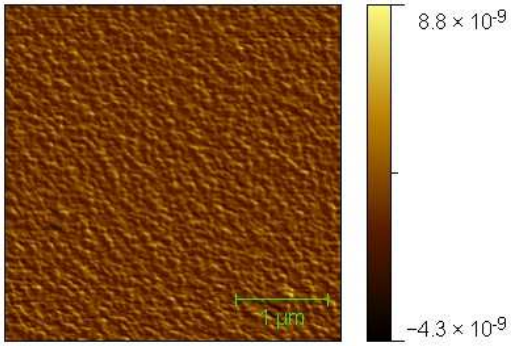

b.) 200℃

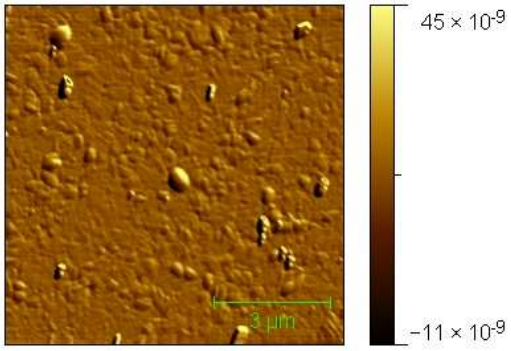

f.) 600℃

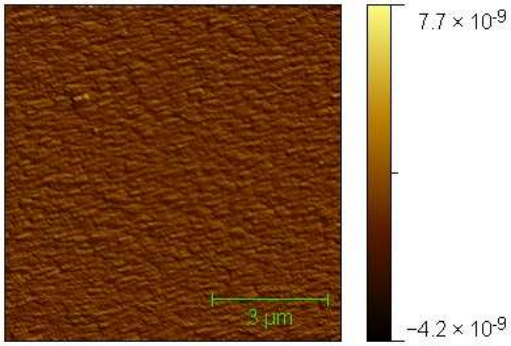

c.) 300℃

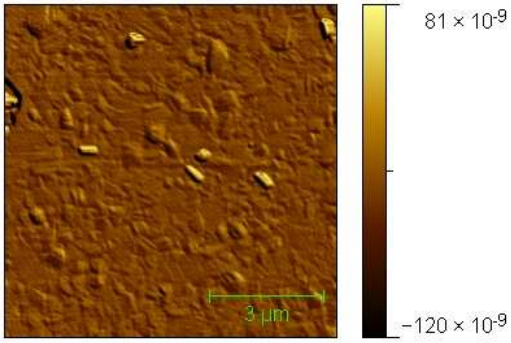

g.) 700℃

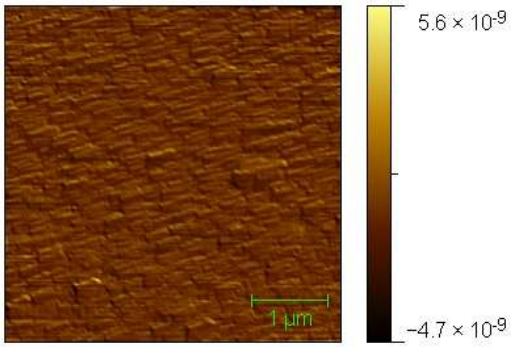

d.) 400℃

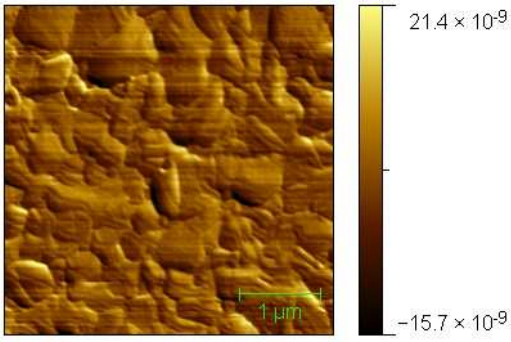

h.) 800℃

Figure 6.13: AFM (atomic force microscopy) measurements of homogeneous areas on sample K15 (100nm) after every annealing step up to 800℃ .

Because of the macroscopic changed area after 500℃ thermal annealing step further investigations with NOVA 200 Dual microscopy at single gold hills, see figure 6.14a.), were measured by H.Planck. The used system is a dual beam microscopy, which consists of a FIB (focused ion beam) and FEB (focused electron beam). The highly energetic Ga ions were used removing material (sputtering) at spot of incidence. A three dimensional structuring down to the nanometer scale was possible because of controlled movement and exposure time of the ion beam. Additional simultaneous operation of FIB and FEB allowed online monitoring of structuring. Different crystal orientation was registered after selective sputtering, see figure 6.14b.). If there polycrystalline structuring or a second phase existing was not possible to difference. On the half gold hill in figure 6.14d.) redeposition of sputtering is viewable, moreover the optionally found second phase, darker areas in figure 6.14d.), looks more like voids.

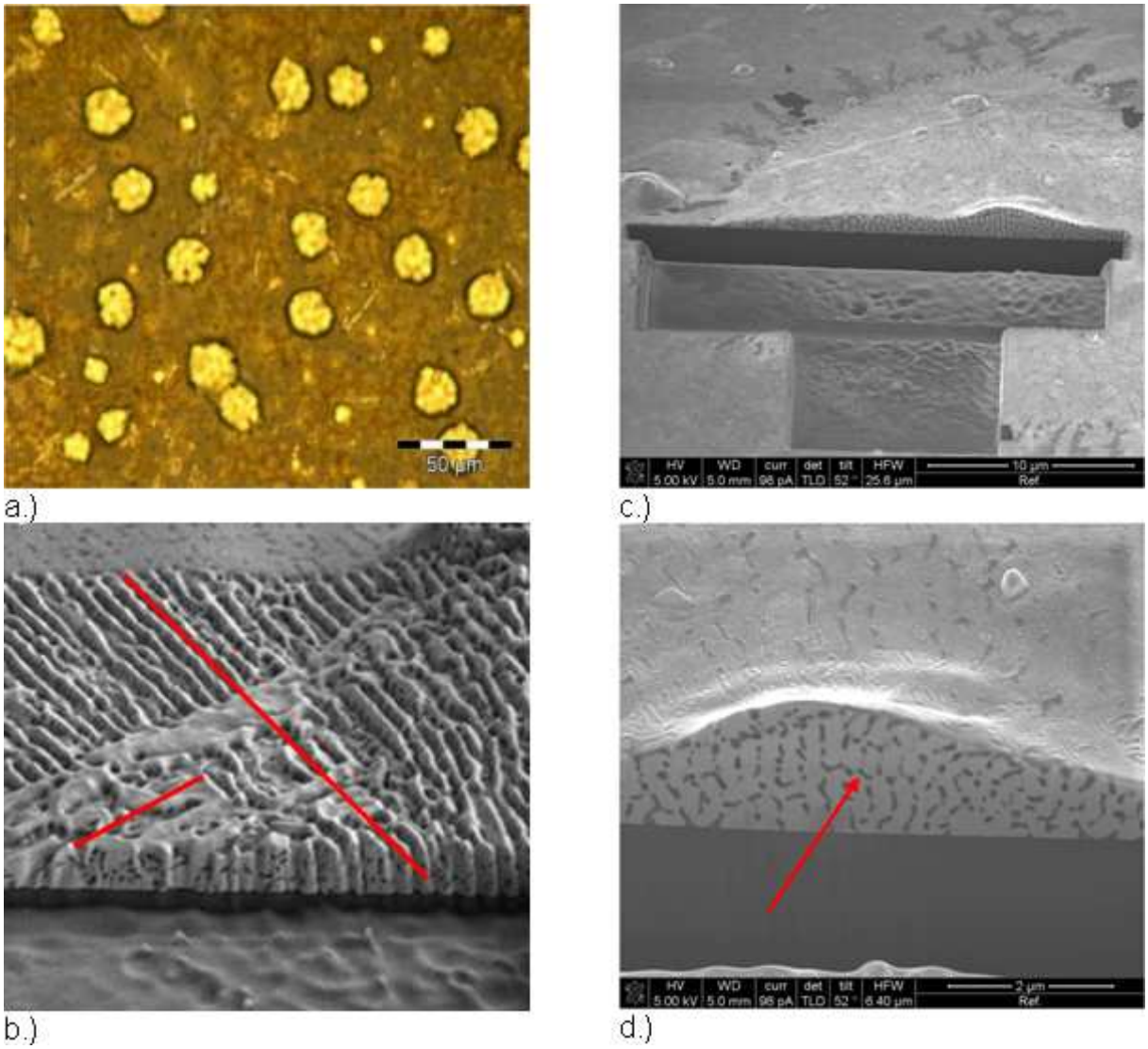

Figure 6.:14 sample K15 (100nm gold) images after 900℃ thermal annealing : **a.)** optical microscopy image **c.) - d.)** SEM (scanning electron microscopy) images after focused ion beam etching

6.1.2. sample K12

Verifying the results in connection with macroscopic morphology changing, especially the unidentified specular scan X-ray diffraction peaks in figure 6.3, a second 100nm gold sample was thermal annealed. This 100nm gold sample, named K12, was produced under same conditions as sample K15 discussed in last chapter. So it was not really surprisingly registering the same textures, strong {111} and small {511}, see figure 6.16. At first sample K12 was thermal annealed with DHS900 at temperature of four hundred degree Celsius during a twelve hours period. Afterwards no morphology changes with optical microscopy as well as other X-ray diffraction peaks out of well known gold and silicon peaks were found. Then a thermal annealing temperature of five hundred degree Celsius was used, at first during a thermal annealing period of twelve hours. Only one edge of the sample surface was macroscopic changed (see figure 6.17). In this area also one pyramidical morphology, like n figure 6.15c.)+d.) displayed, was identified. And after X-ray diffraction and optical microscopy investigating, a second period over sixty seven hours were thermal annealed with temperature of five hundred degree Celsius. . In figure 6.15a.)+b.) optical microscopy images are displayed of till unknown morphologies like hill with needles and gold layer crack within closed gold layer with small gold hills. Moreover in figure 6.15c.)+d.) pyramidical morphology and the surrounding area are displayed.

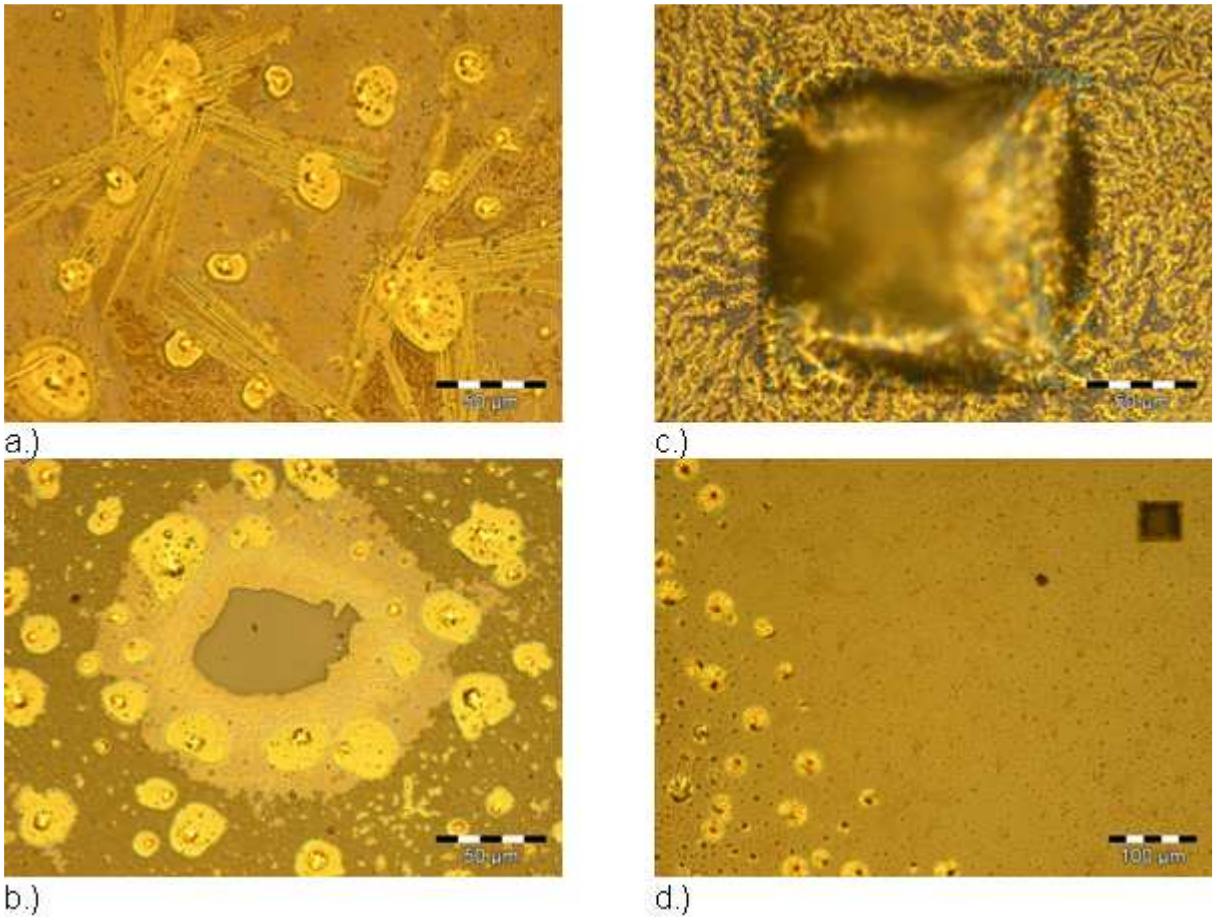

Figure6.15: optical microscopy images of different sample K12 morphologies after 500℃ thermal annealing **a.)** gold needles **b.)** gold layer crack **c.)** pyramidical crack into substrate **d.)** surrounding area around pyramidical crack

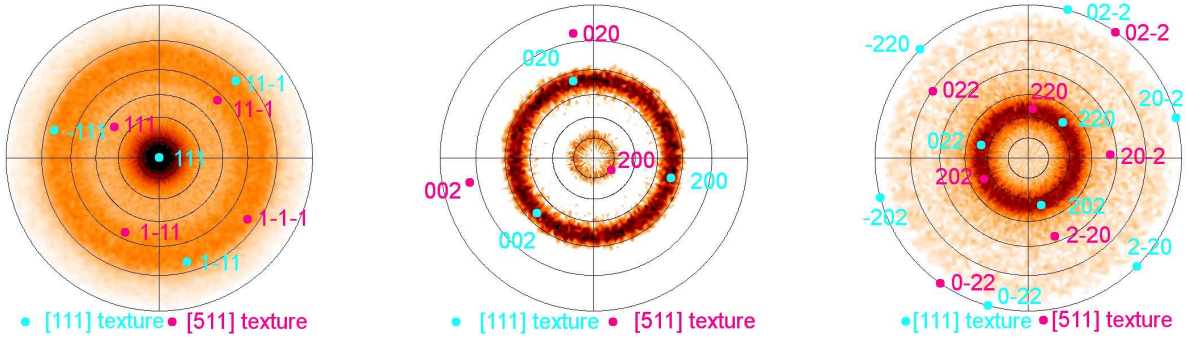

a.) K12(111)$_{Au}$ 2Θ=58,3 b.) K12(200)$_{Au}$ 2Θ=68,4 c.) K12(220)$_{Au}$ 2Θ=105,4

Figure 6.16: polefigures of sample K12 (100nm) as prepared.

As noted after every thermal annealing step X-ray diffraction investigations were made. So ψ-map were measured with Phillips X-ray diffractometer after every step at room temperature, whereas an integration time of 2,45s per step was used. Moreover always the same electrical X-ray tube voltage was set up. The used ψ-range was chosen from minus ten to plus ninety tilting degree with a step size of five degree. The 2θ range was measured from 40 to 110 degree. After 400℃ thermal annealing step no really changes in comparison with as prepared measurement results were found. In the following thermal annealing step with 500℃ during a annealing time of twelve hours the most interesting conclusion described in this chapter was found. So at first the X-ray beam was focused in the middle of the thermal annealed sample, where no macroscopic changes and a homogenous gold surface area were found. Because of no existing unidentified X-ray diffraction peaks, see figure 6.17, like on sample K15 after 500℃ the rmal annealing a second ψ-map was measured whereas the X-ray beam was focused on the inhomogeneous area. In this area as said one pyramidical morphology was found. And like in figure 6.17 reproducible in this area the so called unidentified X-ray diffraction peaks were measured. So a correlation between the so called unidentified peaks and the pyramidical morphology was accounted. This account was confirmed with measurements described in the next chapter.
Then 500℃ thermal annealing for a thermal annealin g time of 67 hours was investigated. At first it must be noted, that after this thermal annealing step several pyramidical morphologies with optical microscopy were found. Inhomogeneous area was registered all over the whole sample surface. Afterwards a ψ-map with the same calibration parameters as before with Phillips diffractometer was measured. The X-ray beam was focused to the middle of sample. By figure 6.17 it is clearly reproducible that the intensities of the three unknown X-ray diffraction peaks in correlation to 111 gold peak got stronger. This fact and moreover the fact of existing more pyramidical morphologies was interpreted as the second indication that a correlation between the pyramidical morphologies and the three unidentified peaks have to exist.

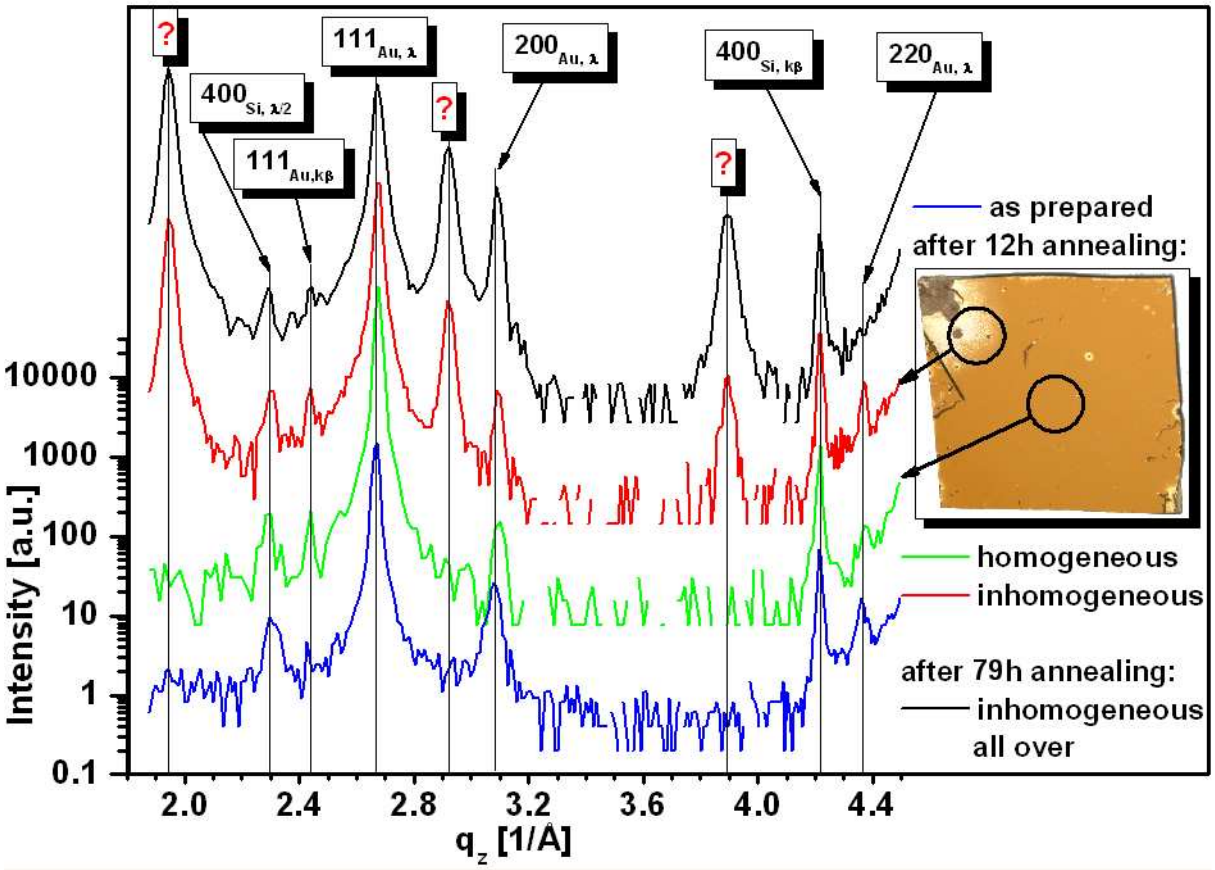

Figure 6.17: specular scans of sample K12 (100nm) as prepared, after 12 hours 500℃ temperature annealing, X-ray beam focused on inhomogeneous and homogeneous areas, and after moreover 67 hours 500℃ thermal annealing .

6.1.3. other samples

Because of small adhesion force of gold layer on the smooth silicon-dioxid surface of the substrate the hypothesis was made that gold layer cracking after five hundred degree Celsius thermal annealing would be avoided by existing stronger adhesion forces of gold layer. Therefore the sample K20 was prepared in Graz with a five nanometer chrome layer between one hundred nanometer gold layer and substrate. The adhesion forces of gold is as known essential stronger.At first a ψ-map of this sample was measured as prepared. The found gold crystallites orientation was interpreted by a strong {111} and a small {511} texture. After twelve hours thermal annealing of sample K20 with DHS900 with 500℃ the gold layer was cracked once again, but with other found morphologies. In figure 6.19 all new morphologies, measured with optical microscopy, are displayed. Moreover no pyramidical morphology was found. At second a third small {200}-texture was found by ψ-mapping. The most interesting result of the ψ-map measurement was the fact that the so called three unidentified X-ray diffraction peaks did not exist. Instead one other non identifiable peak was measured. This peak in the specular scan pattern was not identifiable in correlation with gold, silicon, or chrome. The position of this peak was a little bit shifted rightwards compared to the first so called unidentified peak of sample K15 specular scan pattern. In figure 6.18 all measured specular scan pattern are displayed. The first unidentified peak of samples K12 and K15 was no symmetric peak identified and therefore the use of existing two single peaks because of superposition in comparison with the new unidentified specular scan peak of gold-chrome sample K20 was made.
Checking up the correlation between pyramidical morphology and the so called three unidentified specular scan pattern peaks other 100nm gold samples, which were produced in Graz, were thermal annealed with a temperature of 500℃ during an annealing time of twelve hours. Of all sample ψ- map investigations with Phillips diffractometer were measured as prepared and after thermal annealing process. All samples were strong {111} and small {511} textured as prepared. Moreover after thermal annealing process at all samples the pyramidical morphology were registered instead of one gold sample named K18. The fact that all specular scan pattern, measured after thermal annealing process, the so called three unidentified peaks feature, instead of sample K18 without pyramidical morphology, was the third indication and finally the proof of existing correlation between pyramidical morphologies and the so called unidentified specular pattern peaks. By figure 6.18 this fact is reproducible, moreover the interesting measurement result, that at sample K18 without existing pyramidical morphology after thermal annealing process the a further unidentifiable X-ray diffraction peak was measured at the same position like the unidentified peak measured at gold-chrome-sample K20. Comparing the results, measured with FIB (focused ion beam), there also FIB investigations with gold-chrome sample were measured by Harald Planck. In figure 6.20 these measurements are displayed. The hill structure in figure 6.20 b.) and c.) looks like a double phase structure. But after ionizing the hill and sputtering, displayed in figure 6.20d.), the darker areas of the hill look more like voids. Differencing this phenomena no more investigations were done

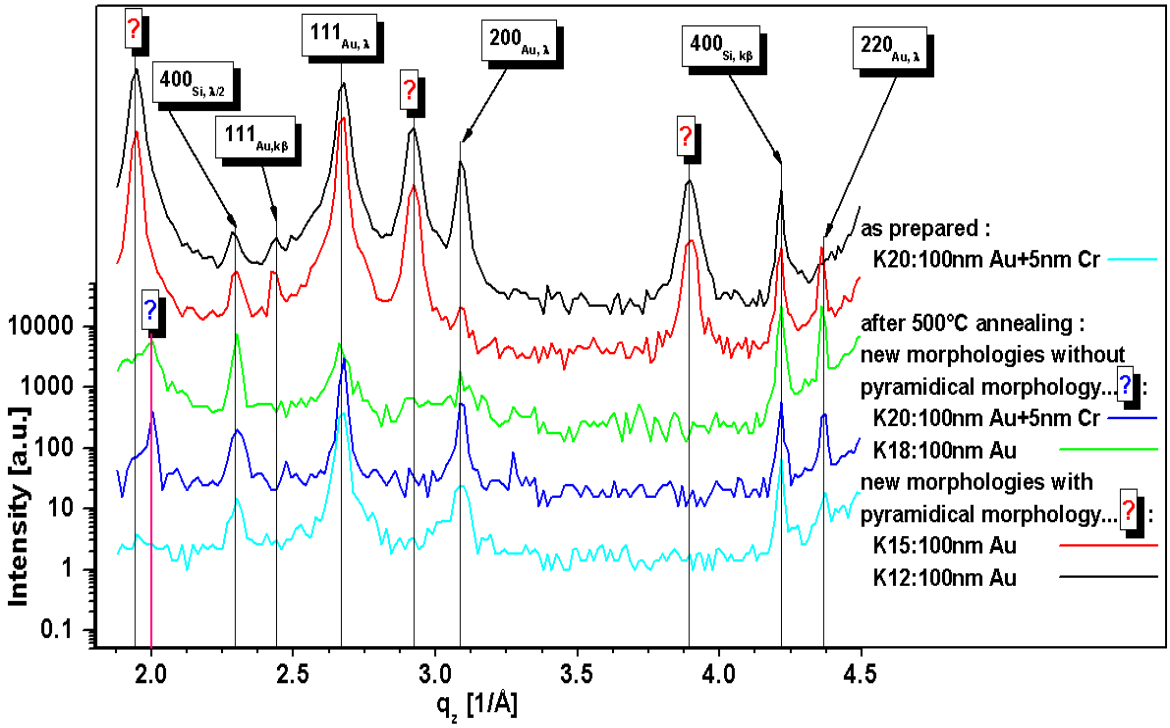

Figure 6.18: specular scan pattern of 100nm gold films without as well as with Cr 5nm layer between gold and substrate

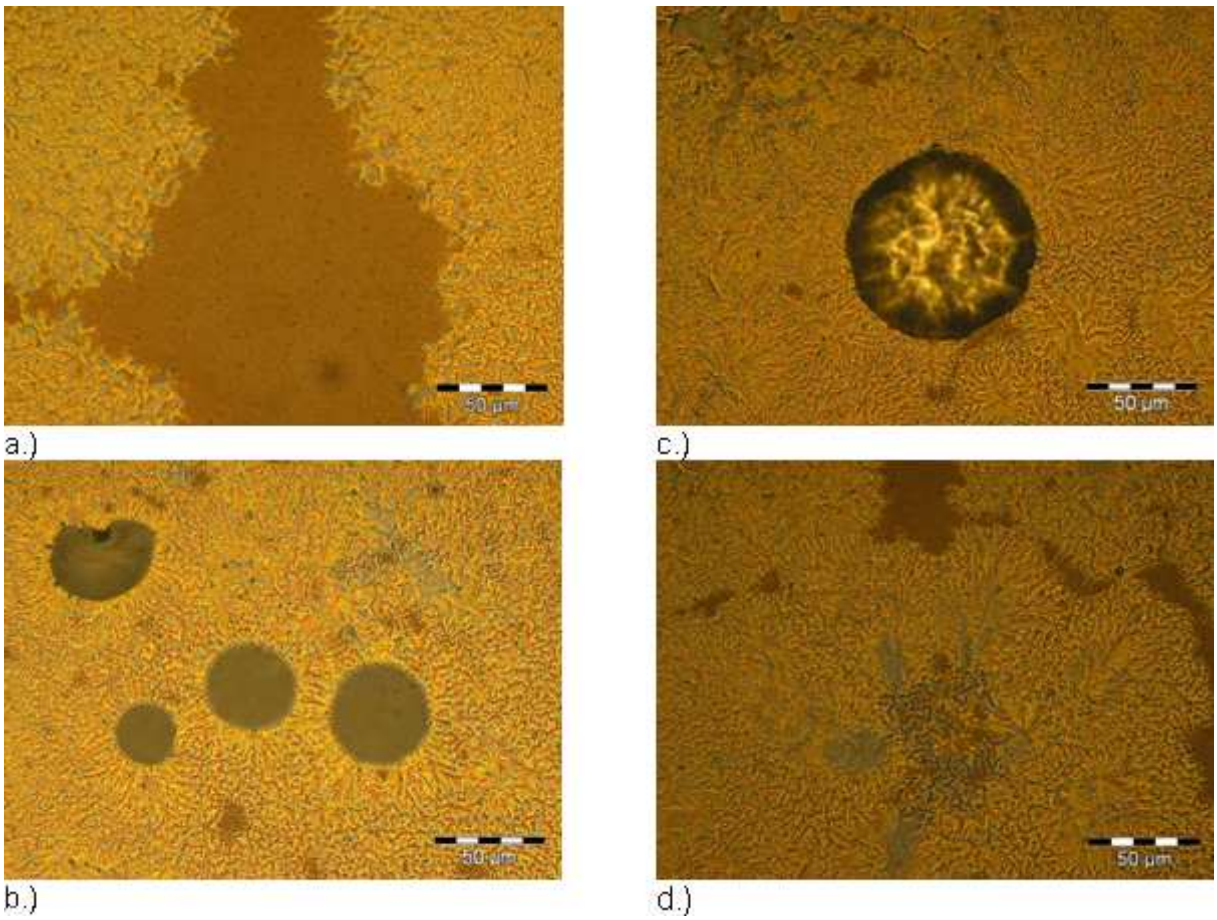

Figure 6.19: optical microscopy images of sample K20(100nm Au+5nm Cr) after 500℃ thermal annealing **a.)** gold layer crack **b.)** circular gold and chrome crack **c.)** cylindric gold morphology d.) overview

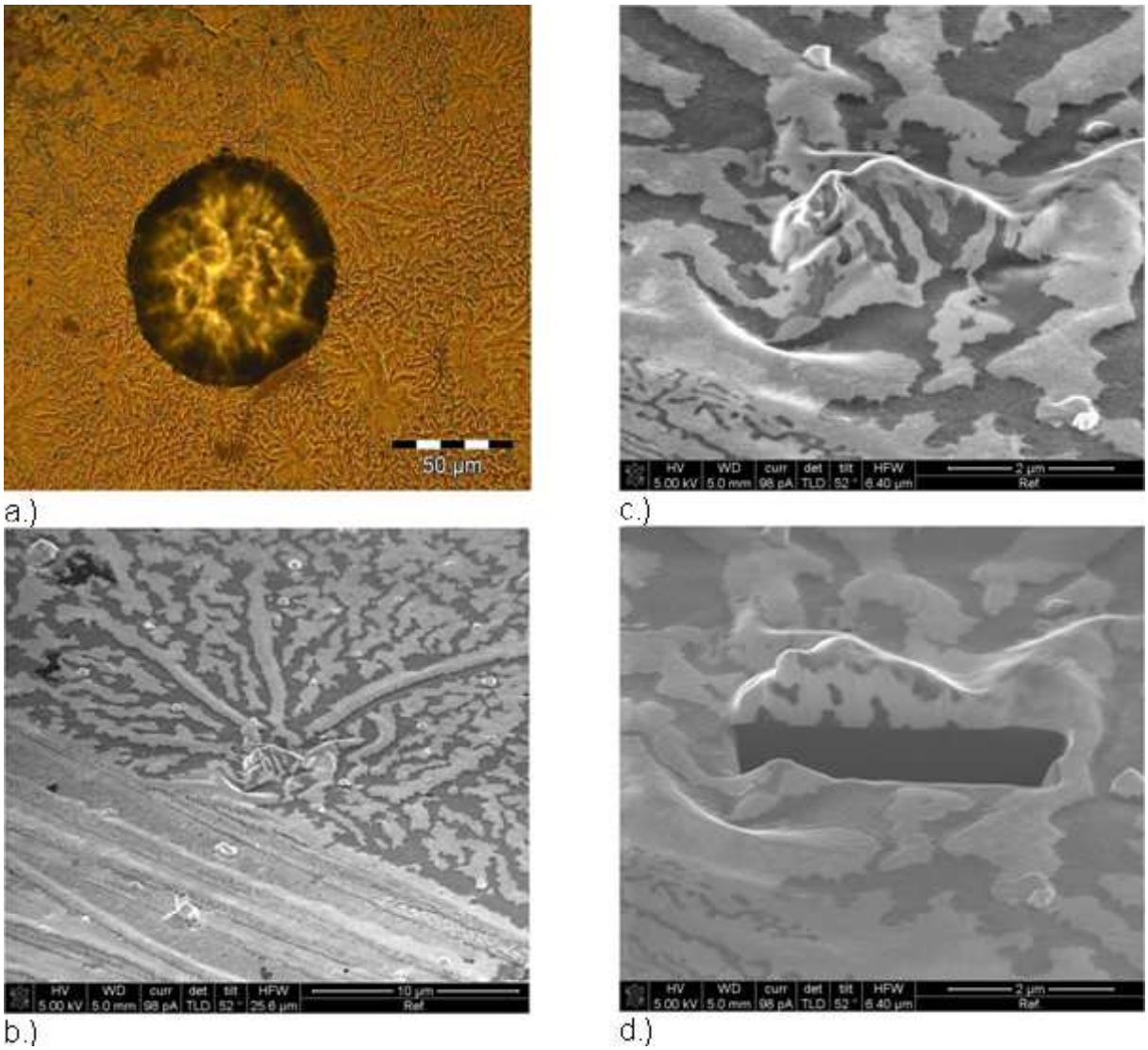

Figure 6.20: sample K20 (100nm gold+5nm chrome) images after 500℃ thermal annealing : **a.)** optical microscopy image **b.)-c.)** SEM (scanning electron microscopy) images **d.)** after focused ion beam etching

Moreover the used substrate was thermal annealed with 500℃ during an annealing time of twelve hours. Afterwards no macroscopic changing was found with optical microscopy. In figure 6.21 XRR (X-ray reflectivity) investigations of the thermal oxidized silicon substrate are displayed. These investigations were made by H.G. Flesch with Brucker Discover D8. So after thermal annealing process no oxide layer thickness difference was discovered, but a slightly different roughness. Small changes in roughness might be related to measurement errors of non equally shaped samples.

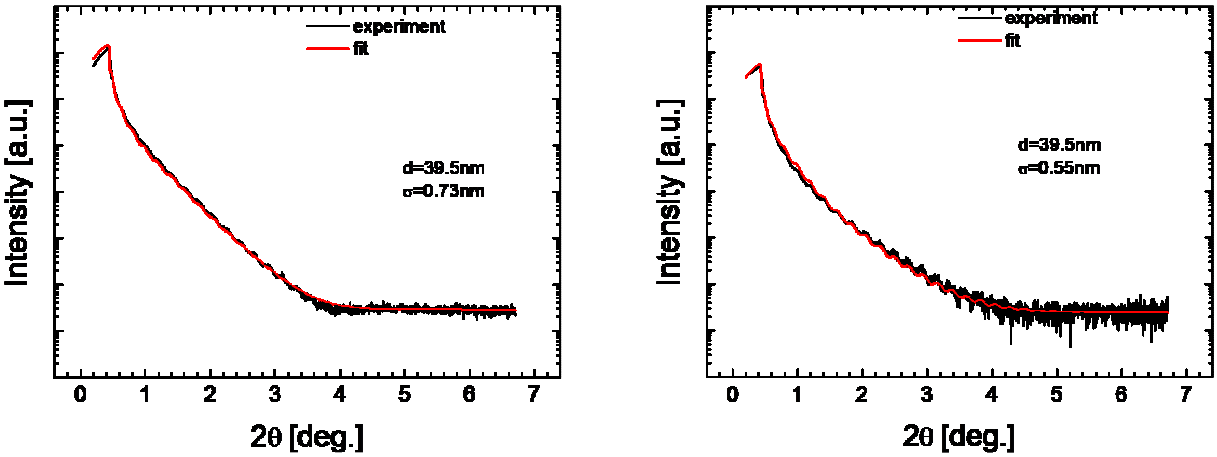

a.) as prepared b.) after 500℃ thermal annealing

Figure 6.21 : XRR (X-ray reflectivity) measurements of thermal oxidized silicon substrate

In summery the following corresponding ex-situ measurements results were discovered in this chapter :

- Gold layer cracking at a temperature between 400℃ and 500℃
- Existing of three unidentifiable X-ray diffraction peaks after gold layer cracking in correlation with a new pyramidical morphology
- Using higher thermal annealing temperature leads to better crystallite alignment measurement results
- Micro stress increasing until 500℃ thermal anneal ing step and afterwards decreasing after every thermal annealing step
- Increasing grain size with higher thermal annealing temperature
- increasing hill highness until the triple origin gold layer thickness
- stronger {111} texture after every thermal annealing step
- new gold texture after 700℃ (small {220}) and 900 ℃ (strong {200})
- no discovered differences of only substrate after thermal annealing with 500℃

6.2. In-situ investigations with DHS 1100

X-ray diffraction in-situ investigations were measured by O.Werzer and H.G.Flesch with diffratometer Brucker Discover D8. So DHS1100 was built into Brucker Discover D8. The 20nm gold sample K13, made in Bratislava, was used for this measurement series. After sample alignment the four gold peaks 11-1$_{\{111\}}$, 111$_{\{111\}}$, 222$_{\{111\}}$, and 22-2$_{\{111\}}$ of the sample as prepared were measured by 2θ/θ-technique. 222$_{\{111\}}$ notice the 222 diffraction peak of the crystallites, which are oriented with a {111} texture. Under an atmosphere of the inert gas Argon the sample was thermal annealed at 100℃ during an annealing time of one hour. During this time the development of 111 gold diffraction peak was observed by specular scan measuring with small integration time and greater 2θ steps. Afterwards with higher integration time and smaller 2θ steps specular scans of the same four gold diffraction peaks as above were measured. Then the thermal annealing temperature was increased to 200℃ following the same X-ray measurement procedure as above. This thermal annealing and X-ray diffraction measurement step was made in one 100℃ steps up to 1100℃.
In the following figure 6.21 – 6.24 all in-situ diffraction measurement points inclusive corresponding fit lines are displayed. The fit was calculated with the computer program Origin 7.0. In figure 6.21 the measuring results of 111$_{\{111\}}$ gold peak are displayed. These measurement results were used calculating all following conclusions in this chapter because of the highest intensity. So lattice expansion is noticed by drifting to smaller angels just as well increasing crystallite size in the corresponding direction by getting more intensity at higher temperature. Only the intensities, measured at 1000℃ and higher temperat ure, got smaller. This fact can be explained by beginning gold evaporating process. In figure 6.22 the higher order diffraction peak of this lattice distance are displayed. Similar characteristics as at the 111$_{\{111\}}$ gold peak except for the visualizing smaller intensity can be noticed. The higher order was measured because of calculating Williamson Hall plot.
Therefore as well the 11-1$_{\{111\}}$ and the corresponding second higher order 22-2$_{\{111\}}$ gold diffraction peaks were measured. They are displayed in figure 6.23 and 6.24. Because the -111$_{\{511\}}$ gold diffraction peak and the corresponding higher order also exist on this reciprocal space place, the measured peaks were identified as superposition of these two peaks, clearly visible in figure 6.23. Therefore and because of the smaller measured intensity of these peaks a significant Williamson Hall calculation was not possible. However lattice constant expansion is observable by peak drifting with higher temperature to smaller 2θ values. So in figure 6.23 it is also observable by drifting apart of the two in superposition existing peaks more and more with higher temperature that the lattice expansion coefficient of the {111} and the {511} textured crystallites are a little bit different. The higher order measured data in figure 5.24 have too less intensity calculating significant fits because of unknown background data. However a similar crystallite size growing development can be registered.

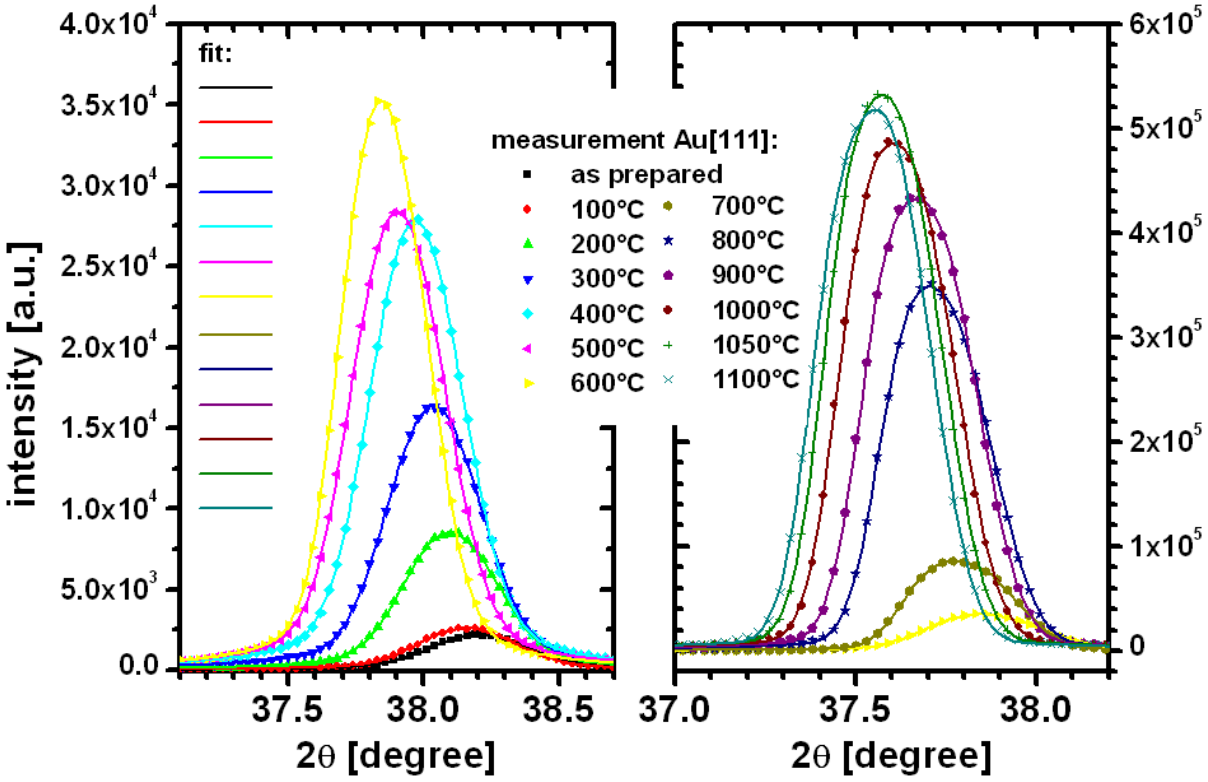

Figure 6.21: in-situ measurement of $111_{\{111\}}$ gold peak and the corresponding fits.

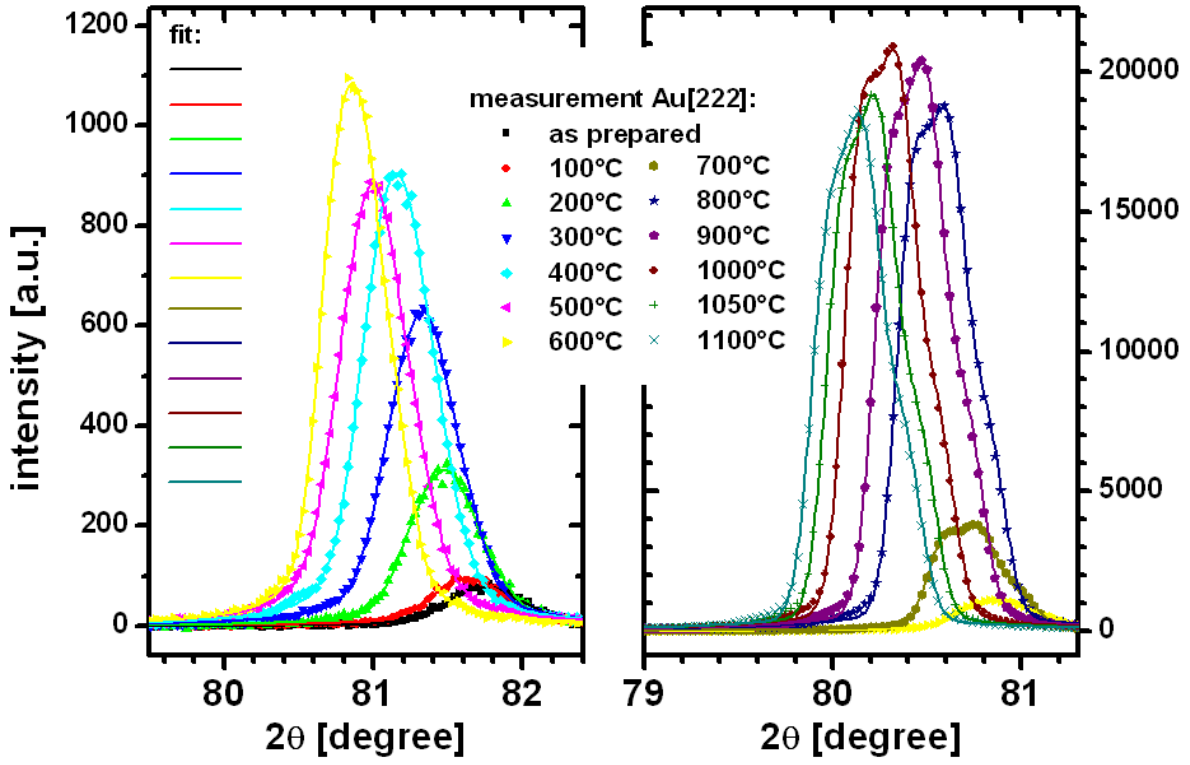

Figure6.22: in-situ measurement of $222_{\{111\}}$ gold peak and the corresponding fits.

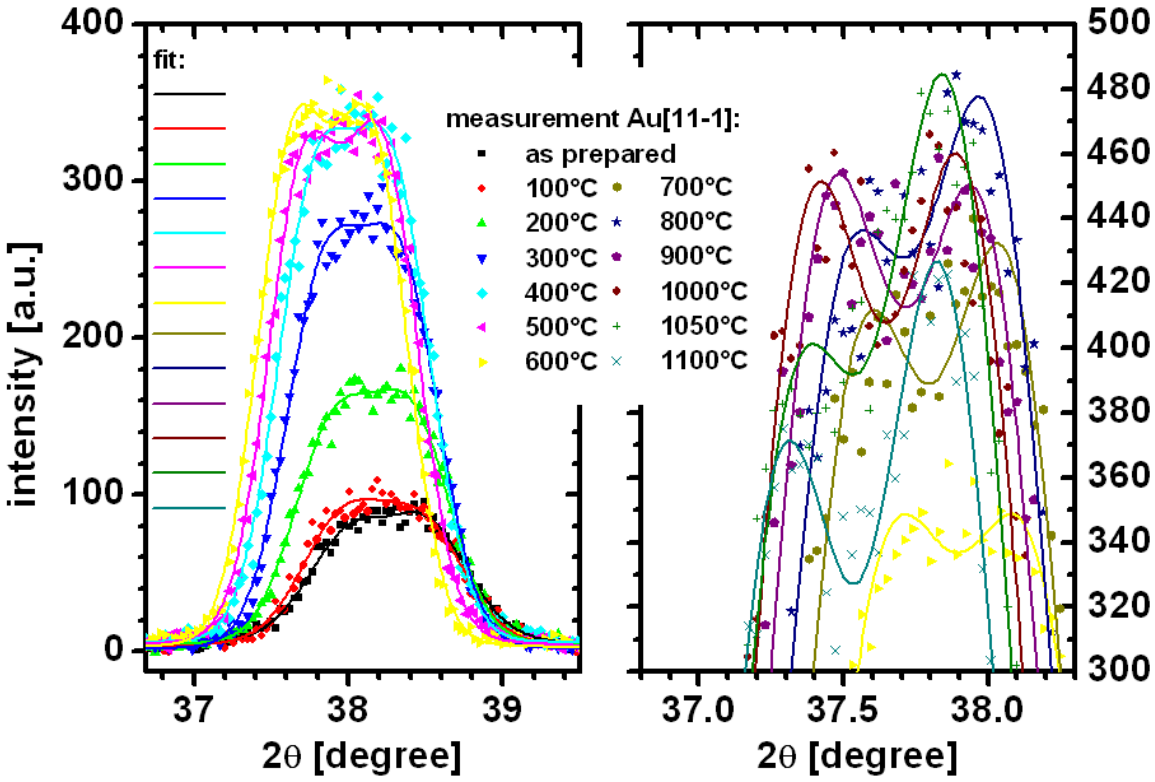

Figure 6.23: in-situ measurement of 11-1$_{\{111\}}$ and -111$_{\{511\}}$ gold peaks as well as their corresponding fits. Different expansion of the two textures is noticed by dispersing of the representing peaks. Increasing crystallites is noticed by getting more intensity with higher temperature.

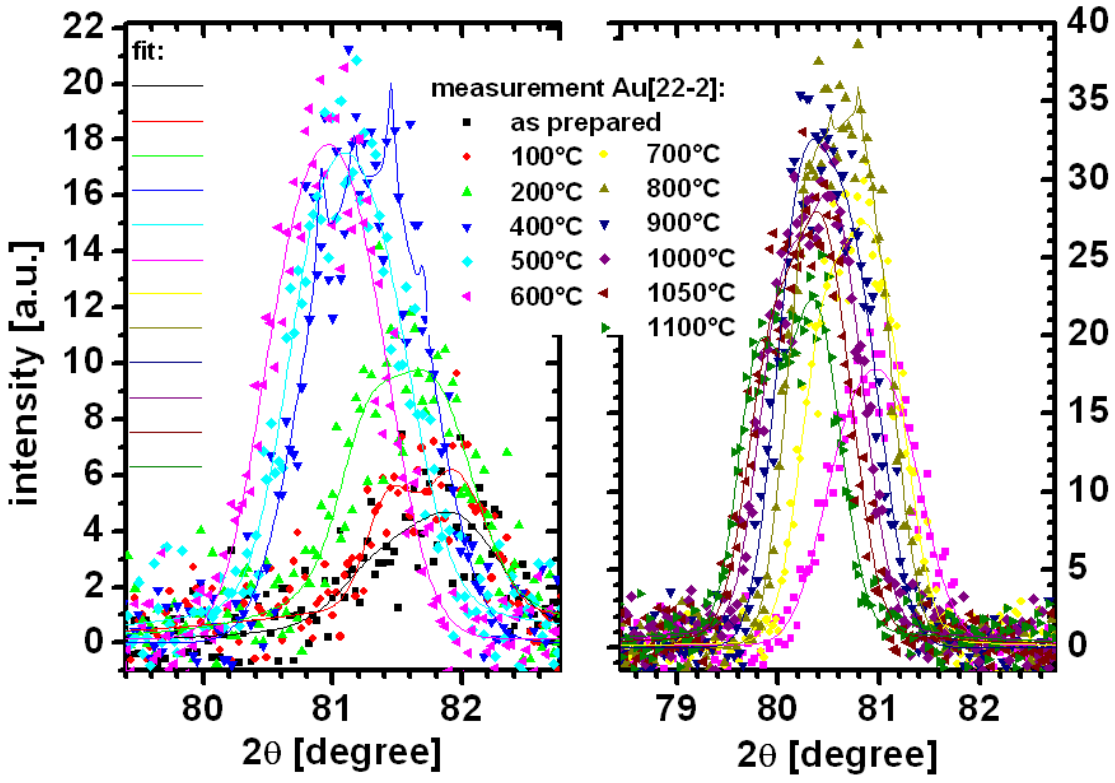

Figure 6.24: in-situ measurement of 22-2$_{\{111\}}$ and -222$_{\{511\}}$ gold peaks as well as their corresponding fits. Because of the small intensity noise gets stronger and therefore a well made fit isn't possible.

6.2.1. Williamson Hall plot

As above discussed a Williamson Hall plot calculation only in specular (111) direction was possible calculating because of small measured intensities and the unknown diffraction background as well as the off specular superposition of the two different diffraction peaks caused by existing {111} and {511} textures. So in figure 6.25 the calculated Williamson Hall plot of gold (111) layers are displayed. The gradient of the line is proportional to the micro strain and the origin of the line (abszisssa=0) is inverse proportional to the crystal size. At this point it is to be underlined that the physical quantities micro strain and crystal size do not have to be the same quality in every crystallite direction. Therefore a crystallite size calculation by Scherrer equation also was done. The first reason of calculating crystal size by Scherrer was getting a comparative crystal size temperature development in specular (111) direction to Williamson Hall plot calculation. At second with Scherrer technique it was possible to calculate the crystallite size in off specular direction (11-1).

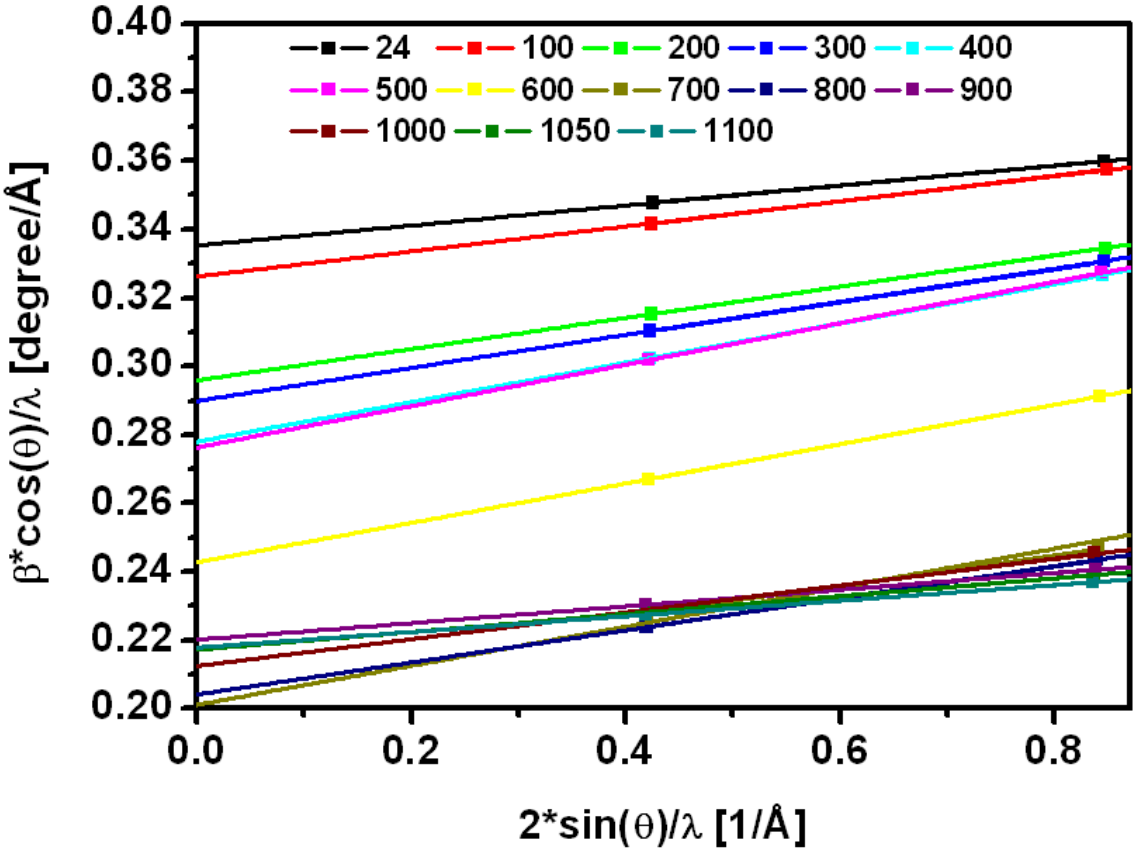

Figure 6.25: Williamson Hall plots of the gold sample K13 (20nm), calculated of all insitu measured temperature in 100℃ steps (β..integral 2θ-peak-breath)

At second it must be said that the error bars of calculated crystallite size were discovered comparably greater with Scherrer technique because of unknown diffractometer background as well as the great error bars of the calculated area under the diffraction peak calculating the integral breath of corresponding diffraction peak. So the high error bar of calculated area was inserted into Scherrer equation directly, but with Williamson Hall plot technique they were smoothed because of linear fitting technique.

In figure 6.26 the vertical crystallite size developments are displayed. It is clearly visible that the quality of specular calculated crystal size with Scherrer technique is similar to development calculated by Williamson Hall plot technique. So in the beginning of thermal annealing process there was a small crystal size increasing found until the temperature of 500℃, where the ex-situ thermal annealed samples cracked and got a macroscopic inhomogeneous surface. After that temperature a strong crystal size increasing was calculated while increasing the temperature per a 200℃ interval. Afterwards the crystal size increasing process was detected to stagnate. Moreover with Williamson Hall plot technique a small decreasing crystal size was observed in this temperature section. At first it must be underlined that the Williamson Hall plot technique calculating crystal sizes get more inexact because of higher rounding errors. At second it should be remembered that in this last temperature section a small gold evaporating process can start and therefore a crystal size decreasing in this temperature section is truly possible.

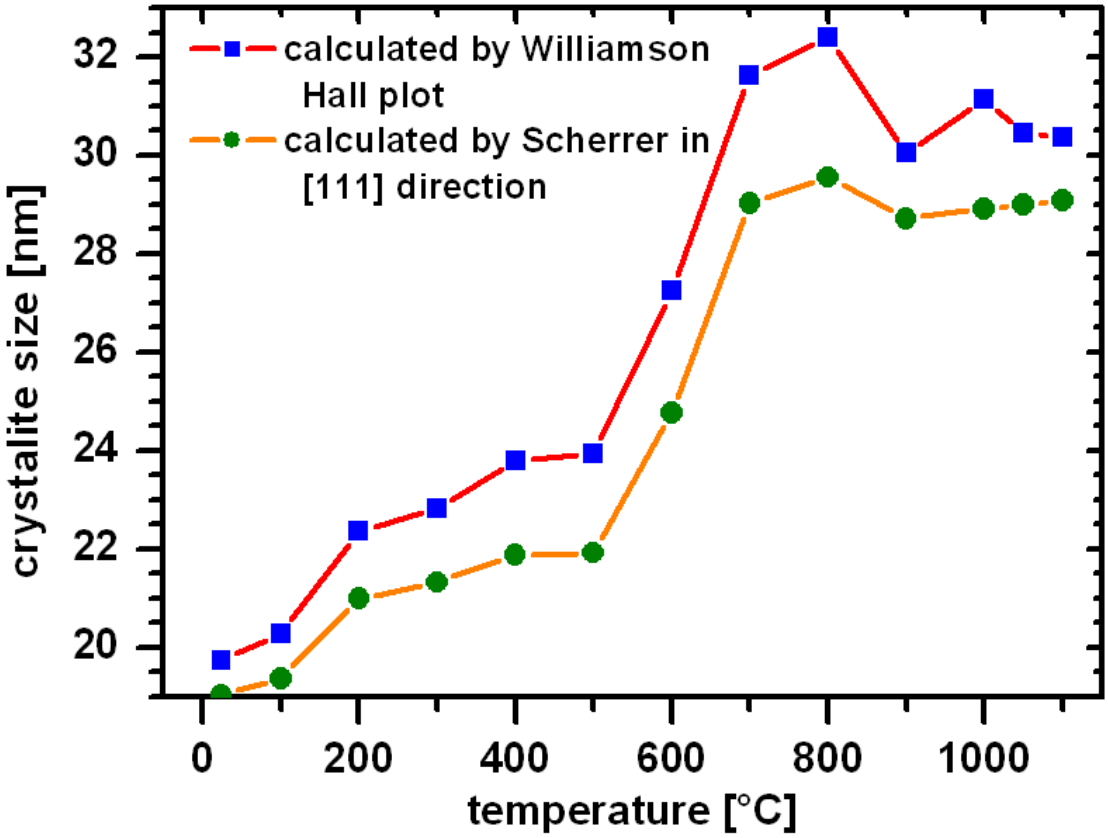

Figure 6.26:vertical crystallite size of the gold sample K13 (20nm) calculated with the gradient of the specular Williamson Hall plot as well as by Scherrer equation of all in-situ measured temperatures in 100℃ steps.

In figure 6.27 the micro strain, calculated by Williamson Hall plot, is displayed. It is clearly visible that the temperature of 500℃ is critical again. So at this temperature the maximum of calculated micro strain was found. Comparing the ex-situ thermal annealing measurement series and the corresponding calculated lattice constant development quality, it is clearly reproducible that the in-situ measured and calculated micro strain quality is inverse.

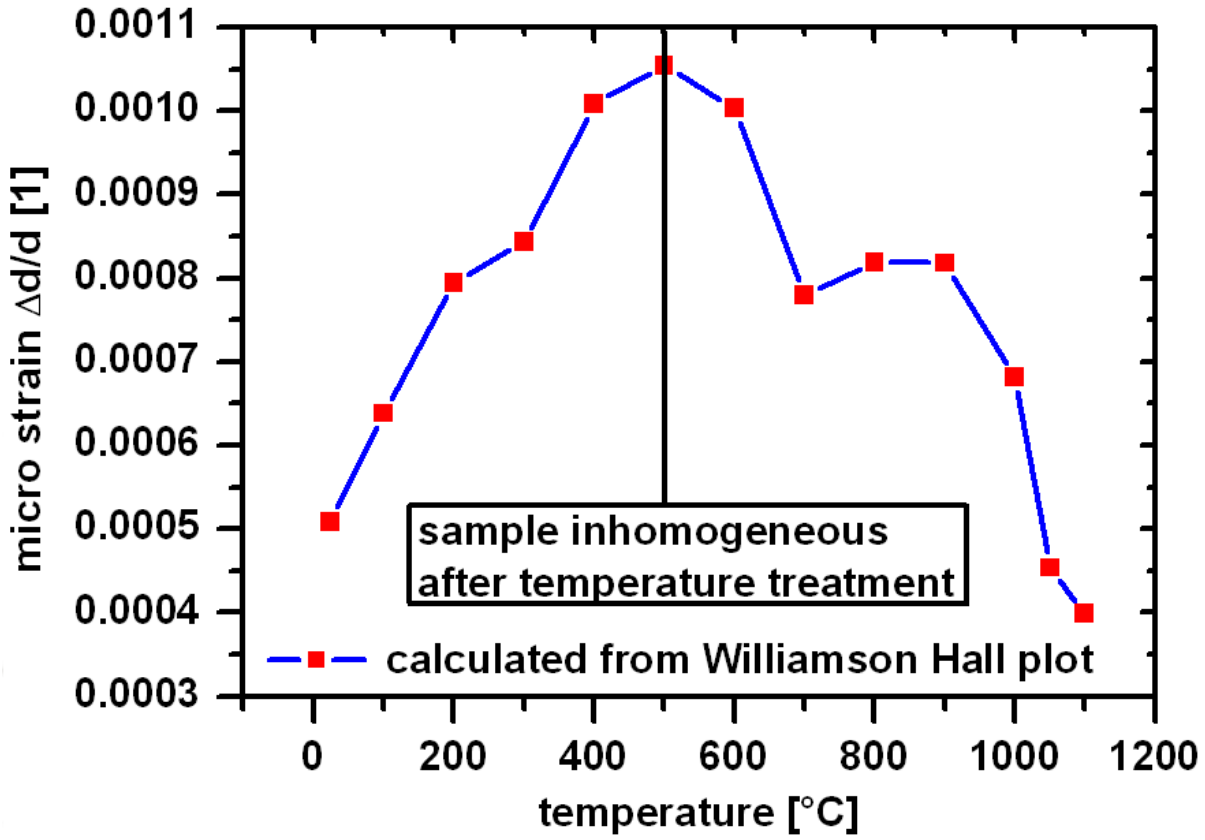

Figure 6.27: in-situ measured micro strain of the gold sample K13 (20nm) calculated with the gradient of the specular Williamson Hall plot normal to (111) layer.

6.2.2. thermal expansion coefficient

After fitting the in-situ measured diffraction peaks the θ position of the peaks were known. With formula (3.8), which is a perform of the popular Bragg equation, the lattice constants for each measured temperature were calculated. Then a linear fit was made calculating the linear thermal expansion coefficient $\alpha=(\Delta a/a)/\Delta T$.

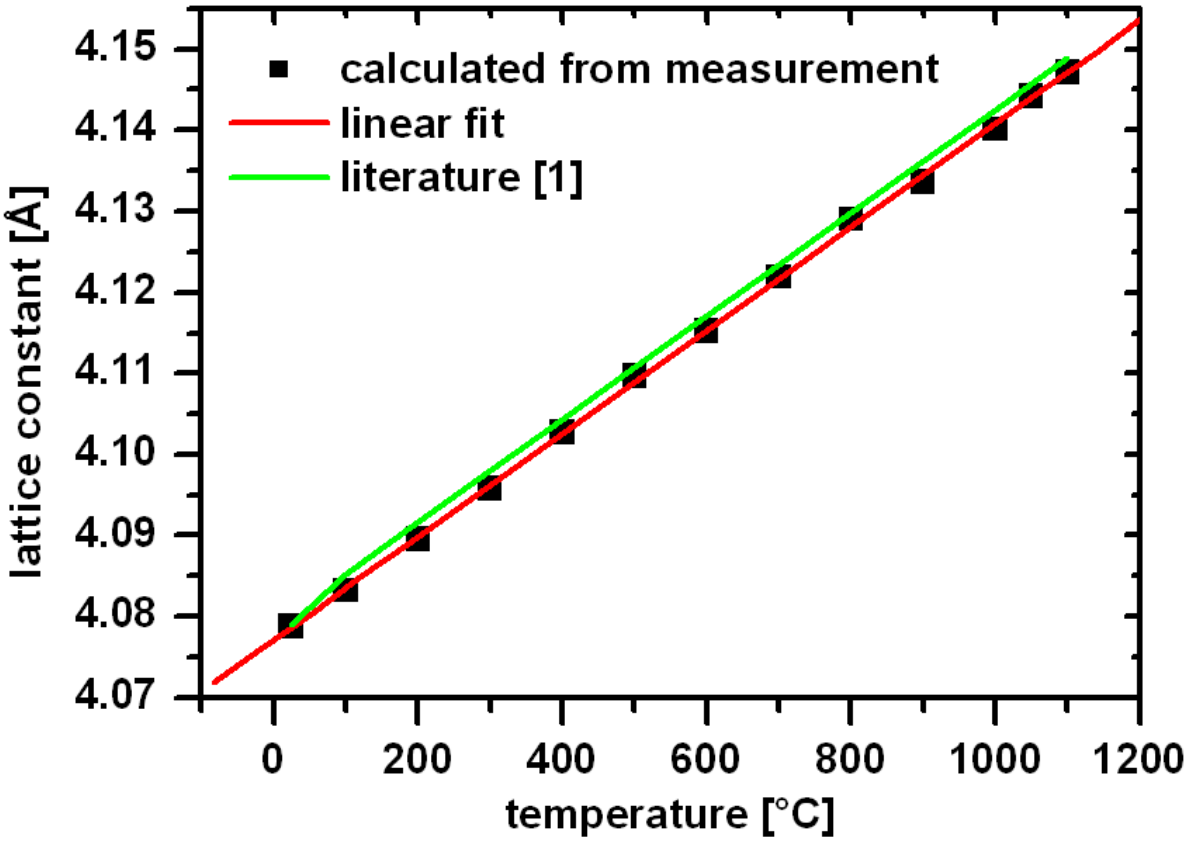

Figure 6.28: calculated lattice constant of the gold sample K13 (20nm) at different temperatures insitu measured in 100℃ steps. The la ttice constants as well as the calculated expansion coefficient are consistent very good with literature.

In figure 6.28 the calculated fit as well as the literature [1] value and the corresponding quality are displayed. The calculated linear thermal expansion coefficient α is displayed and compared with literature values in table 6.1.

Literature [1]	$\alpha=13{,}4\times10^{-6}\ C^{-1}$
Literature [36]	$\alpha=14{,}2\times10^{-6}\ C^{-1}$
Calculated from measurement	$\alpha=15{,}6\times10^{-6}\ C^{-1}$

Table 6.1: comparing linear thermal expansion coefficient α of gold

6.3. scanning electron microscopy

Investigations with SEM (scanning electron microscopy) after thermal annealing with 500℃ and higher show different morphologies on the annealed samples. An ex-situ SEM investigation of all found different morphologies was made at different positions. Secondary electron images (SE) show the topography contrast of the sample and back scattered electron images (BSE) the phase contrast. Back scattered electrons (BSE) are scattered at the atomic nucleus. The lighter an image area is visible, the higher atomic number of the scattered nucleus in this area is observed. Moreover at each morphology an EDX (energy dispersive X-ray spectroscopy)-spectrum investigation with two different primary beam energy, 3keV and 5keV, represents an elementary analysis of the different morphologies. The higher the used energy the thicker is the observed layer. At second, in-situ temperature annealing SEM measurements were made observing the morphology changing centre as more the starting temperature of the changing process. Furthermore FIB (focused ion beam) ex-situ measurements were made observing the two morphologies, which mostly exist on all 500℃ and higher temperature annealed samples (see chapter 6.1). Because of new others morphologies on 100nm gold sample K19, made in Graz, in-situ thermal annealing investigations with SEM (scanning electron microscopy) are illustrated firstly. Ex-situ SEM investigations of all found morphologies of gold samples after thermal annealing are illustrated in the second part of this chapter.

6.3.1. in-situ investigations

At first the 100nm gold sample K19 was cut into smaller parts, because the specimen holder of the SEM thermal annealing process had a cross section dimension of 0,6cm and therefore original size of 2x2 cm was too large. The first sample was thermally annealed up to 400℃, afterwards the thermal annealing temperature was increased step by step until gold layer cracks was registered at the temperature of 450℃. Then the temperature was kept constant. While the gold layer cracking process at this constant temperature of 460℃ was going on, a SEM (scanning electron microscopy) video was made visualizing the whole morphology changing process. After the changing process got stationary and no gold layer changes were registered anymore, the temperature was increased up to 800℃. At higher temperatures no changes of gold layer were registered by scanning electron microscopy. In figure 6.29 some SEM (scanning electron microscopy) images of the adjusted video are shown. It is clearly visible that the origin of the gold layer cracking off process was located at a position where the thermal oxidized silicon layer had been damaged as before. This conclusion was registered at all thermal annealed samples, also visible in figure 6.30. This sample was thermally annealed with continuous increasing temperature. The end result is circular changed area with different morphologies around the cracked SiO_2 layer. This conclusion was also found at the ex-situ thermal annealed gold samples. In the middle of these circular morphology changed areas pyramidical morphology always was located, see next chapter.

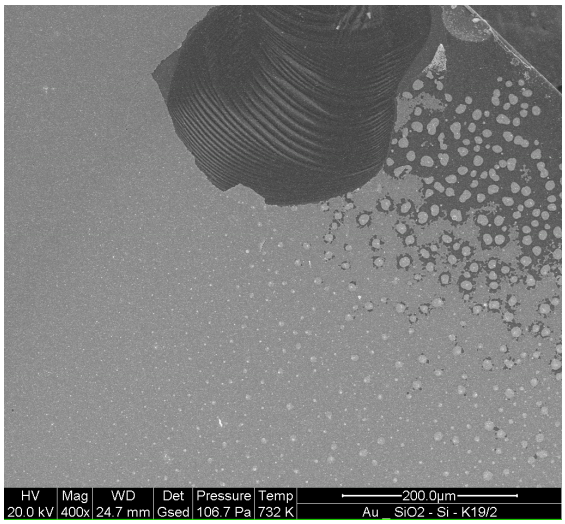

a.) t(video beginning)≈30s, T=459℃

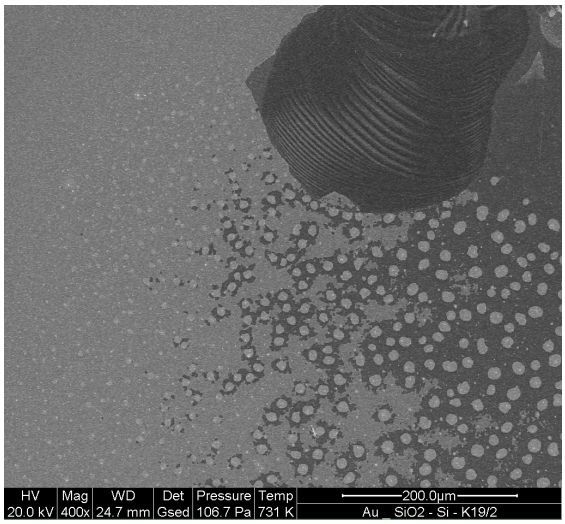

d.) Δt=390s, T=458℃

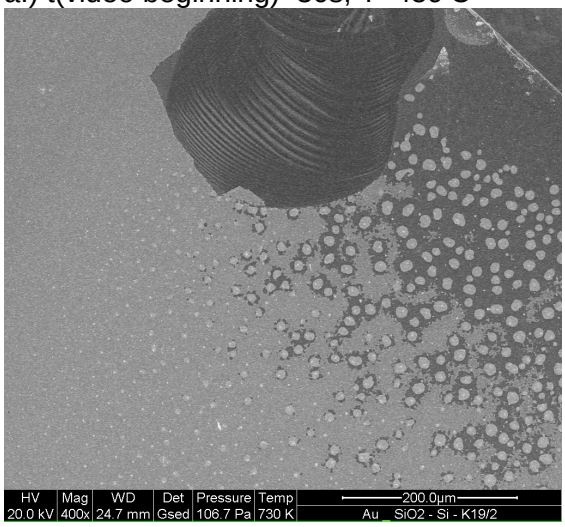

b.) Δt=130s, T=457℃

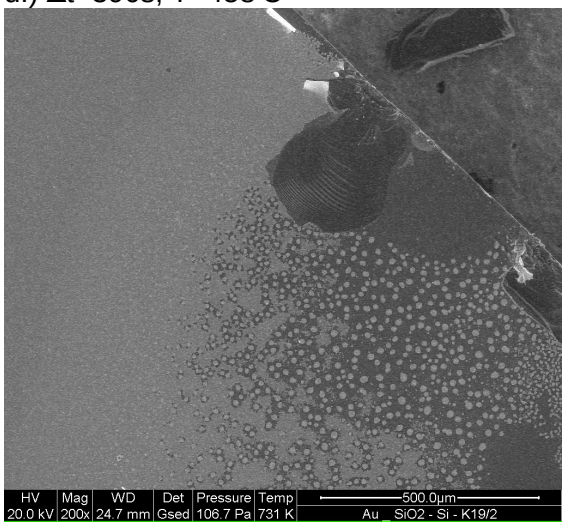

e.) Δt=600s, T=458℃

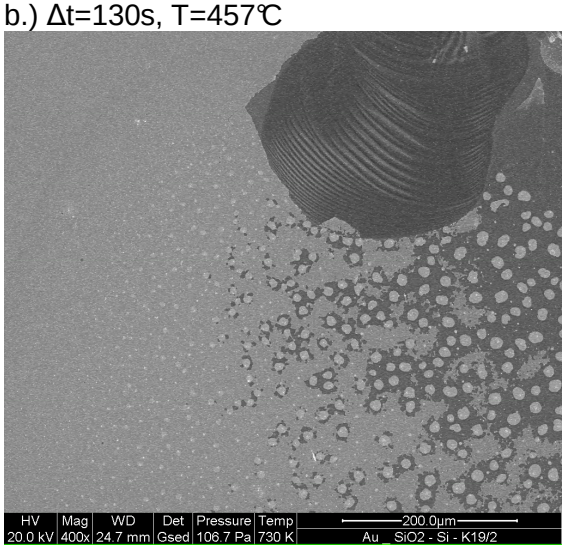

c.) Δt=260s, T=457℃

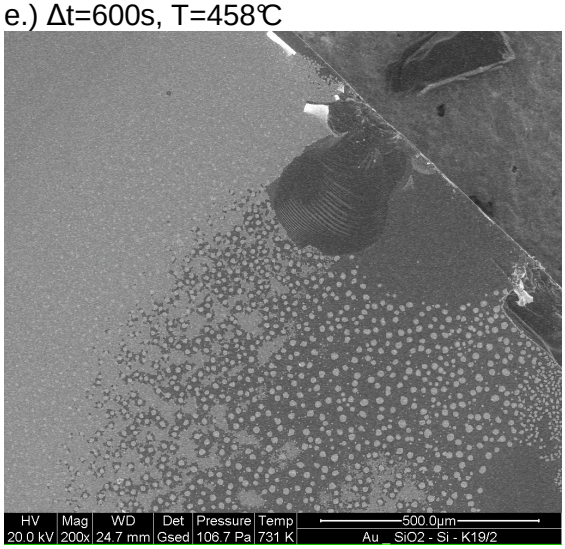

f.) Δt=1000s, T=458℃

Figure6.29: SEM (Scanning Electron Microscopy) images of in-situ measured SEM video while thermal annealing process with constant temperature T of 100nm gold sample K19/2: **a.)** first SEM image of video; **b.) - f.)** SEM images measured about Δt (time difference to video beginning) later

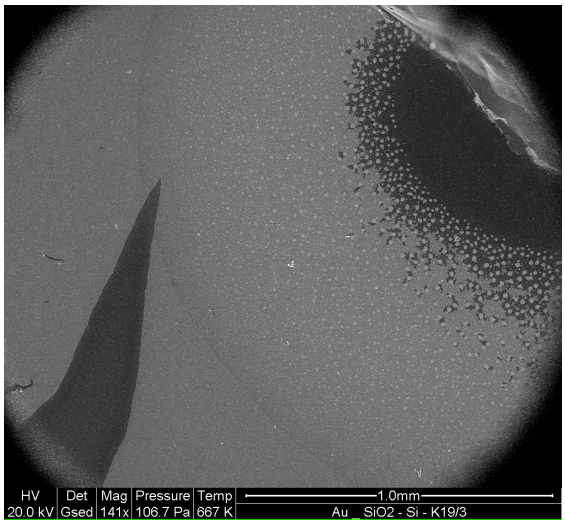

a.) t(video beginning)≈200s, T=394℃

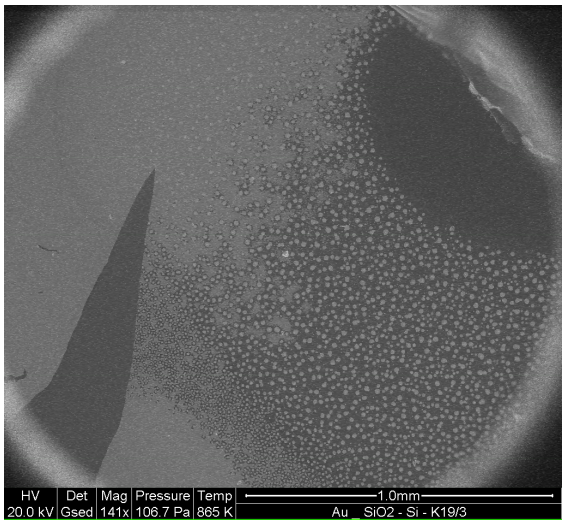

d.) Δt=12min T=592℃

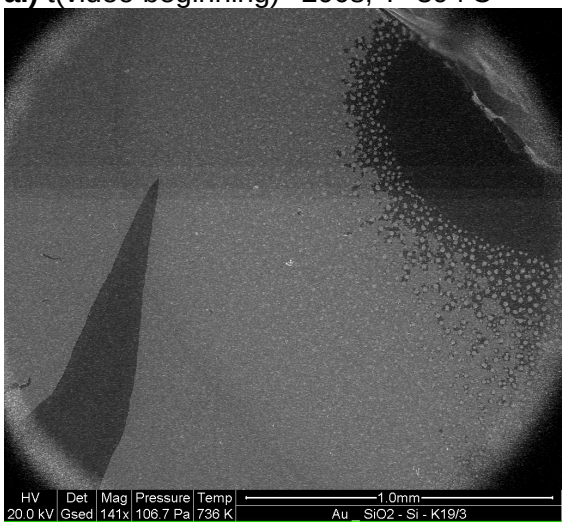

b.) Δt=4min, T=463℃

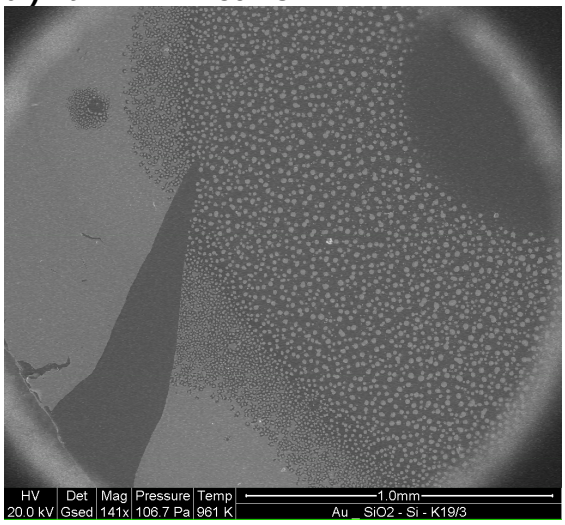

e.) Δt=16min, T=688℃

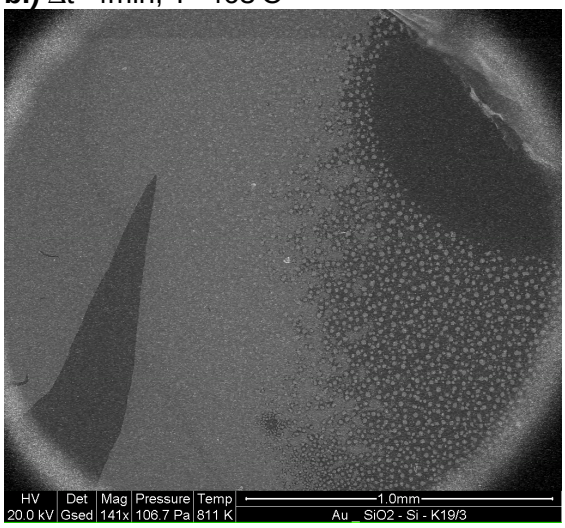

c.) Δt=8min, T=538℃

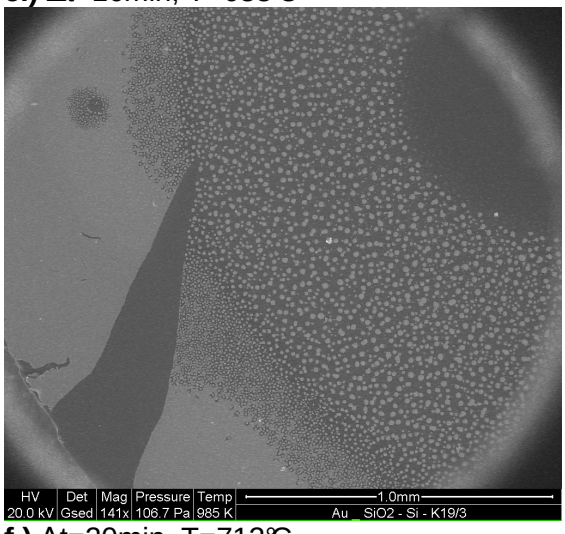

f.) Δt=20min, T=712℃

Figure6.30: SEM (Scanning Electron Microscopy) images of in-situ thermal annealing measured SEM-video with increasing temperature Tof 100nm gold sample K19/3: **a.)**first SEM image of video; **b.) - f.)** SEM images measured about Δt (time difference to video beginning) later

6.3.2.ex-situ investigations

Ex-situ SEM (scanning electron microscopy) measurements observing the different morphologies after thermal annealing was made with varying annealed samples. So after 12h annealing time for each 100℃ step up to 900℃, after 12h annealing at 500℃, and after 79h annealing at 500℃. The most d istinctive morphologies exist on sample K12, which was thermally annealed at 500℃ a bout 12 hours and in a second step about 67 hours. Because of showing similar morphologies the other with DHS900 thermal annealed gold samples are represented by ex-situ measured SEM- and EDX-images of sample K12 in this chapter. Moreover other morphologies were found on the thermal annealed samples K19/2 and K19/3, which were prepared in Graz and thermally annealed while in-situ SEM measurements (see chapter 6.3.1). Therefore these morphologies are also represented in this chapter. Moreover the great difference between the thermally annealed samples with DHS900 and the others is the fact that the origin of the gold cracking process is in the middle of the sample and at the in-situ SEM thermal annealed measured samples K19/x the origin is given by the sample edge (see figure 6.29 and 6.30).

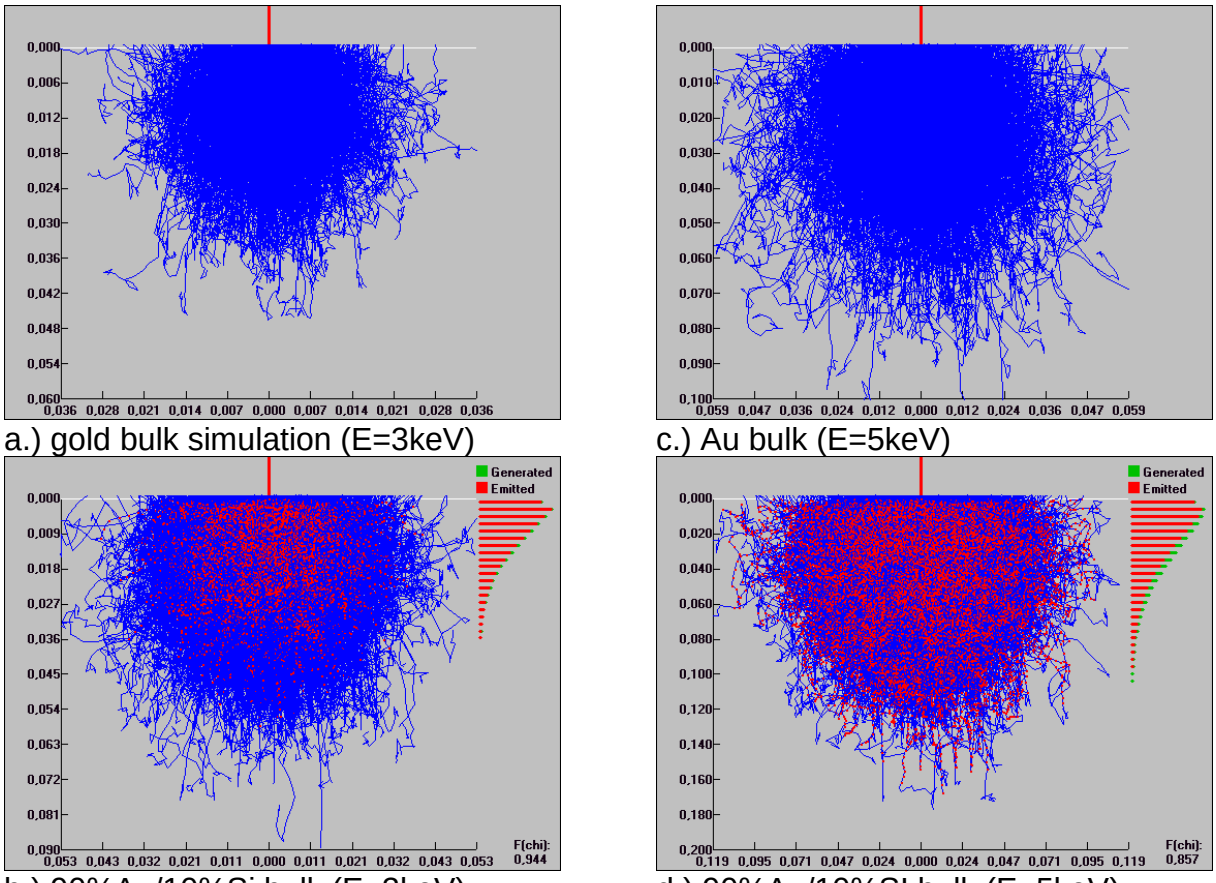

a.) gold bulk simulation (E=3keV)

c.) Au bulk (E=5keV)

b.) 90%Au/10%Si bulk (E=3keV)

d.) 90%Au/10%SI bulk (E=5keV)

Figure 6.31: simulations of electron penetration (scale µm) into denoted bulk using electron energy E

Before studying all different morphologies theoretical electron depth of impression, also called penetration, was simulated by a computer program. Because the original gold layer thickness was 100nm and thicker, there was searched an electron energy with a maximal range of 100nm. As in figure 6.31c.) visible this condition is fulfilled with an electron energy of 5keV for gold bulk. At second a smaller electron energy was searched fulfilling the following condition: The electron depth of impression should be smaller than the half original gold layer thickness analyzing the chemical composition of the gold hills surfaces and comparing with the higher electron energy measurements. This condition was perfectly fulfilled with the electron energy of 3keV, see simulation in figure 6.31a.). At this point it should be noted that the electron depth of impression in a gold silicon bulk with the same energy gets smaller if there exist a gold silicon composition bulk, see figure 6.31b.) and 6.31d.).
In figure 6.32a.) a SE (secondary electrons) image of non cracked gold layer is displayed, denoted with morphology 1. On every thermal annealed sample this morphology was found. The EDX (energy dispersive X-ray) spectrum, displayed in figure 6.32b.), verify that morphology 1 is an only gold layer. The existing O and C peaks are explainable with area contamination. Therefore in the EDX (energy dispersive X-ray) spectrum of the same morphology, but measured with smaller electron energy 3keV, a greater ratio of the O and C peaks in relation to the Au peak was measured (see figure 6.32 c.), because of the smaller electron depth of impression.

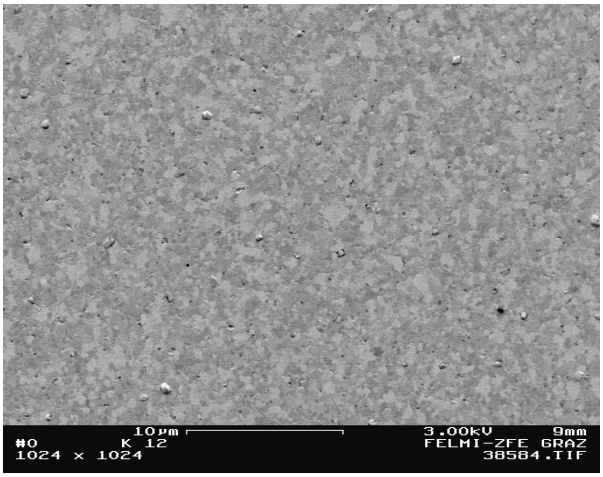

a.) K12 – morphology 1

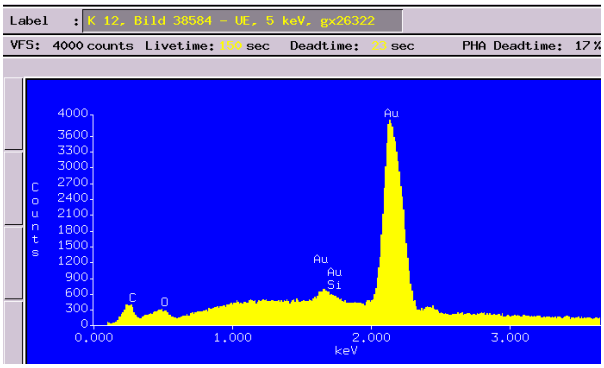

b.) EDX in a.) (all around) – 5kev

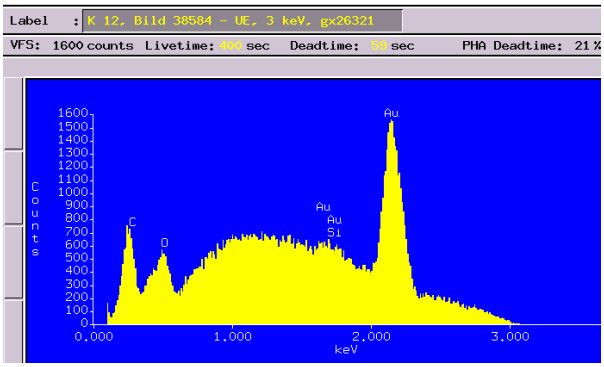

c.) EDX in a.) (all around) – 3kev

Figure 6.32: a.)SE (Secondary electrons) image of morphology 1 on sample K12, measured after 12h+67h thermal annealing (500℃) **b.)+c.):** EDX (energy dispersive X-ray) spectrums of a.) with b.)5keV and c.) 3keV electron energy

In figure 6.33a.) further four different morphologies are signified. This image represents all over 500℃ thermal annealed gold sam ples, because this gold hill morphology together with all intersection morphologies were found on all these samples. There exist two types of gold hills, in figure 6.33a.), which are signified with 1 and 38581. Comparing the significant EDX measurements, that is displayed in 6.33c.)+g.), at gold hills with different electron energy and therefore different electron range, the following can be concluded:

- on the hill surface silicon exist additionally

The significant difference between the two hills is the ratio of silicon peak to gold peak in the measured EDX spectrums. So this ratio of the first signified hill [1], noted as morphology 2, is considerable smaller than the silicon gold ratio of hill [38581], which is enhanced displayed in figure 6.33e.), and which is noted as morphology 3. If there exists a alloy compound or only a gold-silicon mixture cannot be determined clearly.
The fourth significant morphology is signified with 2 in figure 6.33a.). In the first moment it looks like an non destroyed substrate surface area without any gold. This intention can only partially be proved. So the with 5keV measured EDX-spectrum in this area, which is displayed in figure 6.33 d.), proves the existing intact SiO_2 layer from substrate. But the EDX-spectrum in figure 6.33h.), which was measured with 3keV, accounts for existing some gold particles in this area.
Otherwise it is very interesting that on the fifth morphology, which is signified with [3] in figure 6.33a.), and which looks like a mixture of gold layer areas and substrate surface areas, generally no gold was detected in the substrate surface area by EDX measuring, see figure 6.33f.).
It seems that two different ways of gold layer cracking were happened while the thermal annealing process. On the one hand a gold diffusion process is possible, on the other hand an evaporating process could be happened.
The sixth significant morphology is the most interesting one of all. It is signed in figure 6.34a.) and is enhanced displayed in figure 6.35a.) and 6.35e.). This morphology looks like a pyramidical cut into the substrate. Moreover all as discussed measurements let be proved this pyramidical morphology as the origin of the gold layer cracking process. The area around this morphology seems to be a circular area with an existing gold monolayer. There was no connection between circle size and thermal annealing time discovered. Around this circular area always gold silicon as well as only gold hills were discovered like in figure 6.33a.) is displayed. The area around this hill structure was not always filled on with the same morphology. So in this area of some thermal annealed gold samples with 500℃ and higher temperature cracked gold layer was discovered. On the other hand on this area section closed gold layer, gold needles, as well as gold layer island with existing small grooves between the existing gold layers were detected. The different morphologies in this area section seem to be in connection with the thermal annealing time as well as with the original gold layer thickness.

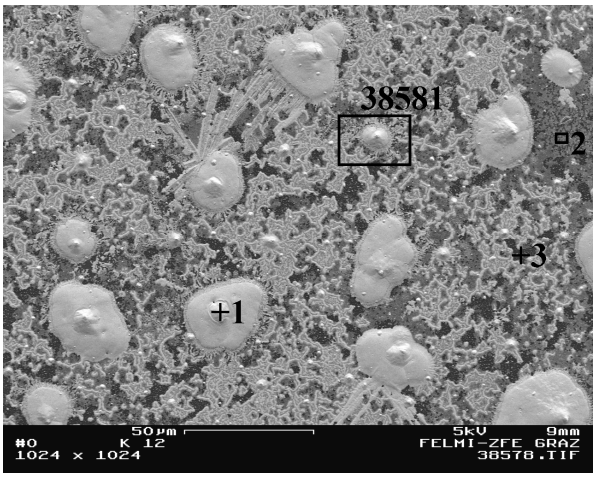

a.) SE image of sample K12

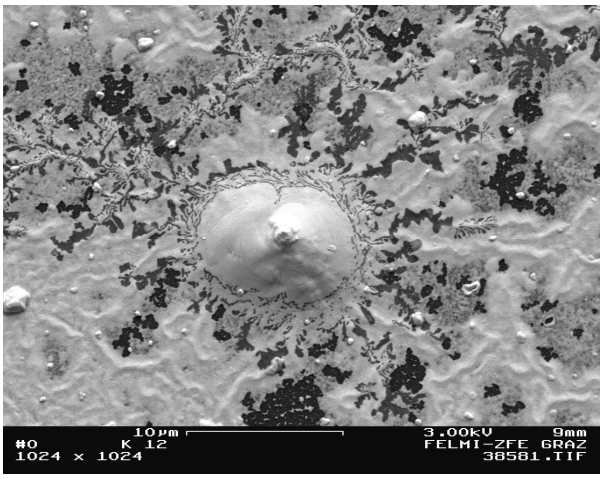

e.) enhanced SE image of place 38581 in a.) –

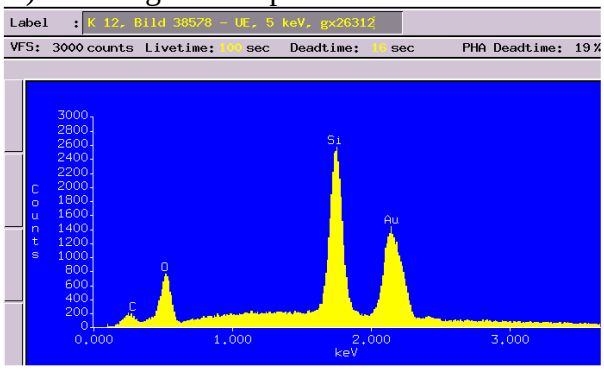

b.) EDX spectrum of a.)[all around] – E=5kev

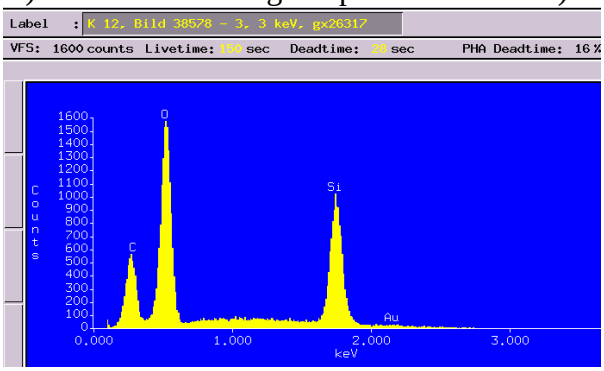

f.) EDX spectrum of zone [3] in a.) – E=3kev

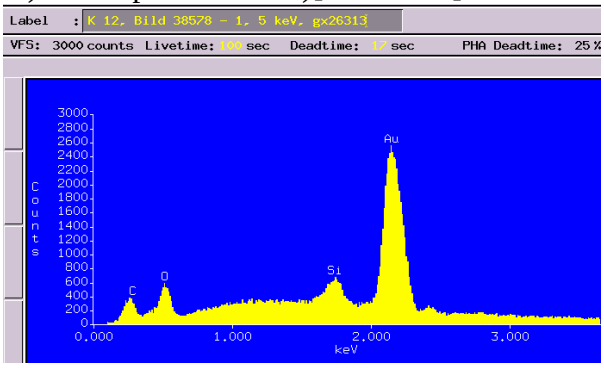

c.) EDX spectrum of zone [1] in a.) – E=5kev

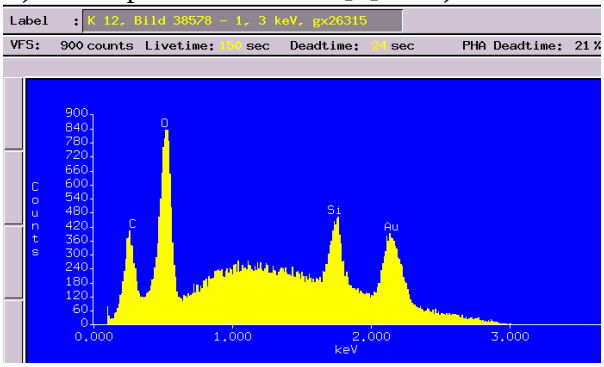

g.) EDX spectrum of zone [1] in a.) – E=3kev

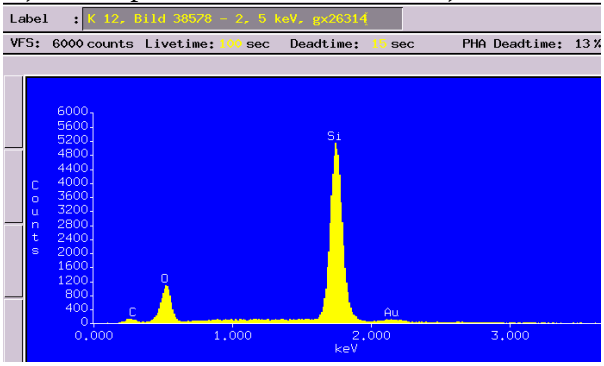

d.) EDX spectrum of zone [2] in a.) – E=5kev

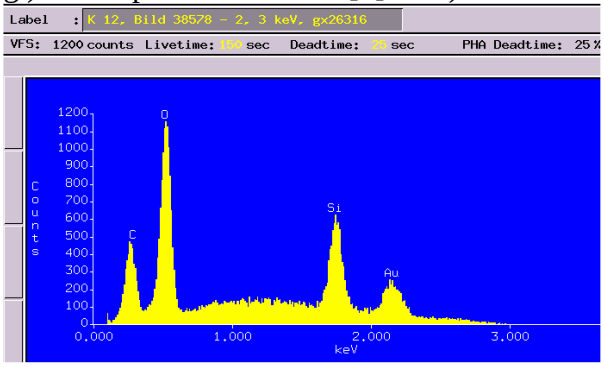

h.) EDX spectrum of zone [2] in a.)– E=3kev

Figure 6.33: a.)SE (Secondary electrons) image of sample K12 measured after 12h+67h thermal annealing (500℃) with three different mark ed morphologies **e.)** zoomed SEM image of a.) at place 38581. EDX (energy dispersive X-ray) spectrums focused on the three marked morphologies, measured with **b.)c.)d.)** 5keV and **f.)g.)h.)** 3keV electron energy

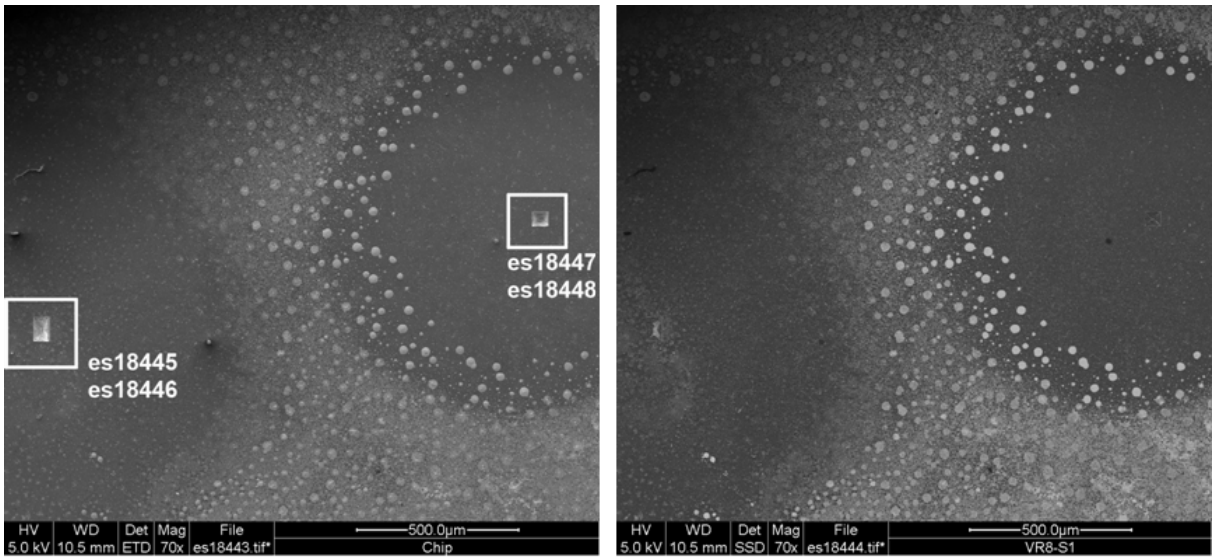

a.) K12 SE (Secondary electrons) image b.) K12 BSE (Back Scattered Electrons) image

Figure 6.34: SE image **(a)** and BSE image **(b)** of 100nm gold sample K12 after 12h+67h thermal annealing at surrounding area of pyramidical morphology (inside the white rectangle)

A SE(secondary electron) image generally show topography contrast. But a BSE(back scattered electrons) image generally show phase contrasts. The lighter the BSE image the higher is the average atomic number. So in figure 6.34b.) the right pyramid is nearly cleared away, because the gold was nearly removed of it as well as from the surrounding circular field. The left pyramid in BSE image 6.34b.) is partially visible because of still existing local gold rests as well as in the surrounding circular field. This is a second indication that the formation of a pyramid is equal with starting formation of the circular non gold field. The gold seems to be disappeared simultaneously.

In figure 6.35a.)+e.) the left pyramid of figure 6.34 is enhanced displayed. At first it seems that the gold stayed for longest time at the outside edges of the pyramid. At second six zones are marked in figure 6.35a.), where the EDX investigation were measured with 5keV. They are all displayed in figure 6.35. Because of the high used electron energy and the small gold layer thickness (<100nm) the analysis depth is definitely higher as the gold layer.

The Analysis zones 1 -4 are located deeper as the SiO_2 layer. This conclusion was made because of the small oxide peaks in zones 1 and 3, which was interpreted as an air contamination oxide layer. Surprising is the fact that in the same depth the zones 2and 4 are covered with a gold layer, because the pyramid was primary developed after gold evaporating and while thermal annealing process. The conclusion was made that the gold subsequently diffused to there.

First of all because of the small thickness of the gold layer of this sample it was not possible discovering definitely if in the pyramid exist regional gold oxide or gold in connection with silicon. The oxide concentration is in any case to small connecting all existing gold in zones 2 and 4. Maybe the compounding of this local layer also vary like in the hills out of the pyramid.

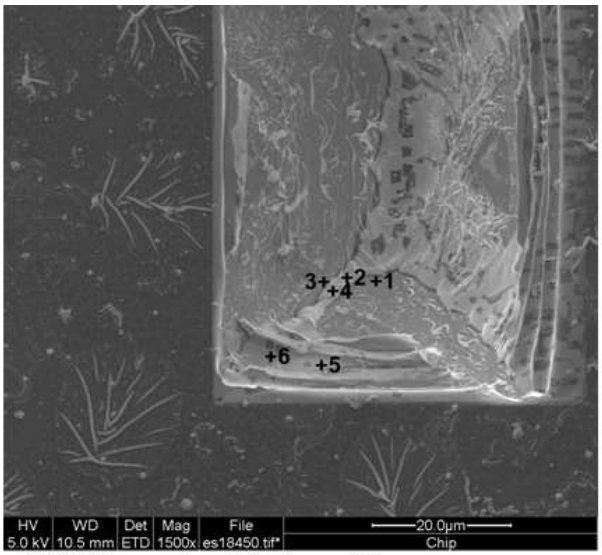

a.) SE (Secondary Electrons) image

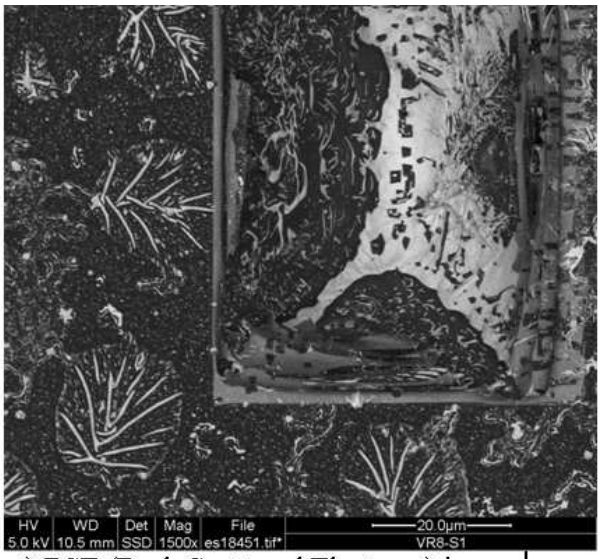

e.) BSE (Back Scattered Electrons) image

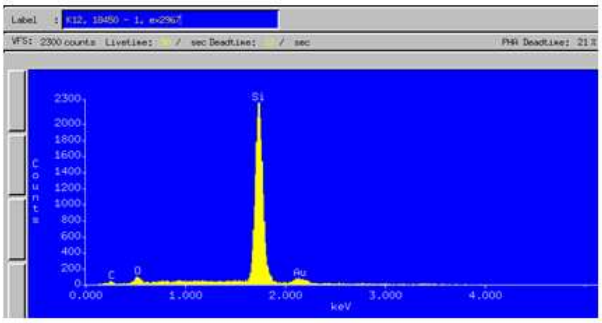

b.) EDX-spectrum of zone 1 in a.)

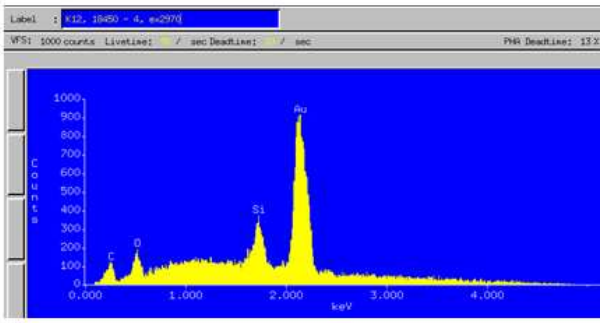

f.) EDX-spectrum of zone 4 in a.)

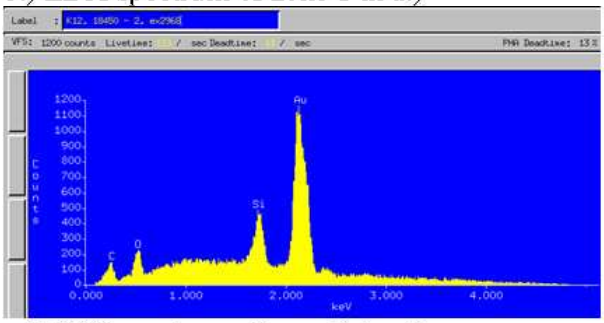

c.) EDX-spectrum of zone 2 in a.)

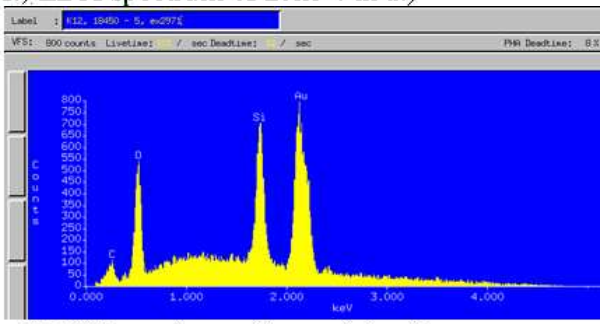

g.) EDX-spectrum of zone 5 in a.)

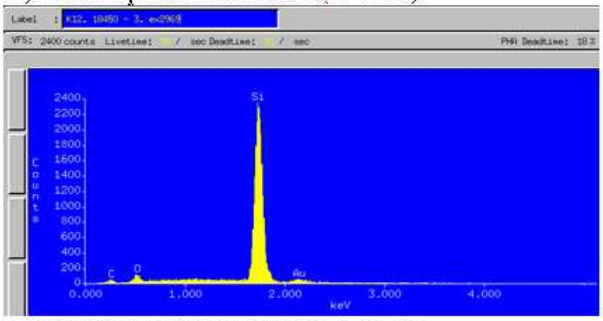

d.) EDX-spectrum of zone 3 in a.)

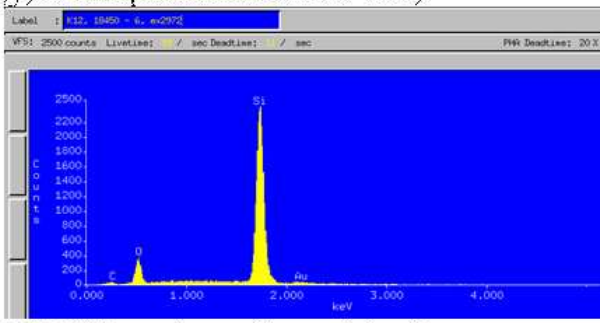

h.) EDX-spectrum of zone 6 in a.)

Figure 6.35: SEM (secondary electron microscopy) images (**a+e**) of pyramidical morphology on sample K12 (100nm) after 12h+67h thermal annealing (500℃) and the corresponding EDX spectrums, measured with 5keV electron energy at in a.) assigned zones 1(**b**),2(**c**),3(**d**),4(**f**),5(**g**), and 6(**h**)

The in Graz evaporated gold sample K19 was cut into smaller parts before in-situ thermal annealing scanning electron microscopy investigations were made. Because of the small samples no complete circular morphology changed field was developed while thermal annealing process. At second no pyramidical morphology was detected on these small samples after thermal annealing process. This fact seems reasonable because the origin of the circular field was always discovered by a destroyed sample edge. So it was observed with scanning electron microscopy while all in-situ thermal annealing measurements. It is also reproducible by the end station of morphology changing process, visible in figure 6.36 and 6.39a.).
On the other hand the small area and the other morphology changing origin seems to be the reason that on this small gold samples further others morphologies were discovered. These morphologies are displayed as well as discussed in the following pages.

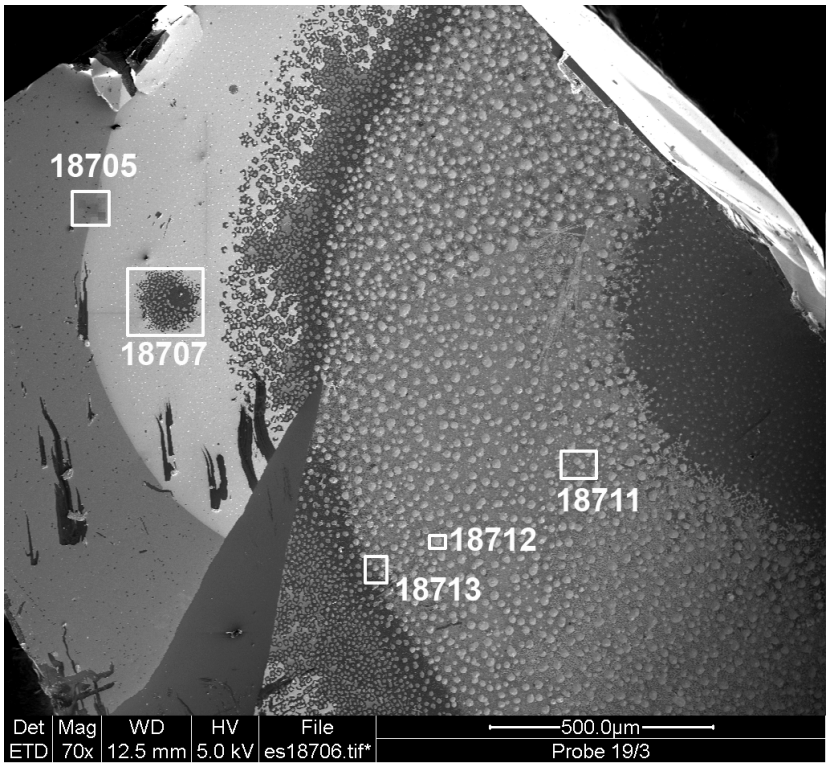

Figure 6.36: SE (secondary electrons) image of sample 19/3 after thermal annealing process

The difference between the first and the so noted seventh morphology, which is enhanced displayed in figure 6.37a.)+d.), and which is signified with 18705 in figure 6.36, is the fact that beside the closed gold layer on the left side a greater carbon concentration was measured by EDX technique. Therefore the BSE image (see figure 6.37d.)) show different lightness.
The eight morphology, see figure 6.37b.)+e.), is probably composed of islands of the origin gold layer. They exist of clean gold, silicon could not be detected with the possible detection sensitivity. Between the islands original SiO_2 – layer of the substrate was detected.
Morphology nine, which is signed as 18712 in figure 6.36, and which is enhanced displayed in figure 6.37c.), seems to be an advanced form of morphology 3 (see figure 6.33e.)). On the hills were gold as well as silicon structures detected. The high carbon peak of EDX spectrum (see figure 6.37f.)), and probably also the oxide peak exist because of contamination. The smaller the used electron energy by EDX

investigating, the smaller is the electron depth of impression. Therefore the contamination layer on surface was measured stronger (see figure 6.37f.)).

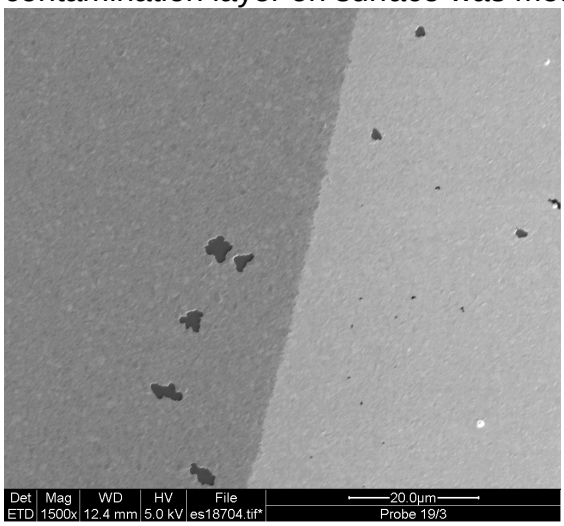

a.) SE image of morphology 7

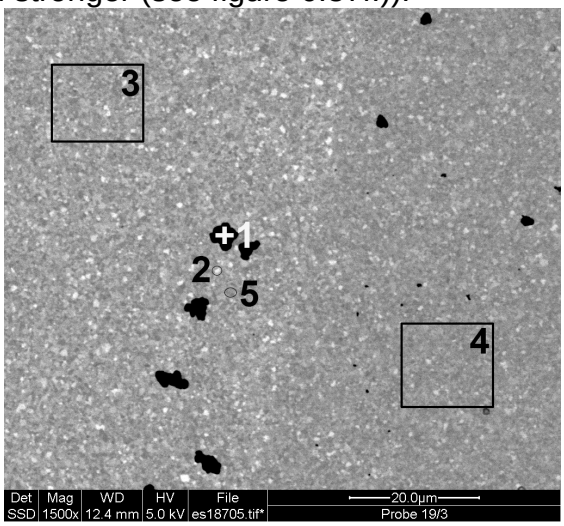

d.) BSE image of morphology 7

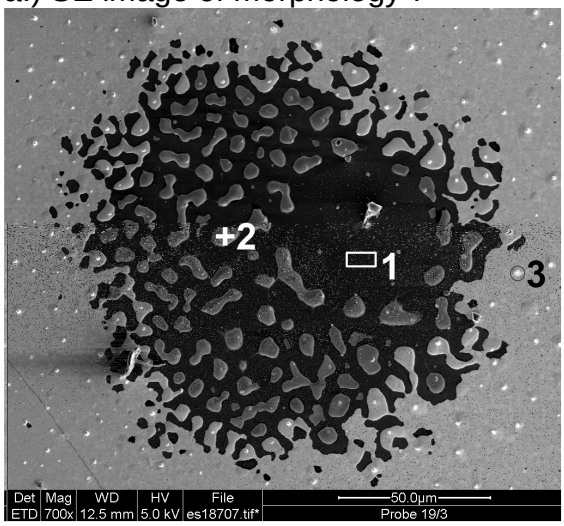

b.) SE image of morphology 8

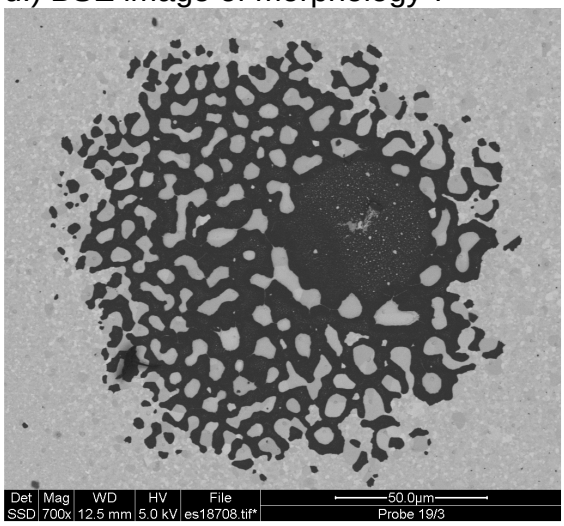

e.) BSE image of morphology 8

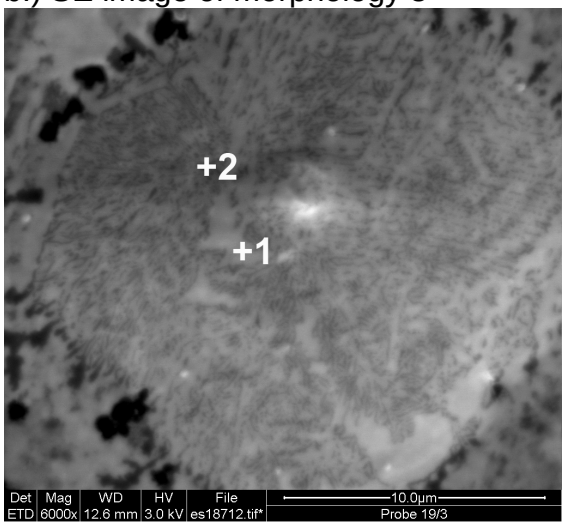

c.) SE image of morphology 9

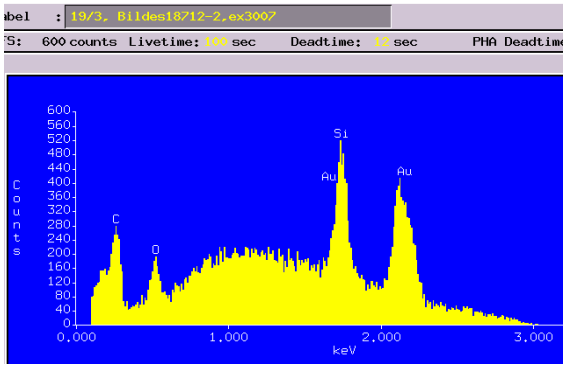

f.) EDX spectrum of zone 2 in c.), E=3kev

Figure 6.37: a.) - c.) SE secondary electron images **d.) + e.)** BSE back scattered electron images of sample K19/3 after thermal annealing process **f.)** EDX spectrum of morphology 9

The supposition that morphology nine (see figure 6.37c.)) is a advanced form of morphology 3 (6.33a) was confirmed by studying the gold hill border area, which is signed in figure 6.36 with 18713, and which is displayed on figure 6.38a.). So on the left side morphology two was detected and on the right side morphology three (see figure 6.38b.)) was detected. The structured hill seems to be covered with a homogeneous layer in the above part. The structures in the hill go from outside to inside.

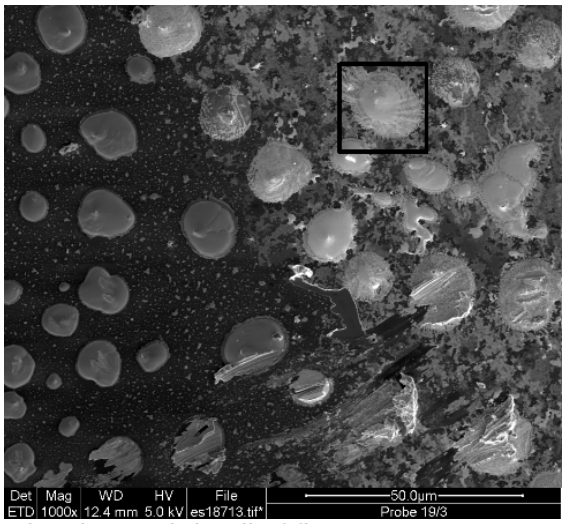

a.) enhanced detail of figure 6.36 at 18713

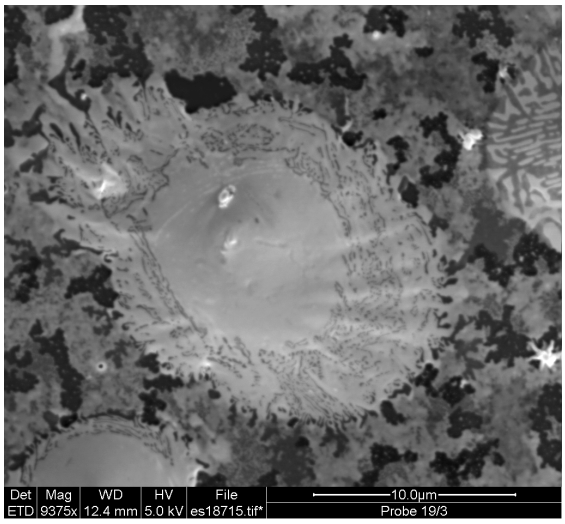

b.) enhanced detail of 6.38a.)

Figure 6.38: SE (secondary electron) images of sample K19/3 after thermal annealing process: **a.)** detail signed on figure 6.36 with 18713 **b.)** enhanced detail of a.)

On sample 19/2 skeletal morphology ten was detected. In contrast to sample K19/3 this sample was thermal annealed with a constant temperature of circa four hundred degree Celsius. The skeletal morphology ten was not analyzed by EDX technique investigations.

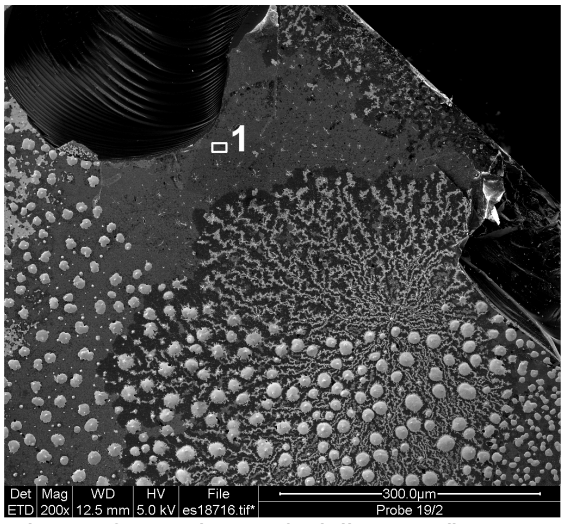

a.) SE of sample K19/2 (all around)

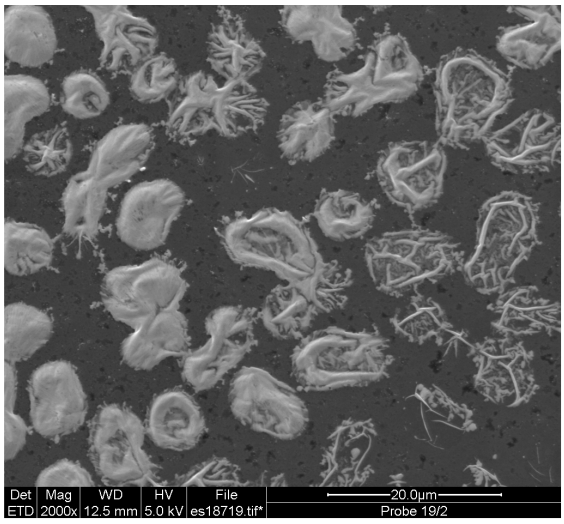

b.) SE image of morphology 10

Figure 6.39: SE (secondary electron) images of sample K19/2 after thermal annealing process a.) all around b.) morphology6. Composition of all structures

In contrast another detected morphology on sample K19/2, which was noted by morphology 11, and which is displayed in figure 6.40a.), was analyzed by EDX technique investigations. The conclusion of these analysis was made in the following way: Because in zone 2 and 3 the oxide signal is definite smaller than in zone 1, the disrupted hill must lay on a platform and exists of a gold-silicon eutectic mixture. If there exists a chemical connection between gold and silicon was not possible to detect with this investigation form.

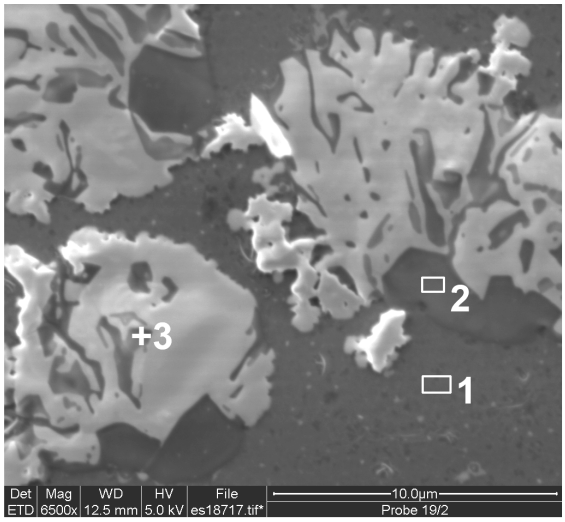

a.) SE image of morphology 11

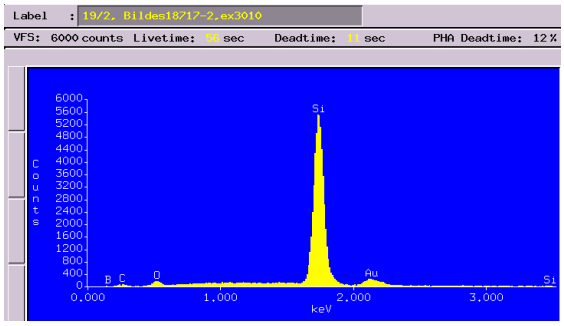

c.) EDX spectrum of zone 2, E=5keV

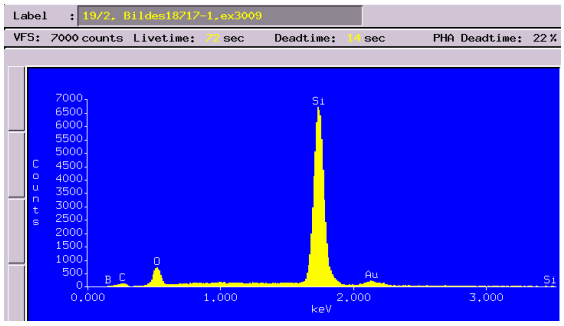

b.) EDX spectrum of zone 1, E=5keV

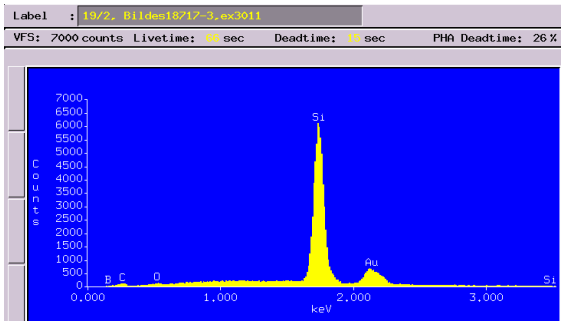

d.) EDX spectrum of zone 3, E=5keV

Figure 6.40: sample K19/2 after thermal annealing process **a.)** morphology 7 and **b.) - d.)** the corresponding EDX spectrums measured at in a.) assigned places

6.4. discussion

At first it should be noted that the macroscopic changing morphology process was detected at many different gold samples. On the other hand in-situ X-ray diffraction measurement was only investigated at one gold sample.
At second because of the significant conclusions in connection with the pyramidical morphology after thermal annealing process with 500℃ and higher temperature, there should be investigated TEM (transmission electron microscopy) measurements of this morphology proving if there exist a chemical connection between gold, silicon, and oxide.
If any chemical alloys will be detected by TEM (transmission electron microscopy) the reciprocal space of these materials should be studied by a special Psi map with X-ray diffraction technique analyzing the crystallite orientation and size. At this point it should be noted that all measured Psi maps of this diploma thesis were made with a psi step wide of five degree. So it is probably possible that some small peaks of this unknown material were not measured. And therefore no alloy with gold, silicon, or oxide could be identified with the three unidentified X-ray diffraction peaks.

VII. conclusion

All temperature induced structure changes of small (<170nm) gold layers, which were evaporated on a thermal oxidized silicon substrate, are concluded in this chapter.

- Texture development of the 2D gold powder:
  - As prepared a strong {111} and small {511} texture were detected
  - The {111} texture got stronger with increasing thermal annealing temperature
  - The {511} texture got smaller with increasing thermal annealing temperature
  - After thermal annealing process with special temperature further more textures were detected:
    - After 700℃ : a small {220} texture
    - After 900℃ : a strong {200} texture
- After thermal annealing with 450℃ and higher thermal annealing temperature following facts were observed:
  - Macroscopic changing by gold layer cracking
  - In [11-1] direction a nearly linear with temperature crystallite increasing process was calculated by Scherrer equation
  - The micro strain in [111] direction increase nearly linearly with temperature until 500℃ and decrease nearly linearly with higher temperature until a smaller unit than as prepared
  - The crystallite alignment increase nearly linearly with higher thermal annealing temperature
  - Gold hill highness profile was measured with AFM (atomic force microscopy) up to 300nm after thermal annealing with 500℃
  - different morphologies
  - a pyramidical morphology laying deeper than the SiO_2-layer of the substrate
  - the pyramidical morphology are in connection with three unidentified X-ray diffraction peaks
  - the three unidentified X-ray diffraction peaks cannot be assigned to any gold or silicon alloy
  - the pyramidical morphology was identified as the origin of the macroscopic changing process
  - on hills above the SiO_2-layer silicon was detected with EDX (energy dispersive X-ray spectroscopy) investigation
- Thermal expansion coefficient of gold were calculated with $\alpha=15{,}6\times10^{-6}\ C^{-1}$
- Crystallite size do not increase linearly in [111] direction.
  - After thermal annealing with 500℃ the crystallite size growth is considerably stronger than before.
  - After 700℃ and higher thermal annealing temperature the crystallite size growth remained static
  - The crystallite size increase from circa 19nm to 30nm (calculated with Scherrer equation and Williamson Hall plot)

Bibliography

[1] Straumanis – “Neubestimmung der Gitterparameter, Dichten und Thermischen Ausdehnungskoeffizienten von Silber und Gold” – Monatshefte für Chemie 102,1377-1386 (1971)

[2] Markus Koini – “In-situ measurement of recrystallisation process in NI – Superalloys” – Diploma Thesis 2006

[3] Armin Moser – “Crystal Structure Determination from Two-Dimesional powders” – Diplomarbeit 2008

[4] Thomas Haber – “Stuctural order in epitaxially grown” – diploma thesis 2004

[5] Prof. Klaus Schäfer, Dr. Claudia Synowietz – “Taschenbuch für Chemiker und Physiker“ – Band 3 – SpringerVerlag 1970

[6] Ingo Salzmann – “-ray diffraction studies in combination with crystallographic simulations” – Diploma thesis 2003

[7] Mario Birkholz – “Thin film analysis by x-ray scattering” – WILEY VCH2006

[8] A.J.C. Wilson and E. Prince – “International Tables for Crystallography”, Volume C 1999

[9] Oliver Werzer – “Structure and Morphology of Thiophene Based Polymers and Pentacene for Organic Electronics: an X-ray Based Study” – Doctoral Thesis 2007

[10] Kathleen Lonsdale – “International tables for X-ray crystallography, Vol.3”

[11] Roland Resel – “Modern x-ray diffraction” – script 2008

[12] R.P.Elliott and F.A.Shunk – “The Au-Si(Gold-Silicon) System”,Bulletin of Alloy Phase Diagrams Vol2 No3 1981

[13] R.W.Cheary - “X-ray diffraction line broadening from thermally deposited gold films” – J.Appl. Cryst. 33, 1271-1283

[14] J.I.Langford, A.J.C. Wilson – “Scherrer after sixty Years: A survey and some new results in the determination of crystallite size” – J.Appl. Cryst. (1978) 11,102-113

[15] Thomas Ederth, “Tempate stripped gold surfaces with 0.4nm rms roughness suitable for force measurements: Application to Casimir force in the 20-100 nm range” – Phys. Rev. A, Vol. 62, 2000

[16] Ingo Salzmann and Roland Resel – “STEREOPOLE: software for the analysis of X-ray diffraction pole figures with IDL”, Journal of Appl. Cryst. (2004),37, 1029-1033

[17] Couderc, J.J.;Garigue, G.;Lafourcade, L.;Nguyen, Q.T – “Eine Versuchsanordnung und Beispiele zur kontinuierlichen Strukturanalyse mit Roentgenstahlen”, Zeitschrift fuer Metallkunde (1959) 50, 708-716”,

[18] Dutta, B.N.;Dayal, B. – “Lattice constants and thermal expansion of gold up to 878 C by X-ray method”, Physica Status Solidi (1963) 3, 473-477

[19] Robert F. Adamsky and Robert E. LeBlanc – “Nucleation and initial growth of single-crystal-films”, J. Vac. Sci. Technol. Volume 2, Issue 2, pp. 79-83 (March 1965)

[20] A.Gibaud and S. Hazra – “X-ray reflectivity and diffuse scattering”, Current science, VOL. 78, NO. 12, 25 JUNE 2000

[21] Thomas Haber, Martin Oehzelt, Roland Resel – “X-ray diffraction”, script Graz University of Technology, Oct. 8, 2007

[22] Birgit Jahn and Matthias Baumann – “Röntgenreflektivitätsmessungen“, script Graz university of technology, Dec. 2, 2006

[23] M.J. Rost, D.A. Quist and J.W.M. Frenken – “Grains, growth, and grooving”, Phys. Rev. Let., VOL.91,026101 (2003)
[24] T.F. Young, J.F. Chang, and H.Y. Ueng – “Study of annealing effects of Au thin films on Si”, Thin Solid Films 322 (1998) 319-322
[25] R.P.Anantatmula, A.A.Johnson, S.P.Gupta, and R.J.Horylev – “The gold-silicon phase diagram”, J. Electronic. Mat., VOL.4, No.3, 1975
[26] C.J.Madams, D.V.Morgan, and M.J.Howes – “Migration of gold atoms through thin silicon oxide films”, J. Appl. Ph., VOL45, No.11, Nov 1974
[27] Liwei Lin, Yu-Ting CHENG, and Khalil Najafi – “Formation of Gold Eutectic bond using localized heating method”, Jpn. J. Appl. Phys. Vol.37 (1998) pp. L1412 –l1414
[28] J.L.Plaza, S.Jacke, Y.Chen, and R.E.Palmer – “nnealing effects on the microstructure of sputtered gold layers on oxidized silicon investigated by scanning electron microscopy and scanning probe microscopy”, Philosophical Magazine, 2003, Vol.83, No.9, 1137-1142
[29] G.K.Williamson and W.H.Hall – “X-ray Line broading from filed aluminium and wolfram”, Acta Metallurgica, Vol.1, Jan. 1953
[30] J W C de Vries, “Resistivity of thin Au films as a function of grain diameter and temperature”, J. Phys. F: Met. Phys. 17 (1987), 1945 – 1952
[31] Kjeld Pedersen and Per Morgen – “Room-temperature deposition and growth of Au on clean and oxygen passivated Si(111) surfaces investigated by optical second-harmonic generation”, J.Phys.: Condens. Matter) (1997), 9497-9506
[32] G.A.Andersen, J.L.Bestel, A.A.Johnson, and B.Post – “Eutectic Decomposition in the gold-silicon system”, Mater. Sci. Eng., 7(1971) 83-90
[33] Feng Huang, Ph. D. “X-ray Reflectivity Studies of Thin Film”, Internal Report of Center of materials (university of Alabama, June 2005)
[34] S.Weber, J. Appl. Crystallogr. 29, 306 (1996)
[35] Thomas Haber, martin Oehzelt, Roland Resel – “X-ray diffraction”, script Graz University of Technology (institute of solid physics), 2007
[36] David R. Lide, “Handbook of chemistry and physics”, 76th-edition 1995-19996
[37] P.Pölt, “Präsentation - ESEM”, presentation 2008

Appendix

appendix 1- written Matlab 7-program codex

The function **“convert”** is converting the ASCI generated measurement data from Phillips goniometer to an useable Matlab matrix. So the measured data can be used and plotted by Matlab7.

```
function convert(st)

if nargin < 1
   clc;
   disp(' ');
   disp('Syntax: convert([filename])');
   disp(' ');
   disp('Input Extensions: ');
   disp('=======================================================');
   disp('RWA ... Polefigure from TEX');
   disp('COA ... Pol-Correction from TEX');
   disp('SCA ... Scanfile from TEX');
   disp('DAT ... Scanfile from SIEMENS (INF-File must be attached)');
   disp(' ');
   disp('Data will be stored in [filename].LST')
   disp('Experimental configuration will be stored in [filename.INF]');
end

inp=sprintf('%s',st(length(st)-2:length(st)));
st=sprintf('%s',st(1:length(st)-4));

if nargin == 1
   str=sprintf('%s.%s',st,inp);
   fid=fopen(str,'r');
   if fid == -1
      disp('File not found...');
      return
   end

   % *** RWA/COA Conversion ***

   if (inp == 'RWA') | (inp == 'rwa') | (inp == 'COA') | (inp == 'coa')

      item='TwoTheta,';
      abb=0;
      while abb == 0
         x=fscanf(fid,'%s',1);
         if sum(x) == sum(item)
            abb=1;
         end
      end
      ttheta=fscanf(fid,'%f',1);
      fscanf(fid,'%s',4);
      psistart=fscanf(fid,'%f',1);
      fscanf(fid,'%s',1);
      psiend=fscanf(fid,'%f',1);
      fscanf(fid,'%s',1);
```

```
      psistep=fscanf(fid,'%f',1);
      fscanf(fid,'%s',1);
      phistart=fscanf(fid,'%f',1);
      fscanf(fid,'%s',1);
      phiend=fscanf(fid,'%f',1);
      fscanf(fid,'%s',1);
      phistep=fscanf(fid,'%f',1);
      fscanf(fid,'%s',1);
      timestep=fscanf(fid,'%f',1);
      fscanf(fid,'%s',2);
      n=fscanf(fid,'%d',1);
      fscanf(fid,'%s',1);

      for k=1:n
         I(k)=fscanf(fid,'%d',1);
         p=fscanf(fid,'%s',1);
         if (sum(char(p)+0) ~= 44)
            fseek(fid,-length(p)-1,0);
         end
      end
      fclose(fid);

      str=sprintf('%s.LST',st);
      fid=fopen(str,'w');

      k=1;
      for psi=psistart:psistep:psiend
         for phi=phistart:phistep:(phiend-phistep)
            fprintf(fid,'%7.3f   %7.3f   %6d\n',psi,phi,I(k));
            k=k+1;
         end
      end
      fclose(fid);

      str=sprintf('%s.INF',st);
      fid=fopen(str,'w');
      if (inp == 'RWA') | (inp == 'rwa')
         fprintf(fid,'Polfigure:
%s.RWA\n=====================================\n',st);
      end
      if (inp == 'COA')| (inp == 'coa')
         fprintf(fid,'Pol-Correction:
%s.COA\n=====================================\n',st);
      end
      fprintf(fid,'2Theta: %f\n',ttheta);
      fprintf(fid,'PSI(Start,Step,End): %7.3f  %7.3f
%7.3f\n',psistart,psistep,psiend);
      fprintf(fid,'PHI(Start,Step,End): %7.3f  %7.3f
%7.3f\n',phistart,phistep,phiend);
      fprintf(fid,'Time/Step: %f\n',timestep);
      fprintf(fid,'Datapoints: %d\n',n);
      fclose(fid);

   end

   % *** SCA Conversion ***
   if (inp == 'SCA') | (inp == 'sca')

      item='FirstAngle,';
      abb=0;
      while abb == 0
         x=fscanf(fid,'%s',1);
         if sum(x) == sum(item)
```

```
            abb=1;
         end
      end

      start=fscanf(fid,'%f',1);
      fscanf(fid,'%s',2);
      range=fscanf(fid,'%f',1);
      fscanf(fid,'%s',2);
      step=fscanf(fid,'%f',1);
      fscanf(fid,'%s',1);
      timestep=fscanf(fid,'%f',1);
      fscanf(fid,'%s',2);
      n=fscanf(fid,'%d',1);
      fscanf(fid,'%s',1);



      for k=1:n
         I(k)=fscanf(fid,'%f',1);
         p=fscanf(fid,'%s',1);
         if (sum(char(p)+0) ~= 44)
            fseek(fid,-length(p)-1,0);
         end
      end
      fclose(fid);

      str=sprintf('%s.LST',st);
      fid=fopen(str,'w');

      winkel=start;
      for k=1:n
         fprintf(fid,'%7.3f   %7.3f\n',winkel,I(k));
         winkel=winkel+step;
      end
      fclose(fid);

      str=sprintf('%s.INF',st);
      fid=fopen(str,'w');
      fprintf(fid,'Scanfile:
%s.SCA\n=====================================\n',st);
      fprintf(fid,'Angle(Start,Step,End): %7.3f  %7.3f
%7.3f\n',start,step,start+range);
      fprintf(fid,'Time/Step: %f\n',timestep);
      fprintf(fid,'Datapoints: %d\n',n);
      fclose(fid);
   end


   % *** DAT Conversation ***

   if (inp == 'DAT') | (inp == 'dat')

      str=sprintf('%s.DAT',st);
      fid=fopen(str,'r');
      I=fscanf(fid,'%f %f',[2,inf]);
      fclose(fid);

      str=sprintf('%s.LST',st);
      fid=fopen(str,'w');
      fprintf(fid,'%7.3f   %6d\n',I);
      fclose(fid);

      str=sprintf('%s.INF',st);
```

```
      fid=fopen(str,'r');
      head=fscanf(fid,'%c',inf);
      fclose(fid);
      fid=fopen(str,'w');
      fprintf(fid,'%c',head);
      fclose(fid);
   end

end
```

The Matlab7 script **Image_9** generates measured Psi map data matrices by using the function convert, plot them, and save the plots as well as the generated matrices automatically with a filename, which includes measurement date, sample name, and the annealing temperature of the sample. The generated measurement data matrices are generated in a way that they can be opened and used by Origin7 easier.

```
%Konvertierung und Darstellung von mehreren  Theta/2Theta-Messungen in
Psi_Maps
%Es werden für jede Messung eigene Ordner erstellt
%Die Werte werden geladen und als Matrix im Ordner DAT abgespeichert
%linear,logarithmisch, und squareroot dargestellt
%Von allen Werten gibt es eine Darstellung im realen Winkelraum und im
reziproken
%Raum

%Karolf 26.02.2010;
clear all;
close all;
%-------------------------Messdaten-----------------------------------%
%       Datum   Probe  TH   ht T_m   Phi      Psi     2Theta  s/step
 H={01 '080125' 'K16' 0024 000 0024 000.0 -10 5.0 90 40 0.10 110 2.10;
    02 '080125' 'K15' 0024 000 0024 000.0 -10 5.0 90 40 0.10 110 2.10;
    03 '080127' 'K11' 0024 000 0024 000.0 -10 5.0 90 40 0.10 110 2.10;
    04 '080129' 'K12' 0024 000 0024 000.0 -10 5.0 90 40 0.10 110 2.10;
    05 '080219' 'K13' 0024 000 0024 000.0 -10 5.0 90 40 0.10 110 2.10;
    06 '080221' 'K14' 0024 000 0024 000.0 -10 5.0 90 40 0.10 110 2.10;
    07 '080222' 'K15' 0024 000 0024 000.0 -10 5.0 90 40 0.20 110 2.45;
    08 '080225' 'K15' 0100 012 0024 000.0 -10 5.0 90 40 0.20 110 2.45;
    09 '080227' 'K15' 0200 012 0024 000.0 -10 5.0 90 40 0.20 110 2.45;
    10 '080228' 'K15' 0300 012 0024 000.0 -10 5.0 90 40 0.20 110 2.45;
    11 '080229' 'K15' 0400 012 0024 000.0 -10 5.0 90 40 0.20 110 2.45;
    12 '080303' 'K15' 0500 012 0024 000.0 -10 5.0 90 40 0.20 110 2.45;
    13 '080304' 'K15' 0600 012 0024 000.0 -10 5.0 90 40 0.20 110 2.45;
    14 '080305' 'K15' 0700 012 0024 000.0 -10 5.0 90 40 0.20 110 2.45;
    15 '080306' 'K15' 0800 012 0024 000.0 -10 5.0 90 40 0.20 110 2.45;
    16 '080307' 'K15' 0900 012 0024 000.0 -10 5.0 90 40 0.20 110 2.45;
    17 '080308' 'K15' 0900 012 0024 000.0 -10 5.0 90 40 0.10 110 2.10;
    18 '080429' 'K12' 0024 000 0024 000.0 -10 2.5 90 40 0.05 110 5.15;
    19 '080507' 'K12' 0400 012 0024 000.0 -10 5.0 90 40 0.20 110 2.45;
    20 '080508' 'K12' 0500 012 0024 000.0 -10 5.0 90 40 0.20 110 2.45;
    21 '080509' 'K12' 0500 012 0024 000.0 -10 5.0 90 40 0.05 110 2.45;
    22 '080512' 'K12' 0500 079 0024 000.0 -10 2.5 90 40 0.10 110 2.45;
    23 '080515' 'K18' 0024 000 0024 000.0 -10 5.0 90 40 0.10 110 2.45;
    24 '080516' 'K20' 0024 000 0024 000.0 -10 2.5 90 40 0.05 110 2.45;
    25 '080519' 'K21' 0024 000 0024 000.0 -10 5.0 90 40 0.10 110 2.45;
    26 '080521' 'K19' 0024 000 0024 356.0 -10 5.0 90 40 0.10 110 2.45;
    27 '080522' 'K22' 0024 000 0024 358.6 -10 5.0 90 40 0.10 110 2.45;
```

```
    28 '080523' 'K24' 0024 000 0024 354.9 -10 5.0 90 40 0.10 110 2.45;
    29 '080526' 'K20' 0500 000 0024 357.6 -10 5.0 90 40 0.10 110 2.45;
    30 '080528' 'K27' 0024 000 0024   6.8 -10 5.0 90 40 0.20 110 2.45;
    31 '080602' 'K23' 0024 000 0024 351.8 -10 5.0 90 40 0.20 110 2.45;
    32 '080605' 'K26' 0024 000 0024 359.3 -10 5.0 90 40 0.20 110 2.45;
    33 '080606' 'K23' 0024 000 0024   2.4 -10 5.0 90 40 0.20 110 2.45;
    34 '080609' 'K28' 0024 000 0024   7.8 -10 5.0 90 40 0.10 110 2.45;
    35 '080610' 'K20' 0500 000 0024   6.2   0   0  0 40 0.01 110 2.45;
    36 '080610' 'K29' 0024 000 0024   5.5 -10 5.0 90 40 0.20 110 2.45;
    37 '081021' 'K18' 0500 060 0024   0   -10 5.0 90 40 0.10 110 2.45;
    38 '081022' 'K11' 0500 060 0024   0   -10 5.0 90 40 0.10 110 2.45;};
%-------------------------Messbedingungen einlesen--------------------%
messung=35;
name=cell2mat(H(messung,3));
temperature=cell2mat(H(messung,4));
date=cell2mat(H(messung,2));
lambda=2.28975;% wellenlänge von Cr
tempstring = sprintf('%04d',temperature);
strh=[name  tempstring date];            %Dateiname
strh1=[name date];

lambda=2.28975;% wellenlänge von Cr
h=cell2mat(H(messung,11:13));
TwoTheta=(h(1):h(2):h(3));t=length(TwoTheta);
h=cell2mat(H(messung,8:10));
Psi=(h(1):h(2):h(3));p=length(Psi);
K=ones(t,p);
format long g;
%-----------------------Ordner für die messung erstellen----------------%
str=['E:\DiplomKarolf\Philips\' name '\MAP'];
str1=[strh 'MAP'];
mkdir(str,str1);

str=['E:\DiplomKarolf\Philips\' name '\Original'];
str1=[strh 'ORG'];
mkdir(str,str1);
    str1=['G:\Philips\' name '\' name date '\*'];
    str2=['E:\DiplomKarolf\Philips\' name '\Original\' strh 'ORG\'];
    copyfile(str1,str2);

str=['E:\DiplomKarolf\Philips\' name '\DAT'];
str1=[strh 'DAT'];
mkdir(str,str1);

str=['E:\DiplomKarolf\Philips\' name '\FIG'];
str1=[strh 'FIG'];
mkdir(str,str1);

%-------------Daten einlesen und Konvertieren-------------------------%
%h1=Psi.*10;
%h1=Psi;
for i=1:p
    %str1=['G:\Philips\' name '\' name date '\K0' num2str(i) 'V.SCA'];
    %str1=['G:\Philips\' name '\' name date '\K16_P' num2str(i) '.SCA']
    h1=Psi(i);
    str1=['G:\Philips\' name '\' name date '\K0' num2str(h1) 'V.SCA'];
    str2=['E:\DiplomKarolf\Philips\' name '\MAP\' strh 'MAP\TwoTheta_'...
    strh '_(' num2str(h1) ').SCA'];
    copyfile(str1,str2);
    convert(str2);
    str3=['E:\DiplomKarolf\Philips\' name '\MAP\' strh 'MAP\TwoTheta_'...
        strh '_(' num2str(h1) ').LST'];
    H=load(str3);
```

```
    %h=(i+125)/25;
    %h=(i+15)/5;
    K(:,i)=H(:,2);
end

%---------------------Daten umwandeln---------------------------------%
KL=max(0,log10(K));
KR=sqrt(K);
KS=K';
KLS=KL';
KRS=KR';
SPSI=Psi';
STwoTheta=TwoTheta';

%---------------------------Matrizen speichern----------------------%
str=['E:\DiplomKarolf\Philips\' name '\DAT\' strh 'DAT\' strh '_linear.dat'
];
save(str,'K','-ASCII');
str=['E:\DiplomKarolf\Philips\' name '\DAT\' strh 'DAT\' strh
'_logarithmic.dat' ];
save(str,'KL','-ASCII');
str=['E:\DiplomKarolf\Philips\' name '\DAT\' strh 'DAT\' strh
'_sqareroot.dat' ];
save(str,'KR','-ASCII');
str=['E:\DiplomKarolf\Philips\' name '\DAT\' strh 'DAT\' strh '_SPsi.dat'
];
save(str,'SPSI','-ASCII');
str=['E:\DiplomKarolf\Philips\' name '\DAT\' strh 'DAT\' strh '_Psi.dat' ];
save(str,'Psi','-ASCII');
str=['E:\DiplomKarolf\Philips\' name '\DAT\' strh 'DAT\' strh
'_STwoTheta.dat' ];
save(str,'STwoTheta','-ASCII');
str=['E:\DiplomKarolf\Philips\' name '\DAT\' strh 'DAT\' strh
'_TwoTheta.dat' ];
save(str,'TwoTheta','-ASCII');
str=['E:\DiplomKarolf\Philips\' name '\DAT\' strh 'DAT\S' strh
'_linear.dat' ];
save(str,'KS','-ASCII');
str=['E:\DiplomKarolf\Philips\' name '\DAT\' strh 'DAT\S' strh
'_logarithmic.dat' ];
save(str,'KLS','-ASCII');
str=['E:\DiplomKarolf\Philips\' name '\DAT\' strh 'DAT\S' strh
'_sqareroot.dat' ];
save(str,'KRS','-ASCII');
%----------------------Daten im Realraum darstellen-------------------%
figure;
axes('Fontsize',20)
pcolor(Psi,TwoTheta,K);
xlabel('\Psi [°]','Fontsize',20); ylabel('2\theta [°]','Fontsize',20);
str=[name ' (Linear) im Realraum bei T=' tempstring '°C'];
title(str);
shading flat;
shading interp;
axis equal;axis tight;
colorbar('Fontsize',20);
str=['E:\DiplomKarolf\Philips\' name '\JPG\LinReal_' strh '.jpeg'];
print('-djpeg',str);
str=['E:\DiplomKarolf\Philips\' name '\FIG\LinReal_' strh '.fig'];
saveas(gcf,str);
%str=['G:\Philips\' name '\JPG\LinReal_' strh '.jpeg'];
%print('-djpeg',str);
```

```
figure;
axes('Fontsize',20)
pcolor(Psi,TwoTheta,KL);
xlabel('\psi [°]','Fontsize',20); ylabel('2\theta [°]','Fontsize',20);
str=[name ' (LOG10) im Realraum bei T=' tempstring '°C'];
title(str);
shading flat;
shading interp;
axis equal;axis tight;
colorbar('Fontsize',20);
str=['E:\DiplomKarolf\Philips\' name '\JPG\LogReal_' strh '.jpeg'];
print('-djpeg',str);
str=['E:\DiplomKarolf\Philips\' name '\FIG\LogReal_' strh '.fig'];
saveas(gcf,str);
%str=['G:\Philips\' name '\JPG\LogReal_' strh '.jpeg'];
%print('-djpeg',str);

figure;
axes('Fontsize',20)
pcolor(Psi,TwoTheta,KR);
xlabel('\Psi [°]','Fontsize',20); ylabel('2\theta [°]','Fontsize',20);
str=[name ' (SQRT) im Realraum bei T=' tempstring '°C'];
title(str);
shading flat;
shading interp;
axis equal;axis tight;
colorbar('Fontsize',20);
str=['E:\DiplomKarolf\Philips\' name '\JPG\SqrtReal_' strh '.jpeg'];
print('-djpeg',str);
str=['E:\DiplomKarolf\Philips\' name '\FIG\SqrtReal_' strh '.fig'];
saveas(gcf,str);
%str=['G:\Philips\' name '\JPG\SqrtReal_' strh '.jpeg'];
%print('-djpeg',str);

%-----------Koordinaten in den Reziproken Raum transformieren----------%
two_theta=TwoTheta;
q=4*pi*sin(two_theta*pi/360)/lambda;
psi=Psi*pi/180;


b=length(q);
a=length(psi);

l=1;
for n=1:b
  for m=1:a;
    qz(n,m)=cos(psi(m))*q(n);
    if psi(m) < 0
    qx(n,m)=-sqrt(q(n).^2-qz(n,m).^2);

    else
    qx(n,m)=sqrt(q(n).^2-qz(n,m).^2);
    end
  end
end

%---------------------Daten im Reziproken Raum darstellen----------------%
figure;
axes('Fontsize',20)
pcolor(qx,qz,(K));
view(0,90);
xlabel('q_{parallel} [Å^{-1}]','Fontsize',20);
ylabel('q_{z} [Å^{-1}]','Fontsize',20);
```

```
shading flat; shading interp;  axis equal;axis tight;
str=[name ' (Linear) im Rez. Raum bei T=' tempstring '°C'];
title(str);
colorbar('Fontsize',20);
str=['E:\DiplomKarolf\Philips\' name '\JPG\LinRez_' strh '.jpeg'];
print('-djpeg',str);
str=['E:\DiplomKarolf\Philips\' name '\FIG\LinRez_' strh '.fig'];
saveas(gcf,str);
%str=['G:\Philips\' name '\JPG\LinRez_' strh '.jpeg'];
%print('-djpeg',str);

figure;
axes('Fontsize',20)
pcolor(qx,qz,(KR));
view(0,90);
xlabel('q_{parallel} [Å^{-1}]','Fontsize',20);
ylabel('q_{z} [Å^{-1}]','Fontsize',20);
shading flat; shading interp;
axis equal;axis tight;
str=[name ' (SQRT) im Rez. Raum bei T=' tempstring '°C'];
title(str);
colorbar('Fontsize',20);
str=['E:\DiplomKarolf\Philips\' name '\JPG\SqrtRez_' strh '.jpeg'];
print('-djpeg',str);
str=['E:\DiplomKarolf\Philips\' name '\FIG\SqrtRez_' strh '.fig'];
saveas(gcf,str);
%str=['G:\Philips\' name '\JPG\SqrtRez_' strh '.jpeg'];
%print('-djpeg',str);

figure;
axes('Fontsize',20)
pcolor(qx,qz,(KL));
view(0,90);
xlabel('q_{parallel} [Å^{-1}]','Fontsize',20);
ylabel('q_{z} [Å^{-1}]','Fontsize',20);
shading flat; shading interp;  axis equal;axis tight;
str=[name ' (LOG10) im Rez. Raum bei T=' tempstring '°C'];
title(str);
colorbar('Fontsize',20);
str=['E:\DiplomKarolf\Philips\' name '\JPG\LogRez_' strh '.jpeg'];
print('-djpeg',str);
str=['E:\DiplomKarolf\Philips\' name '\FIG\LogRez_' strh '.fig'];
saveas(gcf,str);
%str=['G:\Philips\' name '\JPG\LogRez_' strh '.jpeg'];
%print('-djpeg',str);
```

The matlab7 script **“vergleich_relativ2”**

```
%-Darstellung von mehreren  Theta/2Theta-Messungen in Maps
% linear,logarithmisch, und squareroot dargestellt
% mit Hilfe der generierten DAT-Matrizen von den jeweiligen Messungen
%-Von allen Werten gibt es eine Darstellung im Realraum und im reziproken
% Raum

%Karolf 17.02.2010;
clear all;
%---------------------------Messbedingungen---------------------------%
%       Datum   Probe  TH   tH T_m   Phi      Psi     2Theta  s/step
 H={01 '080125' 'K16' 0024 000 0024 000.0 -10 5.0 90 40 0.10 110 2.10;
    02 '080125' 'K15' 0024 000 0024 000.0 -10 5.0 90 40 0.10 110 2.10;
    03 '080127' 'K11' 0024 000 0024 000.0 -10 5.0 90 40 0.10 110 2.10;
    04 '080129' 'K12' 0024 000 0024 000.0 -10 5.0 90 40 0.10 110 2.10;
    05 '080219' 'K13' 0024 000 0024 000.0 -10 5.0 90 40 0.10 110 2.10;
    06 '080221' 'K14' 0024 000 0024 000.0 -10 5.0 90 40 0.10 110 2.10;
```

```
    07 '080222' 'K15' 0024 000 0024 000.0 -10 5.0 90 40 0.20 110 2.45;
    08 '080225' 'K15' 0100 000 0024 000.0 -10 5.0 90 40 0.20 110 2.45;
    09 '080227' 'K15' 0200 000 0024 000.0 -10 5.0 90 40 0.20 110 2.45;
    10 '080228' 'K15' 0300 000 0024 000.0 -10 5.0 90 40 0.20 110 2.45;
    11 '080229' 'K15' 0400 000 0024 000.0 -10 5.0 90 40 0.20 110 2.45;
    12 '080303' 'K15' 0500 000 0024 000.0 -10 5.0 90 40 0.20 110 2.45;
    13 '080304' 'K15' 0600 000 0024 000.0 -10 5.0 90 40 0.20 110 2.45;
    14 '080305' 'K15' 0700 000 0024 000.0 -10 5.0 90 40 0.20 110 2.45;
    15 '080306' 'K15' 0800 000 0024 000.0 -10 5.0 90 40 0.20 110 2.45;
    16 '080307' 'K15' 0900 000 0024 000.0 -10 5.0 90 40 0.20 110 2.45;
    17 '080308' 'K15' 0900 000 0024 000.0 -10 5.0 90 40 0.10 110 2.10;
    18 '080429' 'K12' 0024 000 0024 000.0 -10 2.5 90 40 0.05 110 5.15;
    19 '080507' 'K12' 0400 012 0024 000.0 -10 5.0 90 40 0.20 110 2.45;
    20 '080508' 'K12' 0500 012 0024 000.0 -10 5.0 90 40 0.20 110 2.45;
    21 '080509' 'K12' 0500 012 0024 000.0 -10 5.0 90 40 0.05 110 2.45;
    22 '080512' 'K12' 0500 079 0024 000.0 -10 2.5 90 40 0.10 110 2.45;
    23 '080515' 'K18' 0024 000 0024 000.0 -10 5.0 90 40 0.10 110 2.45;
    24 '080516' 'K20' 0024 000 0024 000.0 -10 2.5 90 40 0.05 110 2.45;
    25 '080519' 'K21' 0024 000 0024 000.0 -10 5.0 90 40 0.10 110 2.45;
    26 '080521' 'K19' 0024 000 0024 356.0 -10 5.0 90 40 0.10 110 2.45;
    27 '080522' 'K22' 0024 000 0024 358.6 -10 5.0 90 40 0.10 110 2.45;
    28 '080523' 'K24' 0024 000 0024 354.9 -10 5.0 90 40 0.10 110 2.45;
    29 '080526' 'K20' 0500 000 0024 357.6 -10 5.0 90 40 0.10 110 2.45;
    30 '080528' 'K27' 0024 000 0024   6.8 -10 5.0 90 40 0.20 110 2.45;
    31 '080602' 'K23' 0024 000 0024 351.8 -10 5.0 90 40 0.20 110 2.45;
    32 '080605' 'K26' 0024 000 0024 359.3 -10 5.0 90 40 0.20 110 2.45;
    33 '080606' 'K23' 0024 000 0024   2.4 -10 5.0 90 40 0.20 110 2.45;
    34 '080609' 'K28' 0024 000 0024   7.8 -10 5.0 90 40 0.10 110 2.45;
    35 '080610' 'K20' 0500 000 0024   6.2   0   0  0 40 0.01 110 2.45;
    36 '080610' 'K29' 0024 000 0024   5.5 -10 5.0 90 40 0.20 110 2.45;
    37 '081021' 'K18' 0500 060 0024   0   -10 5.0 90 40 0.10 110 2.45;
    38 '081022' 'K11' 0500 060 0024   0   -10 5.0 90 40 0.10 110 2.45;};

%-------------------------Messbedingungen einlesen-------------------
close all;
messung=14;
name=cell2mat(H(messung,3));
temperature=cell2mat(H(messung,4));
date=cell2mat(H(messung,2));
thetamin=cell2mat(H(messung,11));dtheta=cell2mat(H(messung,12));
thetamax=cell2mat(H(messung,13));
lambda=2.28975;                    % wellenlänge von Cr
tempstring = sprintf('%04d',temperature);
strh=[name  tempstring date];             %Dateiname
strh1=[name date];

%-------------------------- Daten Laden --------------------------------%
str=['E:\DiplomKarolf\Philips\' name '\DAT\'  strh 'DAT\' strh
'_linear.dat' ];
K=load(str);
str=['E:\DiplomKarolf\Philips\' name '\DAT\'  strh 'DAT\' strh
'_logarithmic.dat' ];
KL=load(str);
str=['E:\DiplomKarolf\Philips\' name '\DAT\' strh 'DAT\' strh '_Psi.dat' ];
Psi_h=load(str);            %spalten
dPsi=round(Psi_h(2)-Psi_h(1));
str=['E:\DiplomKarolf\Philips\' name '\DAT\'  strh 'DAT\' strh
'_TwoTheta.dat' ];
TwoTheta_h=load(str);       %Zeilen


%----------------Bestimmte Werte zum Vergleich herausnehmen------------%
```

```
old_psi=length(Psi_h);old_TwoTheta=length(TwoTheta_h);
%neue Psi :    (-10:5:90)    Länge 21
%neue 2Theta : (40:0.2:110)  Länge 351
f_psi=(old_psi-1)/20;f_psi=round(f_psi);
f_TwoTheta=(old_TwoTheta-1)/350;f_TwoTheta=round(f_TwoTheta);
KL=KL(1:f_TwoTheta:old_TwoTheta,1:f_psi:old_psi);

%------------------counts auf Au-Textur normieren-------------------------
%

countmax=zeros(1,3);
nPsi=1-Psi_h(1)/dPsi;     %Index für specular scan

countmax(1)=max(KL(80:100,nPsi)); %Au111
countmax(2)=max(KL(112:155,nPsi)); %Au200
countmax(3)=max(KL(317:340,nPsi)); %Au220
if max(countmax(:))==countmax(1)
    texture=1;
elseif max(countmax(:))==countmax(2)
    texture=2;
else
    texture=3;
end
countmax=max(countmax(:));
KL=KL./countmax;
%-----------Koordinaten in den Reziproken Raum transformieren----------%
two_theta=TwoTheta_h(1:f_TwoTheta:old_TwoTheta);
q=4*pi*sin(two_theta*pi/360)/lambda;
psi=Psi_h(1:f_psi:old_psi)*pi/180;


b=length(q);
a=length(psi);

l=1;
for n=1:b
  for m=1:a;
    qz(n,m)=cos(psi(m))*q(n);
    if psi(m) < 0
    qx(n,m)=-sqrt(q(n).^2-qz(n,m).^2);

    else
    qx(n,m)=sqrt(q(n).^2-qz(n,m).^2);
    end
  end
end

%--------------------Daten im Reziproken Raum darstellen----------------%
%hold on;
figure;
axes('Fontsize',20)
pcolor(qx,qz,(KL));
view(0,90);
xlabel('q_{parallel} [Å^{-1}]','Fontsize',20);
ylabel('q_{z} [Å^{-1}]','Fontsize',20);
shading flat; shading interp;  axis equal;axis tight;
str=[ name ' (LOG10) in Rez. space bei T=' temperature '°C'];
str=[ name ' (LOG10) in Rez. space bei T=' temperature '°C ,measurement '
date];
s1=size(K);s2=size(KL);
str1=['\Psi' ' x 2' '\Theta : Plot ' num2str(s2(2)) ' x ' num2str(s2(1))...
      ',measured points ' num2str(s1(2)) ' x ' num2str(s1(1))];
%str2=['Strahl auf makroskopisch veränderten Bereich gerichtet'];
```

```
%str1=['Messung ' date];
%hold off;
%title({str;str1});
%title({str;str1;str2});
%-------------------------------------------------------------------------
%-------------------------colorbar relativieren-------------------------%
%-------------------------------------------------------------------------
caxis([0 1]);
%Au111-Textur :
h=winkel([1 1 1],[1 1 1]);h=round(h(1)/dPsi);h=nPsi+h;
peak111_111=max(KL(80:100,h));
h=winkel([1 1 1],[2 2 0]);h=round(h(1)/dPsi);h=nPsi+h;
peak220_111=max(KL(315:335,h));
h=winkel([1 1 1],[2 0 0]);h=round(h(1)/dPsi);h=nPsi+h;
peak200_111=max(KL(132:152,h));
%Au 200-Textur
h=winkel([2 0 0],[2 0 0]);h=round(h(1)/dPsi);h=nPsi+h;
peak200_200=max(KL(132:152,h));
h=winkel([2 2 0],[2 0 0]);h=round(h(1)/dPsi);h=nPsi+h;
peak220_200=max(KL(315:335,h));
h=winkel([1 1 1],[2 0 0]);h=round(h(1)/dPsi);h=nPsi+h;
peak111_200=max(KL(80:100,h));
%Au 220-Textur
h=winkel([2 2 0],[2 2 0]);h=round(h(1)/dPsi);h=nPsi+h;
peak220_220=max(KL(315:335,h));
h=winkel([2 2 0],[2 0 0]);h=round(h(1)/dPsi);h=nPsi+h;
peak200_220=max(KL(132:152,h));
h=winkel([2 2 0],[1 1 1]);h=round(h(1)/dPsi);h=nPsi+h;
peak111_220=max(KL(80:100,h));
%Au 511-Textur
peak220_511=max(KL(315:335,h));h=round(h(1)/dPsi);h=nPsi+h;
peak200_511=max(KL(132:152,h));h=round(h(1)/dPsi);h=nPsi+h;
peak111_511=max(KL(80:100,h));h=round(h(1)/dPsi);h=nPsi+h;
%1000 und 50 counts
counts50=log10(50)/countmax;
counts1000=log10(1000)/countmax;

%-------------------------------------------------------------------------
%-----------------colorbar plotten--------------------------------------
%-------------------------------------------------------------------------
%if texture(1)==1
 %   h=2;
 %  if h==1 %111+200 Textur
 %     colorbar('Fontsize',15,'YTick',[peak111_111 peak220_111
peak200_111...
 %       peak200_200 peak220_200 peak111_200],'YTickLabel',{'Au111[111]'...
 %
,'Au220[111]','Au200[111]','Au200[200]','Au220[200]','Au111[200]'});

 %  elseif h==2 %111+511-Textur
 %  colorbar('Fontsize',15,'YTick',[peak111_111 peak220_111 peak200_111...
 %  peak200_511 peak220_511 peak111_511],'YTickLabel',{'Au111[111]'...
 %   ,'Au220[111]','Au200[111]','Au200[511]','Au220[511]','Au111[511]'});

  %  else %111+220 Textur
  %  colorbar('Fontsize',15,'YTick',[peak111_111 peak220_111 peak200_111...
  %  peak200_220 peak220_220 peak111_220],'YTickLabel',{'Au111[111]'...
  %   ,'Au220[111]','Au200[111]','Au200[220]','Au220[220]','Au111[220]'});

  %  end

%elseif texture(1)==2
%colorbar('Fontsize',15,'YTick',[peak111_111 peak220_111 peak200_111...
```

```
 %   peak200_200 peak220_200 peak111_200],'YTickLabel',{'Au111[111]'...
  % ,'Au220[111]','Au200[111]','Au200[200]','Au220[200]','Au111[200]'});

%else
%colorbar('Fontsize',15,'YTick',[peak111_111 peak220_111 peak200_111...
%   peak200_220 peak220_220 peak111_220],'YTickLabel',{'Au111[111]'...
%   ,'Au220[111]','Au200[111]','Au200[220]','Au220[220]','Au111[220]'});
%end

%---------------------------------oder-----------------------------
%colorbar('Fontsize',15,'YTick',[peak111_111
peak200_511],'YTickLabel',{'Au111[111]','Au200[511]'});
%-------------------------------------oder-----------------------------
countmax=10^countmax;countmax=int32(countmax);
countmaxstr=num2str(countmax);countmaxstr=['Au111[111]=' countmaxstr
'counts'];
%countmaxstr1=['Au111[111] =    ';'   = ' countmaxstr ' counts' ];


colorbar('Fontsize',15,'YTick',[counts50 peak111_111 counts1000],...
    'YTickLabel',{'50 counts',countmaxstr(1:11),'1000 counts'});
%Au200[511]
%colorbar('Fontsize',15,'YTick',[peak200_511 counts50 peak220_220
counts1000],...
 %   'YTickLabel',{'','50 counts',countmaxstr(1:11),'1000 counts'});
%Au200[511]
h=length(countmaxstr);
text(4.82 ,4.34,countmaxstr(11:h),'Fontsize',15)
text(4.88,0,'logarithmic scale','Rotation',90,'FontSize',25)
%text(1,2,'Au200[511]','Color','black','FontSize',15);
%-----------------------------------------------------------------
%-------------------------------Speichern-----------------------------
%-----------------------------------------------------------------

%str=['E:\DiplomKarolf\Philips\' name '\JPG\LogRez_' strh '.jpeg'];
%print('-djpeg',str);

%close all;


%-------------------------------------------------------------------------
%------------Mit hellblauer 50 counts Colormap darstellen----------------%
%-------------------------------------------------------------------------
%colormap24;

%----------------------------rote colormap-------------------------
colormap_rot;    %Speichert bestimmte colormap in C und plottet diese

%counts50 Lage auf colormap brechnen
color50=counts50*64;
color50h1=round(color50);
if color50h1<color50+0.5
    color50h2=color50h1+1;
else
    color50h2=color50h1-1;
end
C(color50h1,:)=[1 1 1];
C(color50h2,:)=[1 1 1];
colormap(C);
```

function **“hkl_generation1”**

```
% hkl Indizierung im Reziproken raum in der oberen Halbebene
```

```
% function hkl generation
function [q_p,q_z]=f(a,b,c,alpha,beta,gamma_c,hkl_ref,ho,ko,lo)



global H; global K; global L;
H= hkl_ref(:,1);
K= hkl_ref(:,2);
L= hkl_ref(:,3);


% ************** formulae from thomas haber (tu-graz)
*****************************

s11 = b^2*c^2*sin(alpha)^2;
s22 = a^2*c^2*sin(beta)^2;
s33 = a^2*b^2*sin(gamma_c)^2;
s12 = a*b*c^2*(cos(alpha)*cos(beta) - cos(gamma_c));
s23 = a^2*b*c*(cos(beta)*cos(gamma_c) - cos(alpha));
s13 = a*b^2*c*(cos(gamma_c)*cos(alpha) - cos(beta));
v = a*b*c*sqrt(1 - cos(alpha)^2 - cos(beta)^2 - cos(gamma_c)^2 +
2*cos(alpha)*cos(beta)*cos(gamma_c));
d = sqrt(v^2./(s11*H.^2 + s22*K.^2 + s33*L.^2 + 2*s12*H.*K + 2*s23*K.*L +
2*s13*H.*L));
dor = sqrt(v^2./(s11*ho^2 + s22*ko^2 + s33*lo^2 + 2*s12*ho*ko + 2*s23*ko*lo
+ 2*s13*ho*lo));
psi = acos((sqrt(dor^2)*sqrt(d.^2)./v^2.*(s11*ho*H + s22*ko*K + s33*lo*L +
s23*(ko*L + K*lo) + ...
      s13*(lo*H + L*ho) + s12*(ho*K + H*ko))));
q_abs= 2*pi./d;
q_z=abs(cos(psi).*q_abs);
q_p=abs(sin(psi).*q_abs);
```

Matlab7 script **“indices4“**

```
a=4.0704;b=4.0704;c=4.0704;alpha=90;beta=90;gamma=90;name='{Au}'; %Gold
%a=5.4308;b=5.4308;c=5.4308;alpha=90;beta=90;gamma=90;name='{Si}';
%Silizium
%a=12.827;b=10.52;c=3.838;alpha=90;beta=90;gamma=90;name='{Au2O3}';
%Au2O3
%a=4.923000;b=4.923000;c=5.409000;alpha=90;beta=90;gamma=120;name='{SiO2}';
%SiO2
%a=4.731;b=4.731;c=5.280;alpha=90;beta=90;gamma=120;name='{SiO2}';
%SiO2_Damour

alpha=alpha.*pi/180; %Winkeln in Radiant umwandeln
beta=beta.*pi/180;
gamma=gamma.*pi/180;

hkl_ref=[1 0 1];   %hkl indizes
h=[1 1 1];         %crystal orientation

%----------------Reziproke Koordinaten berechnen--------------------%
[qp,qz]=hkl_generation1(a,b,c,alpha,beta,gamma,hkl_ref,h(1),h(2),h(3));

global H K L
Q=[qp, qz, H, K, L,h, 2*pi./sqrt(qp.^2+qz.^2)];

%---------------------High harmonics und kß berechnen----------------%
lambda_a=2.28975;% wellenlänge von Cr k_Alpha
```

```
lambda_b=2.085128; %Wellenlänge von Cr k_Beta

l=lambda_b/lambda_a;
%Q(1)=Q(1)*l;Q(2)=Q(2)*l;name='{\itSi,k\beta }';   %K-beta von Silizium
%Q(1)=Q(1)*l;Q(2)=Q(2)*l;name='{\itAu,k\beta }';   %K-beta von Gold
berechnen
%Q(1)=Q(1)/2;Q(2)=Q(2)/2;name='{\itSi,\lambda\it/2 }';   %1.high harmonic
%Q(1)=Q(1)/2;Q(2)=Q(2)/3;name='{\itSi,\lambda\it/3 }';   %2.high harmonic
%-------------------------------------------------------------------%
TwoTheta=(40:0.2:110);t=length(TwoTheta); %Zeilen
Psi=(-10:5:90);p=length(Psi);             %Spalren

two_theta=TwoTheta;
q=4*pi*sin(two_theta*pi/360)/lambda_a;
psi=Psi*pi/180;


b=length(q);
a=length(psi);

l=1;
for n=1:b
  for m=1:a;
    qz(n,m)=cos(psi(m))*q(n);
    if psi(m) < 0
    qx(n,m)=-sqrt(q(n).^2-qz(n,m).^2);

    else
    qx(n,m)=sqrt(q(n).^2-qz(n,m).^2);
    end
  end
end
%----
%q=sqrt(qp^2+qz^2);
%psi=acos(qz/q);
%q_high1=
%----------------------------Werte Plotten--------------------------%
%H=repmat(reflex,1,size(HKL,2));
%lo=H==HKL;
%lo=sum(lo,1);
%lo=lo==3;
%q_reflex=q_h(:,lo);

%for j=6:15
figure(2);
hold on;
h1=length(Q(:,1));h2=ones(1,h1);h3=ones(2,h1);

for i=1:h1
    h3(1,i)=plot(Q(:,1),Q(:,2),'o','MarkerEdgeColor','k',...
    'MarkerFaceColor','k','LineWidth',1,'MarkerSize',7);
    a1=num2str(Q(i,3));a2=num2str(Q(i,4));a3=num2str(Q(i,5));
    b1=num2str(h(1)); b2=num2str(h(2)); b3=num2str(h(3));
    str=[' ' a1 a2 a3 '_' name '_[' '_' b1 '_' b2 '_' b3 '_]'];
    h3(2,i)=text(Q(i,1),Q(i,2),str,'Color','black','FontSize',15);
    %h3(2,i)=text(Q(i,1)-0.1,Q(i,2)-
0.16,str,'Color','black','FontSize',15);
    %h3(2,i)=text(Q(i,1)-
0.15,Q(i,2)+0.2,str,'Color','black','FontSize',15);
end;
hold off;
```

appendix 2 - special single morphologies

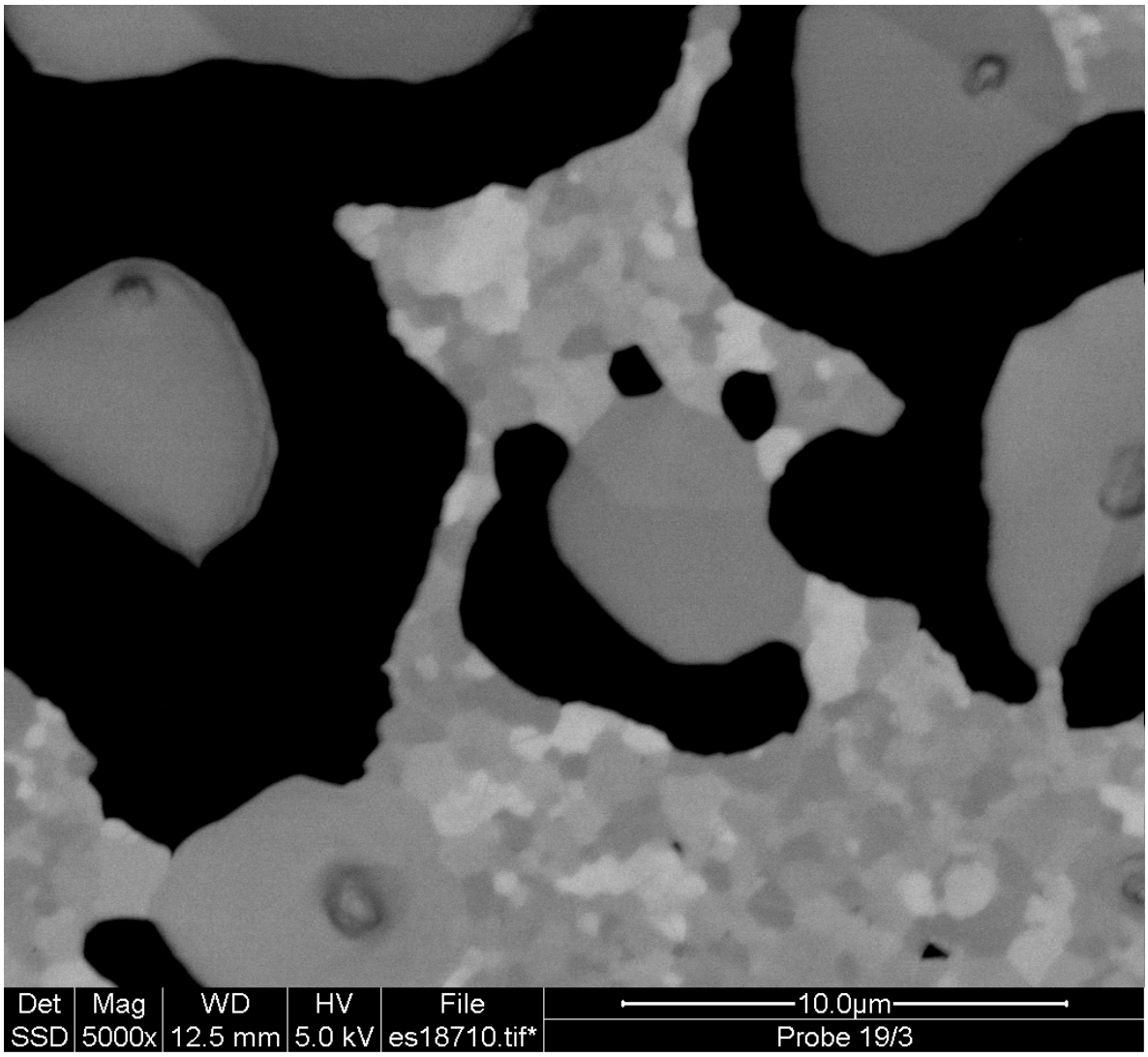

Figure 1.1 : singular morphology after thermal annealing about 500℃

TU Graz
Graz University of Technology
Senat

Deutsche Fassung:
Beschluss der Curricula-Kommission für Bachelor-, Master- und Diplomstudien vom 10.11.2008
Genehmigung des Senates am 1.12.2008

EIDESSTATTLICHE ERKLÄRUNG

Ich erkläre an Eides statt, dass ich die vorliegende Arbeit selbstständig verfasst, andere als die angegebenen Quellen/Hilfsmittel nicht benutzt, und die den benutzten Quellen wörtlich und inhaltlich entnommene Stellen als solche kenntlich gemacht habe.

Graz, am 15.07.2010 ..... (Unterschrift)

Englische Fassung:

STATUTORY DECLARATION

I declare that I have authored this thesis independently, that I have not used other than the declared sources / resources, and that I have explicitly marked all material which has been quoted either literally or by content from the used sources.

15.07.2010
date

..... (signature)